Multi-Spacecraft Solar Surface Stereoscopy: a Method for Direct Estimates of the Wilson Depression from Combined Observations of SO/PHI and SDO/HMI

Von der Fakultät für Elektrotechnik, Informationstechnik, Physik
der Technischen Universität Carolo-Wilhelmina zu Braunschweig

zur Erlangung des Grades einer Doktorin

der Naturwissenschaften (Dr. rer. nat.)

genehmigte Dissertation

von Amanda Romero Avila

aus Mexiko Stadt, Mexiko

eingereicht am: 29.05.2024

Disputation am: 30.08.2024

1. Referent: Prof. Dr. Sami K. Solanki
2. Referent: Prof. Dr. Karl-Heinz Glaßmeier

Druckjahr: 2024

Dissertation an der Technischen Universität Braunschweig,
Fakultät für Elektrotechnik, Informationstechnik, Physik

Abstract

The Wilson depression is the largest height variation in the solar photosphere. Quantifying it is key in the understanding of sunspots. In this work we present a method for a stereoscopic analysis of the height variations in the solar photosphere and to produce the first direct estimates of the Wilson depression. This stereoscopic method allows for the first time to directly compute height variations on the solar surface.

The method presented in this work yields variations in altitude of the solar surface by shifting and correlating two images, mapped along the same epipolar surface profile observed from two different vantage points. This method relies on epipolar geometry and requires a precise camera calibration to resolve the altitude variations of a few hundred kilometers.

The performance and constraints of our method are tested using simulated Stokes-I continuum observations of an MHD simulation of the solar-surface layers. The resulting height estimate is then introduced as an initial height estimate in an optimization algorithm in order to reproduce smaller scale structures. The height estimates from our method reproduce well the overall height variations of the MHD simulation. When applied to test data, our method yields reliable results for a separation of the viewing points between $10°$ and $40°$; and a signal to noise ratio (SNR) of at least 50. We also test the effect that the resolution of the data has on the performance of the method.

We also apply our method to simultaneous continuum intensity observations of a sunspot from Solar Orbiter's Polarimetric and Helioseismic Imager (SO/PHI) and Solar Dynamic Observatory's Helioseismic Magnetic Imager (SDO/HMI) observed on October 29th of 2022. The process of the calibration and rectification of the data as well as the necessary corrections to the data in order to apply the method to the observations are presented.

The results of the stereoscopic analysis of the sunspot, yield a Wilson depression of roughly 800 km. The resolution of the data is the most limiting factor of the performance of the method. A discussion of the method and its limitations, its performance and the obtained results are presented, and possible extensions of the method as well as possible applications of it are discussed.

Zusammenfassung

Die Wilson-Depression ist die größte Höhenvariation auf der Oberfläche Sonne. Ihre Quantifizierung ist von enormer Wichtigkeit für das Verständnis von Sonnenflecken. In dieser Arbeit präsentieren wir eine Methode für eine stereoskopische Bestimmung der Höhenvariationen in der Sonnenphotosphäre und damit einer direkten Messung der Wilson-Depression. Diese stereoskopische Methode ermöglicht zum ersten Mal die direkte Bestimmung von Höhenvariationen auf der Sonnenoberfläche.

Die in dieser Arbeit vorgestellte Methode beruhrt auf einer Korrleation von Intensitätsverteilungen, die von zwei verschiedenen Beobachtungspunkten entlang von epipolaren Oberflächenprofilen auf der Sonne gleichzeitig beobachtet wurden. Die Variation der Oberflächenhöhe kann aus einer kleinen Verschiebung der Intensitätsprofile erschlossen werden, die den besten Korreltionswert ergibt. Die Methode basiert auf einer epipolaren Geometrie und erfordert eine präzise Kamerakalibrierung, um Höhenvariationen von einigen hundert Kilometern aufzulösen.

Die Leistungsfähigkeit unserer Methode wird anhand synthetischer Stokes-I-Kontinuumsbeobachtungen aus MHD-Simulationen einer aktiven Region in der Photosphäre getestet. Das Ergebnis der Korrelationsmethode wird dann als erste Höhenschätzung einem Optimierungsalgorithmus zugeführt, um auch die Höhenschichtung kleinerer Strukturen zu reproduzieren. Bei der Anwendung auf diese Testdaten liefert unsere Methode zuverlässige Ergebnisse für einen Winkelabstand der Beobachtungspunkte zwischen $10°$ and $40°$ und für ein Signal-Rausch-Verhältnis von mindestens 50. Wir untersuchen auch den Effekt, den die räumliche Auflösung der Testdaten auf die Ergebnisse der Methode hat.

Nachdem wir die Leistungsfähigkeit unserer Methode anhand von Simulationen gezeigt haben, wendeten wir sie auch auf gleichzeitige Beobachtungen der Kontinuumsintensitäts eines Sonnenflecks an, die vom Polarimetric and Helioseismic Imager des Solar Orbiters (SO/PHI) und dem Helioseismic Magnetic Imager des Solar Dynamic Observatory (SDO/HMI) am 29. Oktober 2022 aufgenommen wurden. Der Prozess der Kalibrierung und Rektifizierung der Daten sowie die notwendigen Korrekturen der Daten zur Anwendung der Methode auf die Beobachtungen werden präsentiert.

Die Ergebnisse der stereoskopischen Analyse des Sonnenflecks ergeben eine Wilson-Depression von etwa 800 km. Es zeigt sich, dass die Auflösung der Daten der limitierende Faktor für die Leistungsfähigkeit unserer Methode ist. Abschließend werden die erhaltenen Ergebnisse die Einschränkungen sowie mögliche Erweiterungen der Methode und zukunftige Anwendungen der Methode präsentiert.

Contents

1 Introduction **3**

1.1 Sunspots and Wilson Depression 3
1.1.1 Radiative Transfer 3
1.1.2 Granulation 5
1.1.3 Magnetic Flux Tubes 6
1.1.4 Active Regions and the Solar Cycle 7
1.1.5 Sunspots 8
1.1.6 The Wilson Depression 10
1.2 Stereoscopy 15
1.2.1 Camera Model and FITS Parameters 17
1.2.2 Epipolar Geometry 24
1.2.3 Previous Stereoscopic Studies of the Sun 28

2 A Method for Sunspot Stereoscopy **33**

2.1 The Correlation Method 35
2.1.1 Mapping the Surface Grid to an Image 36
2.1.2 Virtual Intensity Profiles 39
2.1.3 The Correlation Coefficient 41
2.1.4 Shift Between the VIPs, Viewing Angles and Surface Normals . . 42
2.1.5 Computing Height Variations From the Optimal Shifts 45
2.2 The Optimization Method 46

3 Application of the Method to Test Data **49**

3.1 Test Data 49
3.2 Practical Reformulations of our Method for the Test Data 51
3.2.1 Correlation Method 52
3.2.2 Optimization Method 53
3.3 Performance on the Method With Test Data 53
3.3.1 Test of the Correlation Method 54
3.3.2 Test of the Optimization Method 58
3.3.3 Test of the Effect of Viewing Angles 60
3.3.4 Analysis of a Second Profile of the Active Region 63
3.3.5 Testing the Effect of Noise in the Reconstructed Height 64
3.3.6 Full 2D Height Maps 67
3.3.7 Estimating a Height Vector for Two Views With Different Resolution 69
3.4 Summary and Discussion 71

4 Application of the Method to Real Data **75**
4.1 Observations From SO/PHI and SDO/HMI: Some Information on the Instruments and Their Images 75
4.1.1 Correction of the WCS Parameters for SO/PHI Data 83
4.2 Results of the Method Applied to Real Data 90
4.2.1 Full 2D Height Map 107
4.3 Summary and Discussion 109

5 Conclusions **113**
5.1 Outlook 114

Bibliography **117**

Aknowledgments **123**

Publications **125**

Curriculum Vitae **127**

Chapter 1

Introduction

The aim of this work is to determine the Wilson depression of sunspots and pores by applying a direct observational method. A stereoscopic method, using combined simultaneous observations from two vantage points was created to estimate 3D photospheric height variations of surface structures.

This introductory chapter gives a brief description of what sunspots and the Wilson depression are, as well as some history on the previous attempts to quantify the latter. An introduction on stereoscopy is also provided. All the basic equations to understand the stereoscopic principles for the analysis performed further down in this work are described as well in this chapter. Finally, a brief overview of previous stereoscopic studies of the Sun is given.

1.1 Sunspots and Wilson Depression

Sunspots are magnetic structures, visible as darker regions on the solar surface. They are characterized by having an umbra, where they appear darkest; and a penumbra, a less darker region surrounding the umbra (see Fig. 1.3). In order to describe and better understand sunspots, a few basic concepts must be introduced. This introduction will give a brief summary of radiative transfer, the solar photosphere and the magnetic structures, the concept of flux tubes and magneto-convection, a simplified model for sunspot formation, and finally a description of sunspots.

1.1.1 Radiative Transfer

Radiative transfer is the process by which energy is transferred by electromagnetic radiation. It is the main mechanism of energy transport in the solar photosphere and above (Murray, 2013). To obtain the basic equations of radiative transfer we first consider a light beam traveling through a small area dA, inside a solid angle $d\omega$, with an inclination of θ with respect to the normal of A over a given time dt. The energy E crossing the area is given by

$$dE = I\ cos\theta\ dA\ dt\ d\nu\ d\omega, \tag{1.1}$$

where I is the specific intensity of the light beam in a particular frequency range $d\nu$.

As light propagates through a medium, it can be affected by processes of emission, absorption or scattering. The intensity I of a beam is increased by emission

processes and decreased by absorption. The emission may be independent of I (spontaneous), or, like the absorption, proportional to I (induced).

Consider a beam with intensity I traveling in the z direction through a medium of thickness dz for a case with simplified geometry, where $\theta = 0°$. This medium might add or subtract energy from the beam by the above mentioned processes. If j_ν is the spontaneous emission coefficient of the medium at frequency ν and κ_ν is the absorption coefficient, the energy added and subtracted to the beam is

$$dE_{added} = j_\nu \, dA \, dt \, d\nu \, dz \tag{1.2}$$

and

$$dE_{substracted} = -\kappa_\nu I \, dA \, dt \, d\nu \, dz, \tag{1.3}$$

respectively. The change in intensity over dz is

$$dI = [j_\nu - \kappa_\nu I]dz \quad \rightarrow \quad \frac{dI}{dz} = -\kappa_\nu I + j_\nu. \tag{1.4}$$

Equation 1.4 is known as the radiative transfer equation (RTE), for which z is the beam's direction of propagation. The ratio between the emission and absorption coefficients is known as the source function $S_\nu \equiv j_\nu/\kappa_\nu$. With this definition, Eq. (1.4) can be written as

$$\frac{dI}{dz} = -\kappa_\nu (I - S_\nu). \tag{1.5}$$

The radiative transfer equation can also be written in terms of optical depth, τ. The optical depth is a measure of the transparency of the medium, and describes the probability of a photon reaching the observer while traveling through it. If $\tau < 1$, the medium is transparent, or optically thin; and for $\tau \geq 1$, the medium is opaque, or optically thick. It is defined as $d\tau_\nu = -\kappa_\nu dz$, which after integration is $\tau = -\int \kappa_\nu dz$. With the former definition Eq. 1.5 can be rewritten as

$$\frac{dI}{d\tau} = I - S_\nu. \tag{1.6}$$

It can be assumed that in the solar photosphere the radiative transfer occurs under local thermodynamic equilibrium (LTE). LTE is a valid assumption when collisions dominate over photonic processes, so that the internal energy distribution within the atoms can be described by a Boltzmann distribution and their ionization equilibrium by Saha-Boltzmann (Stix, 2004). Then the ratio of emission to absorption is a function only of the wavelength and the local temperature.

The photosphere is the Sun's visible surface layer. It is a region from which most of the Sun's visible light at 500 nm is emitted (Priest, 2014b), i.e. where τ varies from $\tau >> 1$ to $\tau << 1$ for visible wavelengths. It is the lower layer of the solar atmosphere, or the directly observable surface of the Sun in visible light. The standard way to define the solar surface is through its radiation.

The photons traveling from the solar core outwards go through a random path, being repeatedly absorbed and re emitted. The distance over which photons can travel before being reabsorbed is called mean free path. The mean free path in the Sun increases with increasing radius as the density and opacity decrease. The radius at which the mean free path is so large that the majority of photons can escape from

the Sun is defined as the solar surface and corresponds to $\tau = 1$. Here τ refers to the optical depth, and its height is dependent on the wavelength. The $\tau = 1$ surface at 500 nm is used as a standard for the solar surface (Priest, 2014a).

The radiation comes from different layers in the solar surface. However, since most of the radiation comes from the $\tau = 1$ layer at 500 nm, this approximation is sufficient to consider this layer as the solar surface for the purposes of this work. Usually, two approaches are used to quantify the contribution of each atmospheric layer to the emitted radiation: the contribution function (CF), which gives the relative contribution of each atmospheric layer to the radiation; and the response function (RF) which measures the response of a given quantity (e.g. temperature, or magnetic field strength), to perturbations in a given atmospheric layer (Magain, 1986).

The contribution function can be obtained by solving the RTE equation. A solution of the RTE equation (Beckers & Milkey, 1975) is

$$I(\tau) = \int_0^\infty S_\nu e^{-\tau} d\tau,$$

and the integrand of the solution is defined as the contribution function:

$$CF \equiv S_\nu e^{-\tau}.$$

The response function (RF) can be defined as the response of the intensity to local changes of a given quantity q at a given optical depth τ or at a given geometrical depth z:

$$RF_q(\tau) = \frac{\partial I}{\partial q(\tau)} \text{ or } RF_q(z) = \frac{\partial I}{\partial q(z)}.$$

These definitions of the response and contribution functions are very simplified and their derivation is not included. Detailed discussions and derivations can be found in e.g., Del Toro Iniesta (2003) and Gray (2021). A very basic assumption throughout this work is that the vertical extent of the response function to, say, temperature with depth z, $R_T(\xi, z)$, at a given position ξ on the solar surface can be replaced by

$$R_T(\xi, z) \to \delta(z - h(\xi)) \int R_T(\xi, z)\, dz, \tag{1.7}$$

i.e., by an effective, height integrated response concentrated at a height $h(\xi)$.

1.1.2 Granulation

The solar surface is covered by granulation. Granules are the manifestation in the photosphere of the turbulent convective motions in the Sun's convective zone and each granule represents the top of a convective cell rising from the solar interior. Granulation is seen in the solar photosphere as a cellular pattern that covers essentially the whole Sun, except where sunspots appear. At any given time there are millions of granules present in the photosphere, which are bright isolated elements that appear on a dark background of multiple connected intergranular lanes (Bray et al., 2009)

Convection is the main energy transport mechanism just below the solar surface. By convection, the different layers of plasma are mixed and the temperature

gradient is reduced. If the vertical temperature gradient ∇T in a fluid is steeper than the adiabatic temperature gradient $\nabla_{ad} T$, then ∇T is said to be super-adiabatic. A super-adiabatic temperature gradient makes the medium unstable for convection. Therefore the condition for convection is $\nabla T > \nabla_{ad} T$.

By convection tiny intense flux tubes are concentrated (see Section 1.1.3) at granulation boundaries (Stix, 2004). A granule in the photosphere is the top of a small convective cell. There are two main cell sizes: granules of the order of ~ 100 to 1000 km in diameter and with a lifetime of ~ 10 minutes, and supergranules with a diameter of $\sim 30,000$ km and lifetimes of 1 to 2 days (Murray, 2013). Granules continuously appear and disappear in a turbulent manner and have irregular shapes. Their centers are bright, consisting of hot rising plasma, while their boundaries are dark, due to the cool falling material (Bray et al., 2009).

1.1.3 Magnetic Flux Tubes

The magnetic field in the photosphere has a wide range of scales and strengths. It can be concentrated forming magnetic flux tubes, regions of space through which strong magnetic field passes (e.g. Parker, 1979; Schüssler et al., 2003; Ryutova et al., 2015). The basic equations to study magnetic fields in an MHD approximation are Gauss's law of magnetism

$$\nabla \cdot \mathbf{B} = 0, \tag{1.8}$$

Ampere's law

$$\nabla \times \mathbf{B} = \mu \mathbf{j}, \tag{1.9}$$

the induction equation

$$\frac{\partial \mathbf{B}}{\partial t} = \nabla \times (\mathbf{u} \times \mathbf{B}) + \eta_D \nabla^2 \mathbf{B}, \tag{1.10}$$

the equation of motion

$$\rho \left(\frac{\partial}{\partial t} + \mathbf{u} \cdot \nabla \right) \mathbf{u} = \mathbf{j} \times \mathbf{B} - \nabla p - \rho \mathbf{g}, \tag{1.11}$$

and the continuity equation

$$\frac{d\rho}{dt} + \rho \nabla \cdot \mathbf{u} = 0, \tag{1.12}$$

where $\mathbf{B}$ is the plasma magnetic field, $\eta_D = 1/\mu_0 \sigma$ is the magnetic diffusivity, σ is the electric conductivity, ρ the plasma density, $\mathbf{u}$ the plasma flow velocity, $\mathbf{j}$ is the electric current density, and $\mathbf{g}$ is the gravity.

If the model consists of a simple magnetic flux tube with cylindrical symmetry, it can be considered as a group of magnetic field lines that are bounded by a closed contour (see Fig. 1.1).

Assuming hydrostatic equilibrium ($\mathbf{u} = 0$), Eq. 1.11 is

$$-\nabla p + \mathbf{j} \times \mathbf{B} - \rho \mathbf{g} = 0. \tag{1.13}$$

With $\mathbf{g}$ acting along the negative z–axis and if the magnetic field depends only on the radial coordinate, such that $\mathbf{B} = B(0, 0, B_z(R))$, Eq. 1.13 can be integrated to

$$p_i(R) + \frac{B_z^2}{2\mu} = p_e + \frac{B_{ze}^2}{2\mu}, \tag{1.14}$$

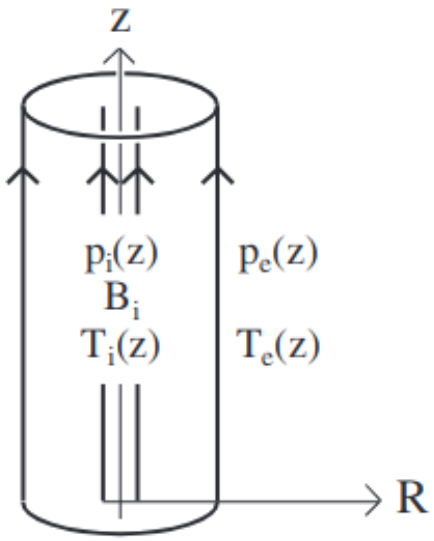

Figure 1.1: A vertical magnetic flux tube embedded in a vertically stratified medium. Taken from Priest (2014b).

where p_i and p_e are the gas pressures inside and outside the flux tube. In the presence of gravity acting along the negative direction of the z-axis, Eq. 1.13 is

$$\frac{dp}{dz} + \rho g(z) = 0. \tag{1.15}$$

The equations above describe the magnetic field and the motion inside vertical magnetic flux tubes, which is the approximation considered in this work to describe sunspots.

Magnetic flux tubes have a typical magnetic field strength of 1 kG in the photosphere, which decreases with height. As a flux tube expands with height, the magnetic field strength ranges from 1500 to 1700 G in the bottom of the photosphere, from 1000 to 1200 G in the middle, and from 200 to 500 G in the top of the photosphere. The plasma beta $\beta = \frac{p}{B^2/2\mu_0}$, which is the ratio of the plasma pressure to the magnetic pressure, is around 0.3 or lower in the flux tubes, meaning that the plasma within is dominated by the magnetic field (Solanki et al., 2006; Priest, 2014a).

1.1.4 Active Regions and the Solar Cycle

Magnetic flux emerges from the photosphere through a wide range of scales. Active regions are large-scale regions of magnetic flux emergence. They appear as regions of enhanced and complex magnetic field around the solar equator. They are formed by concentrations of intense flux tubes. Sunspots and pores can be found within active regions. Active regions are generally restricted to the activity belts on the Sun, usually within a heliographic latitude of $\phi = \mp 30^\circ$ on both solar hemispheres. The latitude on which active regions and sunspots can be seen varies with the solar cycle ; at the beginning of a cycle the sunspots appear in a latitude range of 20° to 30°, which becomes broader as the solar cycle evolves, and the central latitude of the activity belt shifts towards the equator (see Solanki, 2003; Maunder, 1903). Most aspects of the solar activity, including active regions and sunspots are due to the

magnetic field and are a representation of how the solar plasma responds to the underlying magnetic field evolution during a solar cycle (Priest, 2014a).

The solar cycle describes the solar magnetic field on the largest scale, the scale of the field of the Sun as a whole, in which its magnetic activity changes almost periodically every 11 years. The solar magnetic activity is measured in variations in the number of observed sunspots, so that the best indicator of the solar cycle is the sunspot relative number

$$R = k(10g + f_s),$$

where g is the number of sunspot groups, f_s is the total number of spots, and k is a calibration constant. A plot of the sunspot number for the last five solar cycles is displayed in Fig. 1.2. Each solar cycle starts from one minimum and lasts until the next minimum with an average duration of 11 years. On each solar cycle the magnetic polarities of sunspots reverse, and the behavior of the entire solar magnetic field is governed by this reversal (Stix, 2004). At the maximum of the solar cycle, the biggest number of sunspots is observed, and the solar activity is increased, and the opposite happens at solar minimum.

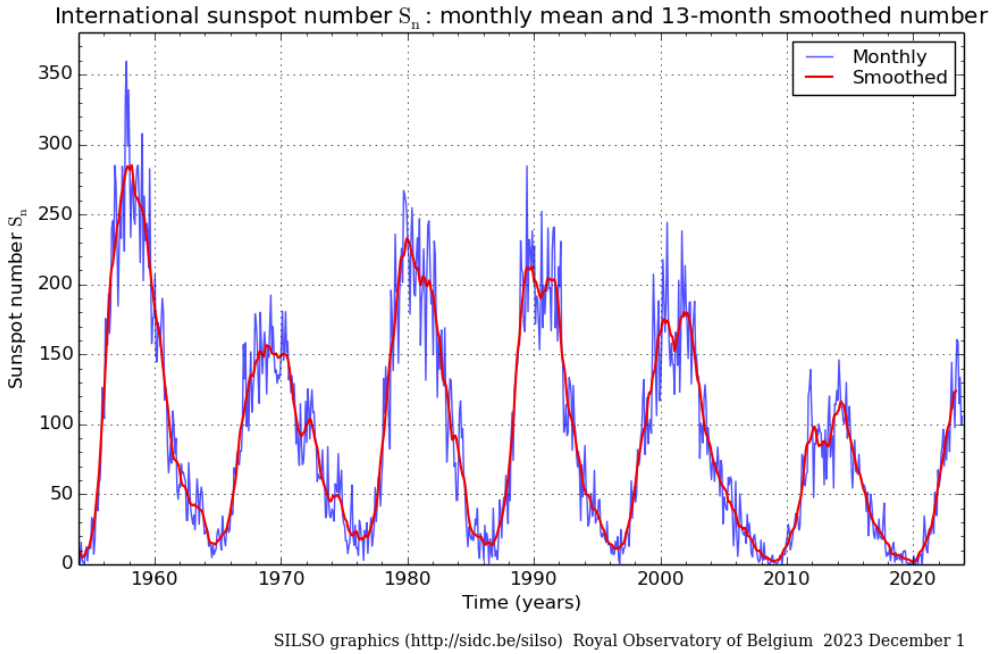

Figure 1.2: The monthly mean sunspot number (blue) and 13-month smoothed monthly sunspot number (red) for the last five solar cycles. Image courtesy of the Royal Observatory of Belgium.

1.1.5 Sunspots

The most visible feature about sunspots and pores is that they are darker than the quiet Sun. Sunspots are differentiated from pores because pores are smaller and don't have a penumbra (Solanki, 2003). This brightness signature is the basis for their identification (Solanki, 2003). Sunspots have a typical radius of 10 to 20 Mm

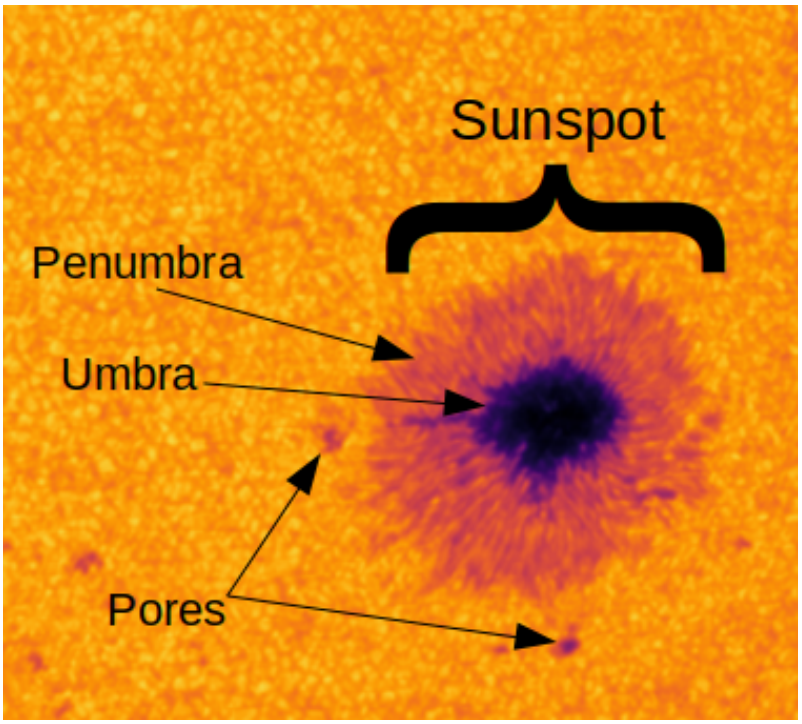

Figure 1.3: Continuum image of the solar photosphere showing sunspots, where the umbra and the penumbra are, and pores. Image recorded by SO/PHI (Solanki et al., 2020). More information on this instrument can be found on Chapter 4.

and consist of a central dark region, called the umbra, with a radius about 40 percent of the overall spot radius, surrounded by a less dark penumbra, with a filament like structure (Solanki, 2003). Their brightness, and therefore their temperature profiles change with the position within the spot. Compared to the quiet photosphere, the umbra radiates only 20 to 30 percent of the average flux density; while the penumbra radiates 75 to 85 percent (Priest, 2014b). The umbra at the surface is cooler than the photosphere by $1000 - 1900K$, while the penumbra is colder by $250 - 400K$ (Solanki, 2003). An example of a typical sunspot, with its umbra and penumbra, as well as of pores is displayed in Fig. 1.3.

The depletion in temperature and brightness in a sunspot occurs because the magnetic field inhibits the convection. The magnetic field within sunspots is nearly vertical in the umbra, while its strength leads to a plasma beta $\beta << 1$, so that the plasma within is dominated by the magnetic field.

The Lorentz force suppresses the motions across field lines below the solar surface so that most of the convection inside the sunspot's umbra is inhibited, and the temperature decreases vertically faster within the spot than in the surrounding region (Priest, 2014b).

In the radiative zone of the Sun the energy transport is by a random walk of the photons. In the convective zone the temperature gradient becomes super-adiabatic and convection sets in, taking over the energy transport. If the convection is suppressed by a strong magnetic field, less energy reaches the surface inside the sunspot in comparison to the quiet sun, and therefore sunspots appear dark. Part of this blocked energy is redistributed through diffusion in the convection zone within a timescale of one month to one year (Spruit, 1982). This additional redistributed heat

does not lead to a measurable increase in the temperature of the convection zone because of its large heat capacity. The excess blocked energy is released during a 10^5 year timescale through thermal relaxation (Spruit, 1982). This is known as the Kelvin-Helmholtz timescale.

The magnetic field in the center of the umbra is nearly vertical and increases with the overall size of the umbra, which is the part of the sunspot with the strongest magnetic field (Murray, 2013). The magnetic field strength in the umbra ranges from 1800 to $3700G$ in the umbra and varies within the sunspots, reaching a range of 700 to $1000G$ at the edge of the penumbra, resulting in an average over one sunspot of $1000 - 1500G$ (Solanki, 2003; Livingston, 2002). In the penumbra the inclination of the field increases with the radius, being close to vertical at the edge of the umbra and with a mean value of 70 to 80 degrees with respect to the vertical at the edge of the spot (Priest, 2014a).

A sunspot consists of an assembly of many small flux tubes that have progressively gathered into a single large flux tube in the solar plasma (Parker, 1979) brought to the surface by magnetic and convective forces, and swept together by photospheric flows (Stix, 2004).

A scenario for the formation and evolution of sunspots from Meyer et al. (1974) is as follows. A magnetic, Ω-shaped flux tube is brought up to the photosphere by buoyant forces in the convective zone. This flux tube has a magnetic field strength of over 1000 G, which is strong enough to dominate the plasma and resist the convection so that the plasma in the tube cools down and falls (see Eq. 1.15 and Fig. 1.4). Then the magnetic field strength increases to a point where the magnetic pressure within almost balances the external gas pressure. Around the flux tube an annular convection cell, called moat, is formed, with an upflow at the tube and an outflow into the surrounding photosphere.

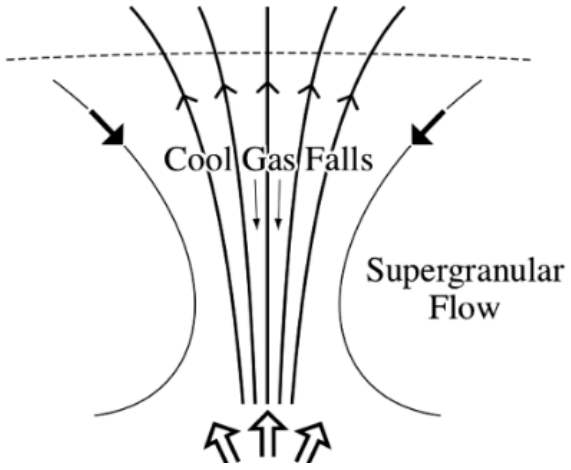

Figure 1.4: Scheme of a flux tube. From Priest (2014b).

1.1.6 The Wilson Depression

Early observations of sunspots indicate that the umbra of sunspots is situated at a lower geometrical height than the quiet Sun (Wilson, 1774). The penumbra of a sunspot on the solar limb side is foreshortened at a different rate than the one on

the observer's side, indicating that the geometrical height of the penumbra has a slope. Close to the limb, the umbra is often partly covered and can disappear from view. This is known as the Wilson effect, which is the basis to infer the existence of the Wilson depression within sunspots. A scheme of the Wilson effect is presented in Fig. 1.5.

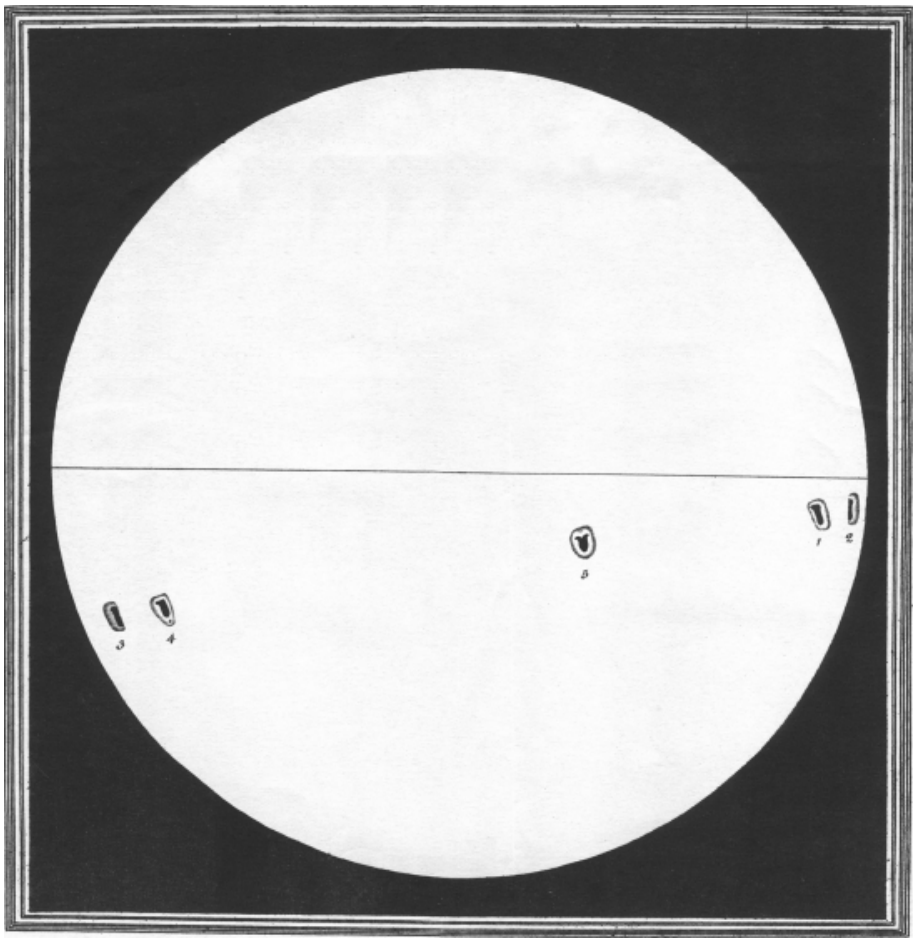

Figure 1.5: Scheme of the Wilson effect. The penumbra of a sunspot on the observer's far side is foreshortened at a different rate than the one on the near side. This effect grows towards the solar limb. Taken from Wilson (1774).

The Wilson depression refers to the fact that the visible radiation from the umbrae and penumbrae of sunspots emerges from a deeper geometrical layer than in the quiet Sun (Solanki, 2003). The optical depth τ is depressed to a lower height in the range $0.1 \leq \tau \leq 1$ (Gokhale & Zwaan, 1972). The $\tau = 1$ level within a sunspot is deeper than in the quiet Sun (see Fig. 1.7). This depression below the altitude level of the quiet Sun's surface is due to the strong magnetic field within the sunspots. The stronger magnetic pressure and curvature forces balance with the lower gas pressure within a sunspot and the lower opacity there. The height variation of the Wilson depression is therefore relevant for the understanding of the magnetic and geometric structure of sunspots and sets constraints on the strength and geometry of the magnetic field.

A magnetohydrostatic pressure balance model for sunspots from Meyer et al. (1977) considers a vertical flux tube with a static, axisymmetric field on a stratified atmosphere, $\mathbf{B}(R, z) = [B_R(R, z), 0, B_z(R, z)]$ in a volume V_i, surrounded by a field

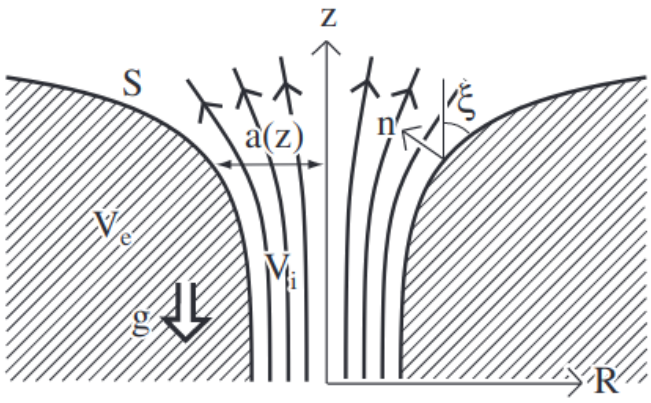

Figure 1.6: A magnetic flux rope surrounded by a field free plasma. Taken from Priest (2014b).

free region (V_e) (see Fig. 1.6). Assuming $B(R = 0) = B_i$ on the axis of the tube, and neglecting B outside of it, and naming the corresponding internal and external gas pressures $p_i(z)$ and $p_e(z)$, respectively, the equations for equilibrium within the flux tube and outside of it are

$$\nabla\left(p_i + \frac{B_i^2}{2\mu}\right) = \rho_i \mathbf{g} + (\mathbf{B_i} \cdot \nabla)\frac{\mathbf{B}_i}{\mu} \qquad \text{and} \qquad \nabla p_e = \rho_e \mathbf{g}, \tag{1.16}$$

respectively, with gravity g acting along the negative z–axis.

A first assumption is that the horizontal magnetic field is zero, such that $\mathbf{B}(R, z) = [0, 0, B_z(R, z)]$. At the interface between the flux tube and the photosphere the magnetic field drops discontinuously to zero. Therefore the total pressure balance at the interface at a given height z is

$$p_i(z) + \frac{B_i^2}{2\mu} = p_e(z) \;\text{ or }\; p_i(z) - p_e(z) = p_{mag,i}, \tag{1.17}$$

where $p_{mag} = B_i^2/2\mu$ is independent of height in the model. In this approximation the radial variations of B_z are not taken into account. Other models consider this variation or match the pressure gradient with its derivative at the interface (e.g. Simon & Weiss, 1970; Spruit, 1976; Simon et al., 1983).

Differentiating Eq. 1.17 with respect to z implies that $dp_e/dz = dp_i/dz$ if B is constant with z, and therefore, from Eq. 1.16 $\rho_i = \rho_e$ for this approximation. From Eq. 1.17 it can also be seen that $p_i < p_e$, or that the plasma pressure inside the spot is smaller than outside of it. Assuming the general gas law, the temperature deficit is therefore

$$\frac{T_i(z)}{T_e(z)} = 1 - \frac{B_i^2}{2\mu p_e(z)}. \tag{1.18}$$

This implies that the presence of a vertical magnetic field does not affect the plasma density, but results in a pressure (and therefore temperature) decrease in order to maintain the horizontal pressure balance given by $p(R, z) + B^2(R)/(2\mu)$. This result also implies the magnetic field lines will be straight only if the plasma's thermal equilibrium produces this particular form for the temperature difference.

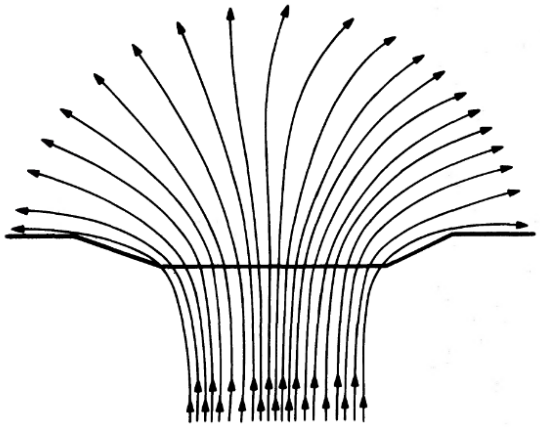

Figure 1.7: Sketch of a model of the magnetic field configuration within a sunspot. The thick horizontal line represents the $\tau = 1$ layer, or the visible surface of the Sun, showing the Wilson depression within the sunspot. From Parker (1979).

If ρ_i and ρ_e decrease, the pressures p_i and p_e decrease as well when T_i and T_e saturate and B_i^2 must decrease too, which results in and expansion of the flux with height.

According to Eq. 1.17, the maximum possible magnetic pressure inside of the flux tube can be equal to the external pressure. However, the magnetic pressure due to a sunspot with a magnetic field of 3000 G is $2.4{\times}10^4$ N m^{-2}, while the photospheric pressure is of 1.4×10^4 N m^{-2}, so that the condition set before is not fulfilled. The explanation for this is in the Wilson depression. Within sunspots, the magnetic field of the umbra is measured at a depth of hundreds of kilometers below the quiet Sun, where the ambient plasma pressure is higher. Additionally, with increasing height the ambient plasma pressure decreases, resulting in the magnetic field lines spreading out (Fig. 1.6), and therefore a decrease in the magnetic field strength. This decrease in the magnetic field strength with height means that the pressure gradient of the sunspot exceeds the external pressure value (Eq. 1.17), so that $T_i < T_e$ (Eq. 1.18). The opacity depends strongly on the temperature, so that at lower temperatures the opacity is reduced (Solanki, 2003), and one can see deeper into the Sun. This depressed $\tau = 1$ level is the Wilson depression.

There are many pressure balance models for sunspots,(e.g. Spruit, 1976; Meyer et al., 1977; Parker, 1979; Schmidt, 1991). However, these models estimate sunspots to be very shallow phenomena (Thomas & Weiss, 1992). These simple models are useful near the bottom photosphere, where the magnetic field can be assumed to be homogeneous and cylindrical and don't consider the curvature of the magnetic field lines expanding with height.

A more accurate approach (e.g. Prokakis, 1974; Maltby, 1977; Solanki, 2003; Löptien et al., 2018) considers again the radial force balance but now includes the horizontal magnetic field $B_R(R, z)$. The magnetohydrostatic equilibrium is again given by Eq. 1.16, and the magnetic field is now assumed to be a cylindrically symmetric, and untwisted (Fig. 1.6), but now the radial component is not zero. Then The force balance components are

$$-\frac{\partial p}{\partial R} + \frac{B_z}{\mu}\left(\frac{\partial B_R}{\partial z} - \frac{\partial B_z}{\partial R}\right) = 0, \quad \text{and} \quad -\frac{\partial p}{\partial z} + \frac{B_R}{\mu}\left(\frac{\partial B_R}{\partial z} - \frac{\partial B_z}{\partial R}\right) - \rho g = 0, \tag{1.19}$$

in radial and vertical direction, respectively. At the center of the sunspot, the vertical

component of Eq. 1.19 is simplified to $\partial p/\partial z = -\rho g$, and the radial force balance in can be re-written as

$$\frac{\partial p}{\partial R} = \frac{B_z}{\mu}\left(\frac{\partial B_R}{\partial z} - \frac{\partial B_z}{\partial R}\right). \tag{1.20}$$

Integrating radially the prior equation from the center of the sunspot (at $R = R_i$) to a point in the quiet Sun ($R = R_e$) gives

$$p(R_e) - p(R_i) = \frac{1}{2\mu}B_z^2(R) + \frac{1}{\mu}\int_{R_i}^{R_e} B_z \frac{\partial B_R}{\partial z} dR = \frac{1}{2\mu}B_z^2(R) + \frac{F_c}{2\mu}, \tag{1.21}$$

where F_c is the curvature integral

$$F_c = 2\int_{R_i}^{R_e} B_z(R') \frac{\partial B_R(R')}{\partial z} dR', \tag{1.22}$$

symbolizing the radially integrated curvature forces (Solanki, 2003).

As seen in the pure pressure balance models, if there are no curvature forces, the gas pressure is still in balance with the magnetic pressure if the magnetic field is straight vertically, as in Eq. 1.17. Considering only the pressure balance explains a decrease in temperature and brightness due to the strong magnetic field within sunspots, which leads to a reduced gas pressure, and therefore a decrease of the density and the opacity, resulting in a depression of a given τ layer in the solar surface. However, F_c must also be considered, since it plays a role in the force balance as important as the gas pressure does (Solanki, 2003).

Considering the pressure balance models, where the curvature force is assumed to be zero, the magnetic pressure is underestimated when only using B_z, and therefore the Wilson depression estimate is as well underestimated. This suggests that the role of F_C in determining the Wilson depression of a sunspot is important (Löptien et al., 2018). Assuming hydrostatic equilibrium, the magnetic pressure in the umbra can be directly derived from observations. However, the curvature force at the $\log\tau = 0$ layer can be estimated only in an indirect way (Löptien et al., 2020). A detailed study on how to estimate F_c and its dependance with different sunspot parameters, such as the magnetic field strength or the sunspot size is presented and discussed in Löptien et al. (2020).

Quantifying the Wilson depression sets constraints on the configuration of the magnetic field within in strength and geometry, making this quantity a relevant problem for stereoscopy.

The Wilson depression has been previously estimated with different methods and approaches. Early quantitative approximations of the depth of the Wilson Depression were based on how the relative sizes of the umbra and penumbra change, parallel and transverse to the solar disk's radial direction, as the sunspots approach the solar limb (Prokakis, 1974; Gokhale & Zwaan, 1972).

From 131 spot observations, Prokakis (1974) obtained depth values in the range between 690 to 2100 km and found typically deeper depressions within larger sunspots. The geometrical altitude of $\tau = 1$, however, depends on the viewing angle. Therefore different altitude surfaces are detected during the passage of the sunspot through the solar disk (Solanki et al., 1993), being a disadvantage for the method of Prokakis (1974), despite it being a direct method to quantify the Wilson depression.

Furthermore, sunspots evolve as well while they move from the disk center to the limb, and the relative sizes of umbra to penumbra may change due to this evolution.

Beyond the observational method described above, attempts to estimate the Wilson depression using indirect methods have been made. Martínez Pillet and Vázquez (1993) studied the distribution of continuum intensity and the increase in magnetic pressure within the umbra of several sunspots. Under the assumption that the horizontal forces across the sunspot are balanced and that the tension forces are of the same order of magnitude as the magnetic pressure, they obtain typical depths in sunspots of about 600 km, averaged over all the local depressions of all points throughout the umbra.

A linear relation between the gas temperature and the vertical magnetic field was obtained by studying the infrared emission through one sunspot. According to a quantitative model of the magnetic and thermal force balance, Solanki et al. (1993) found an average Wilson depression of about 400 km in the studied sunspot, even though the depth varies as a function within the sunspot, with a qualitative radial dependence, which agrees with what was found by Wilson and Cannon (1968) when studying the Wilson effect. However, the results of methods using quantitative estimates of the curvature force, e.g. from Solanki et al. (1993) and Martínez Pillet and Vázquez (1993) have some uncertainty, since the curvature force estimates are as well uncertain.

Puschmann et al. (2010) inverted spectropolarimetric observations of small patches in the penumbra and then fitted to a 3D MHD model of the solar atmosphere above them. It was found that the surface of the penumbra declined around 300 km over a horizontal extension of 4 Mm in this regions.

An extension of the work of Puschmann et al. (2010) onto an entire sunspot was conducted by Löptien et al. (2020). As constraints for fitting the observations they used a vanishing magnetic field divergence and a magnetic force in balance with the gas pressure. Under these two constraints, for a modelled sunspot they found a depression of the umbra of 500 and 700 km.

There is still a considerably large uncertainty in the Wilson depression's depth estimates, which arises from uncertainties in the applied estimation techniques.

It has been found that generally the larger sunspots tend to have stronger magnetic fields and lower umbra temperatures (see, e.g., Kopp & Rabin, 1992; Schad, 2014; Watson et al., 2014; Rezaei et al., 2015). This relation suggests that a dependence of the sunspots' depth with its size may also exist. This has already been shown in the results of (Löptien et al., 2020), but this relation is still not well known, due to the uncertainties in the current depth estimates.

In this work a new method to estimate the depth on sunspots, based on direct observations and stereoscopic analysis is proposed.

1.2 Stereoscopy

Computer vision aims to study properties of digital images which represent a three dimensional world. As the name suggests, computers are used to interpret images to retrieve geometric or dynamic information about the objects in them. There are many different algorithms and tools for computer vision, stereoscopy being one of them.

Stereoscopy is understood as an image analysis by which 3-dimensional information is retrieved from two or more images by identifying a feature from two different vantage points and using their image position to reconstruct their relative 3D position. Stereoscopy includes a wide range of techniques and applications in different fields of technology and science, going from microscopy to star parallax measurements.

A prerequisite of stereoscopy is to identify corresponding features between images. Stereoscopy is a promising tool to retrieve 3D information if the images have clear identifiable features and if the calibration between the cameras is correct. In stereoscopy, the term calibration refers to the determination of the camera resolution, position, attitude and view direction.

Two key problems to be solved when performing a stereoscopic analysis are the correspondence problem and the reconstruction problem. A correspondence is the relationship established between the two projections of one object in the two stereoscopic images (Inhester, 2006). Generally, the approaches to find correspondences between images are based on correlation methods or feature based methods (Trucco & Verri, 1998). While clear identifiable features allow the feature based methods to be used, due to the nature of the structures studied here, the analysis performed in this work requires a statistical correlation-based approach.

Once the correspondence of features between images has been found, the 3D reconstruction can be performed. This requires additional spatial and geometrical information. It is convenient to transform the problem from three-dimensions to a set of two-dimensional problems by finding an adequate coordinate system for the problem (Inhester, 2006). One suitable set of coordinate systems is based on epipolar planes.

Given a set of two images of the same scene, the plane connecting a feature in that scene with each of the observing cameras A and B is the epipolar plane. On this plane lies a line that connects both cameras, say r_{AB}. A feature in the observed scene is projected onto each of the images. The viewing line from that observer to the feature appears in the image of this observer as a point and in the image of the other observer as a straight line, the epipolar line of that feature. The point along the r_{AB} line on which all epipolar lines of one image connect is called the epipole of that image. A representation of epipolar planes and epipolar lines is displayed in Fig. 1.12 in Section 1.2.2, where these topics are discussed in more detail.

The difference in position of corresponding features between images along corresponding epipolar lines, is called disparity. If the spatial configuration and epipolar geometry of the system, comprised of both cameras and the observed object, as well as the disparity are known, then the 3D information of the image can be retrieved. Therefore, the geometric configuration of the system, the camera parameters and a set of algorithms are required to perform stereoscopy.

In this chapter the equations of stereoscopy (see Trucco & Verri, 1998) needed for stereoscopic analysis will be reformulated so they can be used for solar stereoscopic observations. Most of these observations are formatted as FITS files (see Greisen & Calabretta, 2002; Thompson, 2006). The reformulation made in this work is tuned to use specifically the metadata of these files.

1.2.1 Camera Model and FITS Parameters

FITS, or Flexible Image Transport System, is the standard format for data used in astronomy. It is used for transport and analysis of scientific data sets. FITS files can contain multi-dimensional arrays, images and headers, which contain keywords that describe the contained data. These header keywords are key for stereoscopic analysis since they contain information about camera parameters, and scientific coordinate systems, that describe the location of each pixel in an image, but also in a world coordinate system (Wells & Greisen, 1979; Ponz et al., 1994). The relevant FITS header keywords, besides from the 3D spacecraft coordinates, are displayed in table 1.1. These are the quantities needed for the stereoscopic analysis presented here.

Computer vision methods require to link the coordinates of points in a 3D world system to their corresponding points in image coordinates. For this it is assumed that the camera reference frame can be located with respect to some other reference frame; and that the coordinates of the image points in the camera's reference frame can be derived from the pixel coordinates, which are the only ones directly available from the image (Trucco & Verri, 1998). Knowing this camera characteristics, or parameters, helps to build a camera model in order to be able to link features from an image to the 3D world and vice versa.

Keyword	**[units]**	**Description**
CRPIX1	[pixel]	Position of reference pixel along x-axis
CRPIX2	[pixel]	Position of reference pixel along y-axis
CDELT1	[arcsec/pixel]	image scale along x-axis
CDELT2	[arcsec/pixel]	image scale along y-axis
CRVAL1	[arcsec]	Coordinates of reference pixel along x-axis
CRVAL2	[arcsec]	Coordinates of reference pixel along y-axis
CROTA	[deg]	Image rotation angle with respect to the projected solar axis

Table 1.1: Description of the FITS header keywords needed for the streoscopic method presented in this work.

Intrinsic Camera Parameters

For the stereoscopic analysis of solar images, a pinhole or perspective projection camera system is a valid model since the object that cameras designed for solar observations look at is at a much larger distance than the camera or telescope's focal length, f. It is assumed that the images are undistorted and that therefore the projection from the 3D world onto the camera's focal plane has a pinhole camera perspective.

In this pinhole perspective system, the pixel coordinates (p_x, p_y) of a feature on an image and the viewing tangents of the angles ϕ_x, ϕ_y of this feature in the image a with respect to the camera's optical axis are related by (see Fig. 1.8)

$$\begin{pmatrix} t_x \\ t_y \end{pmatrix} = \begin{pmatrix} \tan\phi_x \\ \tan\phi_y \end{pmatrix} = \begin{pmatrix} p_x - \texttt{CRPIX1} \\ p_y - \texttt{CRPIX2} \end{pmatrix} \frac{\Delta_{\text{pix}}}{f} \tag{1.23}$$

$$[(p_x, p_y) \text{ in pixels, } (t_x, t_y) \text{ dimensionless}]$$

where Δ_{pix} is the physical size of the image pixels, which is assumed to be the same in the p_x and p_y coordinates, and f the focal length. The FITS header keywords `CRPIX1` and `CRPIX2` correspond to pixel coordinates of the optical axis in the FITS images. An image can then be constructed as in Fig. 1.8 on a virtual plane which is normal to the camera's optical axis and at a distance f away from the camera's center.

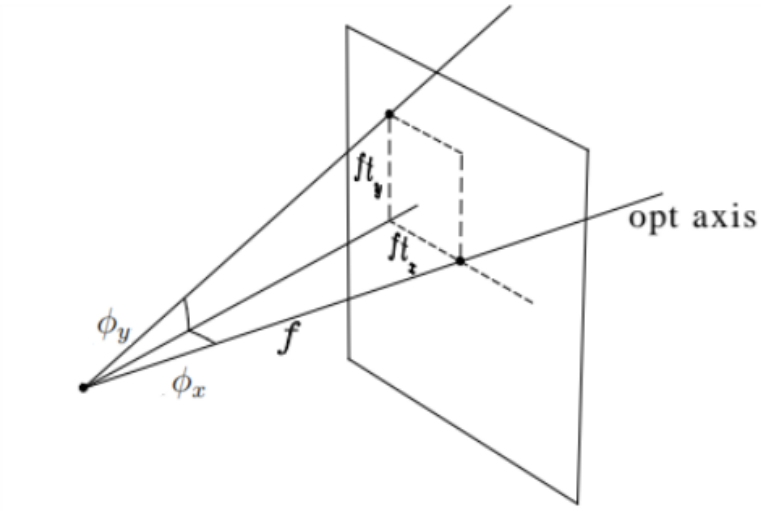

Figure 1.8: Illustration of the pinhole camera geometry with perspective projection as in Eq. 1.23

Since the angles ϕ_x, ϕ_y are very small, the tangent function in Eq. 1.23 can be replaced by the identity function, and the view angle converted from radians to arc seconds by using the constant $1\,\text{rad} = \frac{180}{\pi} \cdot 3600'' = 648000''/\pi$

$$\begin{pmatrix}\phi_x\\ \phi_y\end{pmatrix} \simeq \begin{pmatrix}p_x - \texttt{CRPIX1}\\ p_y - \texttt{CRPIX2}\end{pmatrix} \frac{\Delta_{\text{pix}}}{f} \frac{648000''}{\pi} = \begin{pmatrix}(p_x - \texttt{CRPIX1})\ \texttt{CDELT1}\\ (p_y - \texttt{CRPIX2})\ \texttt{CDELT2}\end{pmatrix} \tag{1.24}$$

$$[(p_x, p_y) \text{ in pixels, } (\phi_x, \phi_y) \text{ in arc seconds}]$$

The FITS header values for the camera's plate scale are `CDELT1` and `CDELT2`, respectively. The plate scale of a camera relates the angular separation of an object with the linear separation on its virtual image at the focal plane of the camera. Two values are given because detector chips might not have square pixels, so Δ_{pix} might be different for the image x and y axes. In this work square pixels are assumed.

A 2D vector of the viewing tangents from the image pixel coordinates is obtained by

$$\begin{pmatrix}t_x\\ t_y\end{pmatrix} = \begin{pmatrix}(p_x - \texttt{CRPIX1})\ \texttt{CDELT1}\\ (p_y - \texttt{CRPIX2})\ \texttt{CDELT2}\end{pmatrix} \frac{\pi}{648000''} \qquad \text{[dimensionless]}. \tag{1.25}$$

The two pixel coordinates can be extended by a third scaling coordinate, giving a homogeneous coordinate vector. Using a homogeneous coordinate vector is

customary and also helpful for the analysis of perspective projection. A specific homogeneous vector obtained from calculations, can be transformed to a normal form by dividing it by its last element. The resulting other elements then represent the physically relevant coordinates. By using homogeneous coordinates, (1.25) can be rewritten as a plain matrix multiplication

$$\begin{pmatrix} t_x \\ t_y \\ 1 \end{pmatrix} \propto \mathbf{K} \begin{pmatrix} p_x \\ p_y \\ 1 \end{pmatrix}, \qquad \mathbf{K} = \frac{\pi}{648000''} \begin{pmatrix} \texttt{CDELT1} & 0 & -\texttt{CRPIX1} \cdot \texttt{CDELT1} \\ 0 & \texttt{CDELT2} & -\texttt{CRPIX2} \cdot \texttt{CDELT2} \\ 0 & 0 & \frac{648000''}{\pi} \end{pmatrix}. \quad (1.26)$$

The $\propto$ sign in Eq. 1.26 implies the transformation of the vector on the right-hand side to normal form, i.e. the multiplication with an adequate scale factor, before the left hand side is obtained. The matrix $\mathbf{K}$ combines all intrinsic camera parameters. Its inverse is also needed

$$\mathbf{K}^{-1} = \begin{pmatrix} \frac{648000''}{\pi}\texttt{CDELT1}^{-1} & 0 & \texttt{CRPIX1} \\ 0 & \frac{648000''}{\pi}\texttt{CDELT2}^{-1} & \texttt{CRPIX2} \\ 0 & 0 & 1 \end{pmatrix} \quad (1.27)$$

The coordinates (t_x, t_y) of the view direction tangents with the optical axis are also called normalized coordinates (Hartley & Zisserman, 2004). The normalized coordinates will be often used as synonyms for pixel coordinates in this text, since the relation to the real pixel coordinates is always as given in Eq. 1.26.

Since $\mathbf{t} = (t_x, t_y)$ is a vector on the retinal plane (see Fig. 1.8), its homogeneous version $(t_x, t_y, 1)$ is a three dimensional vector along the view direction. Its angle with the optical axis is

$$\phi = \arccos\Big[\frac{\begin{pmatrix} t_x \\ t_y \\ 1 \end{pmatrix}^{\mathsf{T}} \begin{pmatrix} 0 \\ 0 \\ 1 \end{pmatrix}}{\sqrt{1 + t_x^2 + t_y^2}}\Big] = \arccos \frac{1}{\sqrt{1 + t^2}} = \arctan \|\mathbf{t}\|. \quad (1.28)$$

Using the tangents of the angles is simpler than using the angles themselves. However, the angle between two arbitrary view directions (t_{1x}, t_{1y}) and (t_{2x}, t_{2y}) gives a more involved formula, which can be cast into a form equivalent to (1.28)

$$\phi = \arccos\Big[\frac{\begin{pmatrix} t_{1x} \\ t_{1y} \\ 1 \end{pmatrix}^{\mathsf{T}} \begin{pmatrix} t_{2x} \\ t_{2y} \\ 1 \end{pmatrix}}{\sqrt{1 + t_{1x}^2 + t_{1y}^2}\sqrt{1 + t_{2x}^2 + t_{2y}^2}}\Big] = \arccos \frac{1 + \mathbf{t}_1^{\mathsf{T}}\mathbf{t}_2}{\sqrt{(1 + t_1^2)(1 + t_2^2)}}$$

$$= \arctan\Big[\frac{(1 + t_1^2)(1 + t_2^2)}{(1 + \mathbf{t}_1^{\mathsf{T}}\mathbf{t}_2)^2} - 1\Big]^{1/2} = \arctan \frac{((1 + t_1^2)(1 + t_2^2) - (1 + \mathbf{t}_1^{\mathsf{T}}\mathbf{t}_2)^2)^{1/2}}{1 + \mathbf{t}_1^{\mathsf{T}}\mathbf{t}_2}$$

$$= \arctan \frac{(\|\mathbf{t}_1 - \mathbf{t}_2\|^2 + t_1^2 t_2^2 - (\mathbf{t}_1^{\mathsf{T}}\mathbf{t}_2)^2)^{1/2}}{1 + \mathbf{t}_1^{\mathsf{T}}\mathbf{t}_2} = \arctan \|\mathbf{t}_1 - \mathbf{t}_2\|^2 + \mathcal{O}(t^4) \quad (1.29)$$

for small magnitudes of t . In general, the optical axis is therefore a particular direction and the angles and distances in the retinal plane are not equivalent unless the angles are small. The symbol $^{\mathsf{T}}$ denotes the transposition of a vector, so that $()^{\mathsf{T}}()$ refers to the inner product of two vectors, and is used throughout this work.

Extrinsic Camera Parameters

Given a set of normalized 2D pixel coordinates in an image, linking them to the 3D world requires knowing the 3D position of the camera, $\mathbf{r}_{\mathrm{SC}}$, and its attitude defined by an orthogonal 3D axis system $(\hat{\mathbf{e}}_x, \hat{\mathbf{e}}_y, \hat{\mathbf{e}}_z)$. The subscript $_{\mathrm{SC}}$ corresponding to spacecraft, will be used to refer to the cameras, since for this stereoscopic analysis the two used cameras will be on board spacecraft. Here, $\hat{\mathbf{e}}_x$ and $\hat{\mathbf{e}}_y$ are 3D directions aligned with the horizontal and vertical edges of the detector chip and $\hat{\mathbf{e}}_z$ is normal to the detector plane. For standard detectors $\hat{\mathbf{e}}_z$ should agree with the optical axis of the telescope. Therefore the view direction associated with a pixel coordinate is (see Fig. 1.8)

$$\mathbf{v}(t_x, t_y) \propto t_x\hat{\mathbf{e}}_x + t_y\hat{\mathbf{e}}_y + \hat{\mathbf{e}}_z = \hat{\mathbf{R}}\begin{pmatrix} t_x \\ t_y \end{pmatrix} + \hat{\mathbf{e}}_z = \mathbf{R}\begin{pmatrix} t_x \\ t_y \\ 1 \end{pmatrix} \tag{1.30}$$

$$\hat{\mathbf{R}} = [\hat{\mathbf{e}}_x, \hat{\mathbf{e}}_y], \qquad \mathbf{R} = [\hat{\mathbf{e}}_x, \hat{\mathbf{e}}_y, \hat{\mathbf{e}}_z]$$

and any object seen in this pixel must lie on the line $\mathbf{r}_{\mathrm{SC}} + \alpha\mathbf{v}$ where the distance $\alpha > 0$ is unknown. The 3×2 matrix $\hat{\mathbf{R}}$ has the the unit vectors $\hat{\mathbf{e}}_x, \hat{\mathbf{e}}_y$ as columns and its extension to $\mathbf{R}$ is required for homogeneous coordinates.

While the intrinsic camera parameters are listed directly in the FITS header of the images, the extrinsic parameters are not. The spacecraft position $\mathbf{r}_{\mathrm{SC}}$ is given in the FITS header for some 3D coordinate systems. As long as all 3D vectors are noted in the same coordinate system, it does not matter which one is used, but due to the nature of the problem it is very convenient if a heliocentric 3D coordinate system is chosen so that $\mathbf{r} = 0$ for the solar center. It is also convenient to choose a coordinate system in which its third axis is aligned to the solar rotation axis, $\boldsymbol{\Omega} = (0, 0, 1)^{\mathsf{T}}$. In this work we will use the Heliocentric Earth Equatorial coordinate system (HEEQ), for which the first axis is directed to the projection of Earth onto the heliographic equator (see Thompson, 2006). The FITS header keywords for the 3D components of $\mathbf{r}_{\mathrm{SC}}$ are `HEQX_OBS`, `HEQY_OBS`, `HEQZ_OBS` in units of meters.

The columns of the matrix $\mathbf{R}$ are not given in the header, so they must be constructed from the observation of the Sun center $\mathbf{r} = 0$ and the direction of the projected solar rotation axis in the image.

The image vector from the Sun center to the optical axis is given in the FITS header as `CRVAL1`, `CRVAL2` in arc seconds, therefore

$$\mathbf{t}_\odot = \begin{pmatrix} t_{x\odot} \\ t_{y\odot} \end{pmatrix} = -\frac{-\pi}{684000''}\begin{pmatrix} \texttt{CRVAL1} \\ \texttt{CRVAL2} \end{pmatrix} \tag{1.31}$$

are the normalized pixel coordinates of the solar center in the image. In order to define the view ray vector $\mathbf{v}$ in Eq. 1.30 uniquely and for it to have a dimension of length we multiply it with the distance $d_\odot$

$$\mathbf{v}(t_x, t_y) = d_\odot[\hat{\mathbf{R}}\begin{pmatrix} t_x \\ t_y \end{pmatrix} + \hat{\mathbf{e}}_z] = d_\odot\mathbf{R}\begin{pmatrix} t_x \\ t_y \\ 1 \end{pmatrix}, \tag{1.32}$$

which will be determined as follows. A general point $\mathbf{r}$ projects to a pixel (t_x, t_y) with a well defined distance parameter α

$$\mathbf{r}(t_x, t_y, \alpha) = \mathbf{r}_{\mathrm{SC}} + \alpha\mathbf{v}(t_x, t_y). \tag{1.33}$$

By demanding that the view ray to the Sun center has the parameter $\alpha = 1$, $d_\odot$ and α are uniquely defined so that

$$\mathbf{r}(t_{x\odot}, t_{y\odot}, 1) = \mathbf{r}_{\mathrm{SC}} + d_\odot[\hat{\mathbf{R}} \begin{pmatrix} t_{x\odot} \\ t_{y\odot} \end{pmatrix} + \hat{\mathbf{e}}_z] = 0. \tag{1.34}$$

$\mathbf{r}(t_{x\odot}, t_{y\odot}, 1)$ points to the origin of the 3D coordinate system. Comparing the magnitudes of both sides of Eq. 1.34 yields

$$d_\odot = \frac{||\mathbf{r}_{\mathrm{SC}}||}{\sqrt{1 + t_\odot^2}}. \tag{1.35}$$

Now the correct axes in $\mathbf{R}$ have to be obtained. The information provided by the FITS header is indirect: it contains only the the pixel position of the Sun center and a roll angle around the optical axis that is provided in the form of a symmetric 2x2 image rotation matrix $\mathbf{P}$ given by its elements $\mathbf{P}_{11} = \mathbf{P}_{22} = \cos\omega$ and $\mathbf{P}_{21} = -\mathbf{P}_{12} = \sin\omega$. This matrix rotates all pixels (t_x, t_y) from the optical axis by an angle ω so that the rotation axis Ω of the Sun is seen parallel to the image y-axis:

$$\begin{pmatrix} t'_{x\odot} \\ t'_{y\odot} \end{pmatrix} = \mathbf{P}(\omega) \begin{pmatrix} t_{x\odot} \\ t_{y\odot} \end{pmatrix} = \begin{pmatrix} \cos\omega & -\sin\omega \\ \sin\omega & \cos\omega \end{pmatrix} \begin{pmatrix} t_{x\odot} \\ t_{y\odot} \end{pmatrix}.$$

The ω is the angle of the projected solar rotation axis with the image $\hat{\mathbf{e}}_y$ axis. Therefore if $\mathbf{P}$ is applied to a pixel proportional to (Ω_x, Ω_y) on the projected solar rotation axis, it will be rotated parallel to the vertical image edge,

$$\begin{pmatrix} \Omega'_x \\ \Omega'_y \end{pmatrix} = \mathbf{P}(\omega) \begin{pmatrix} \Omega_x \\ \Omega_y \end{pmatrix} = \begin{pmatrix} 0 \\ 1 \end{pmatrix}, \quad \text{so} \begin{pmatrix} \Omega_x \\ \Omega_y \end{pmatrix} \propto \begin{pmatrix} \sin\omega \\ \cos\omega \end{pmatrix}.$$

The matrix $\mathbf{P}$ is equivalent to the roll angle ω, which together with the Sun center pixel coordinates $t_\odot$ and the direction $\mathbf{r}_{\mathrm{SC}}/||\mathbf{r}_{\mathrm{SC}}||$ of the spacecraft position provides the three parameters needed to determine $\mathbf{R}$ in the HEEQ coordinate system.

We use Eq. 1.34 for that purpose and solve for the 3D axis system $\mathbf{R}$ by iteration until Eq. 1.34 is satisfied and the projection of $\boldsymbol{\Omega}$ into the image plane is parallel to $\hat{\mathbf{e}}_y^{(n)}$. The final x, y-axes are then rotated by $\mathbf{P}^{\mathsf{T}}$ so that $\boldsymbol{\Omega}$ makes an angle ω with the image y-axis.

$$\begin{aligned}
&\text{initiate } n = 0, && \begin{pmatrix} t'_{x\odot} \\ t'_{y\odot} \end{pmatrix} = \mathbf{P}(\omega) \begin{pmatrix} t_{x\odot} \\ t_{y\odot} \end{pmatrix}, \quad \hat{\mathbf{e}}_z^{(0)} = -\frac{\mathbf{r}_{\mathrm{SC}}}{||\mathbf{r}_{\mathrm{SC}}||} \\
&\text{iterate } n = n + 1, && \hat{\mathbf{e}}_x^{(n)} = \frac{\hat{\mathbf{e}}_z^{(n-1)} \times \boldsymbol{\Omega}}{|\hat{\mathbf{e}}_z^{(n-1)} \times \boldsymbol{\Omega}|}, \quad \hat{\mathbf{e}}_y^{(n)} = \hat{\mathbf{e}}_x^{(n)} \times \hat{\mathbf{e}}_z^{(n-1)}, \quad \text{(orthogonality)} \\
& && \hat{\mathbf{e}}_z^{(n)} = -\frac{\mathbf{r}_{\mathrm{SC}}}{d_\odot} - (\hat{\mathbf{e}}_x^{(n)}, \hat{\mathbf{e}}_y^{(n)}) \begin{pmatrix} t'_{x\odot} \\ t'_{y\odot} \end{pmatrix} \quad \text{(intersection with Sun center)} \\
& && \hat{\mathbf{e}}_z^{(n)} = \frac{\hat{\mathbf{e}}_z^{(n)}}{||\hat{\mathbf{e}}_z^{(n)}||}, \qquad \text{(normalization)} \\
&\text{after convergence} && \hat{\mathbf{R}} = [\hat{\mathbf{e}}_x^{(n)}, \hat{\mathbf{e}}_y^{(n)}]\mathbf{P}(\omega), \qquad \mathbf{R} = [\hat{\mathbf{R}} \mid \hat{\mathbf{e}}_z^{(n)}]
\end{aligned}$$

The iteration converges in a few steps. The first line in the iteration ensures orthogonality and also makes sure that the solar rotation axis lies in the $\hat{\mathbf{e}}_y, \hat{\mathbf{e}}_z$ plane. All the camera's extrinsic parameters except $\mathbf{r}_{\mathrm{SC}}$ are now contained in $\hat{\mathbf{R}}$.

Relation from a pixel to a view ray

The relation from a pixel to a point $\mathbf{r}$ on the image ray combines intrinsic and extrinsic parameters. From (1.33)

$$\mathbf{r}(t_x, t_y, \alpha) = \mathbf{r}_{\mathrm{SC}} + \alpha d_\odot \mathbf{R} \begin{pmatrix} t_x \\ t_y \\ 1 \end{pmatrix} = \mathbf{r}_{\mathrm{SC}} + \alpha d_\odot \mathbf{R}\mathbf{K} \begin{pmatrix} p_x \\ p_y \\ 1 \end{pmatrix}. \tag{1.36}$$

In reverse direction, any point along the same ray will map to the same pixel and the corresponding mapping should be independent of the distance $\alpha d_\odot$. This is the advantage of using homogeneous coordinates.

Given that $\mathbf{R}$ is orthogonal

$$\begin{pmatrix} p_x \\ p_y \\ 1 \end{pmatrix} \propto \mathbf{K}^{-1} \begin{pmatrix} t_x \\ t_y \\ 1 \end{pmatrix}, \quad \begin{pmatrix} t_x \\ t_y \\ 1 \end{pmatrix} \propto \mathbf{R}^{\mathsf{T}} (\mathbf{r} - \mathbf{r}_{\mathrm{SC}}), \tag{1.37}$$

where the factor $\alpha d_\odot$ is absorbed by the proportionality for homogeneous image coordinates as explained above in Section 1.2.1. Any point along the view ray is equivalent so we can simply choose a point at a distance $\alpha d_\odot = 1$.

As well as for the view ray, we also want to introduce homogeneous coordinates for the 3D vector $\mathbf{r}$. The step is similar to the step which led from (1.25) to (1.26):

$$\begin{pmatrix} t_x \\ t_y \\ 1 \end{pmatrix} \propto [\mathbf{R}^{\mathsf{T}} \mid -\mathbf{R}^{\mathsf{T}} \mathbf{r}_{\mathrm{SC}}] \begin{pmatrix} \mathbf{r} \\ 1 \end{pmatrix}. \tag{1.38}$$

Therefore mapping a 3D world point to true image pixel coordinates is given by

$$\begin{pmatrix} p_x \\ p_y \\ 1 \end{pmatrix} \propto \mathbf{K}^{-1} \begin{pmatrix} t_x \\ t_y \\ 1 \end{pmatrix} \propto \mathbf{P} \begin{pmatrix} \mathbf{r} \\ 1 \end{pmatrix}, \qquad \mathbf{P} = \mathbf{K}^{-1} [\mathbf{R}^{\mathsf{T}} \mid -\mathbf{R}^{\mathsf{T}} \mathbf{r}_{\mathrm{SC}}]. \tag{1.39}$$

The 3×4 matrix $\mathbf{P}$ is the perspective projection matrix (PPM).

Without homogeneous coordinates, the calculation equivalent to (1.38) and (1.39) is

$$\begin{pmatrix} t_x \\ t_y \end{pmatrix} = \begin{pmatrix} \hat{\mathbf{e}}_x^{\mathsf{T}} \\ \hat{\mathbf{e}}_y^{\mathsf{T}} \end{pmatrix} \frac{\mathbf{r} - \mathbf{r}_{\mathrm{SC}}}{\hat{\mathbf{e}}_z^{\mathsf{T}} (\mathbf{r} - \mathbf{r}_{\mathrm{SC}})}, \qquad \begin{pmatrix} p_x \\ p_y \end{pmatrix} = \begin{pmatrix} \mathtt{CRPIX1} \\ \mathtt{CRPIX2} \end{pmatrix} + \hat{\mathbf{K}}^{-1} \begin{pmatrix} t_x \\ t_y \end{pmatrix} \tag{1.40}$$

where $\hat{\mathbf{K}}^{-1}$ is the upper left 2×2 submatrix of $\mathbf{K}^{-1}$ in (1.27).

Intersection of a view ray with the solar surface

Any point on the solar surface can be characterised by its 3D position and its distance from the solar center, $\mathbf{r}_{\mathrm{srf}} = r_{\mathrm{srf}} \hat{\mathbf{r}}$. For the distance we write $r_{\mathrm{srf}} = R_\odot + dh(\hat{\mathbf{r}})$, where $R_\odot$ is the standard solar radius. All the surface height variations are in the direction $dh(\hat{\mathbf{r}})$ where the unit vector $\hat{\mathbf{r}}$ defines the coordinates on the solar surface. When using the HEEQ coordinate system, $\hat{\mathbf{r}}$ can be expressed in Stonyhurst longitude Φ and latitude Θ:

$$\hat{\mathbf{r}} = \begin{pmatrix} \cos\Theta \sin\Phi \\ \cos\Theta \cos\Phi \\ \sin\Theta \end{pmatrix}.$$

Mapping the surface coordinates $\hat{\mathbf{r}}$ to pixels (t_x, t_y) is straight forward using, for example, Eq. 1.40 and inserting $\mathbf{r} = (R_\odot + dh(\hat{\mathbf{r}}))\hat{\mathbf{r}}$ on the right hand side.

$$\begin{pmatrix} t_x \\ t_y \end{pmatrix} = \begin{pmatrix} \hat{\mathbf{e}}_x^\mathsf{T} \\ \hat{\mathbf{e}}_y^\mathsf{T} \end{pmatrix} \frac{(h_{\mathrm{ref}} + dh(\hat{\mathbf{r}}))\hat{\mathbf{r}} - \mathbf{r}_{\mathrm{SC}}}{\hat{\mathbf{e}}_z^\mathsf{T}((h_{\mathrm{ref}} + dh(\hat{\mathbf{r}}))\hat{\mathbf{r}} - \mathbf{r}_{\mathrm{SC}})}.$$

The reverse map from (t_x, t_y) to $\hat{\mathbf{r}}$ or equivalently to α_{srf} can only be written down implicitly. Starting from (1.33), and demanding that the length of $\mathbf{r}$ has the correct distance from the solar center $\|\mathbf{r}\| = r_{\mathrm{srf}} = R_\odot + dh(\hat{\mathbf{r}})$, or

$$\|\mathbf{r}_{\mathrm{SC}} + \alpha_{\mathrm{srf}}\mathbf{v}(t_x, t_y)\|^2 = r_{\mathrm{srf}}^2. \tag{1.41}$$

Now, only the correct distance parameter α_{srf} has to be found. Requirement (1.41) gives

$$\begin{aligned} r_{\mathrm{srf}}^2 = r_{\mathrm{SC}}^2 + 2\alpha_{\mathrm{srf}}\mathbf{r}_{\mathrm{SC}}^\mathsf{T}\mathbf{v}(t_x, t_y) + \alpha_{\mathrm{srf}}^2\|\mathbf{v}(t_x, t_y)\|^2 \qquad &\text{or} \\ 0 = \frac{r_{\mathrm{SC}}^2 - r_{\mathrm{srf}}^2}{\|\mathbf{v}(t_x, t_y)\|^2} + 2\alpha_{\mathrm{srf}}\frac{\mathbf{r}_{\mathrm{SC}}^\mathsf{T}\mathbf{v}(t_x, t_y)}{\|\mathbf{v}(t_x, t_y)\|^2} + \alpha_{\mathrm{srf}}^2 \qquad &\text{or} \\ \alpha_{\mathrm{srf}} = -b \pm \sqrt{b^2 - c}, \end{aligned} \tag{1.42}$$

where the coefficients can be calculated using (1.32), (1.35) and (1.34). Since $\mathbf{R}$ is orthogonal,

$$\|\mathbf{v}(t_x, t_y)\|^2 = d_\odot^2\|\mathbf{R}\begin{pmatrix} t_x \\ t_y \\ 1 \end{pmatrix}\|^2 = d_\odot^2(1 + t^2) = r_{\mathrm{SC}}^2\frac{1 + t^2}{1 + t_\odot^2} \tag{1.43}$$

$$\mathbf{r}_{\mathrm{SC}}^\mathsf{T}\mathbf{v}(t_x, t_y) = -d_\odot^2(\mathbf{R}\begin{pmatrix} t_{x\odot} \\ t_{y\odot} \\ 1 \end{pmatrix})^\mathsf{T}\mathbf{R}\begin{pmatrix} t_x \\ t_y 1 \end{pmatrix} = -d_\odot^2\begin{pmatrix} t_{x\odot} \\ t_{y\odot} \\ 1 \end{pmatrix}^\mathsf{T}\begin{pmatrix} t_x \\ t_y \\ 1 \end{pmatrix} = -d_\odot^2(1 + \mathbf{t}_\odot^\mathsf{T}\mathbf{t}) \tag{1.44}$$

$$\text{so that} \qquad b = \frac{\mathbf{r}_{\mathrm{SC}}^\mathsf{T}\mathbf{v}(t_x, t_y)}{\|\mathbf{v}(t_x, t_y)\|^2} = -\frac{1 + \mathbf{t}_\odot^\mathsf{T}\mathbf{t}}{1 + t^2},$$

$$\text{and} \qquad c = \frac{r_{\mathrm{SC}}^2 - r_{\mathrm{srf}}^2}{\|\mathbf{v}(t_x, t_y)\|^2} = (1 - \left(\frac{r_{\mathrm{srf}}}{r_{\mathrm{SC}}}\right)^2)\frac{1 + t_\odot^2}{1 + t^2}.$$

Here, $r_{\mathrm{SC}}^2 > r_{\mathrm{srf}}^2$ because the spacecraft is outside of the Sun and therefore we always have $c > 0$, $b < 0$ and $\alpha_{\mathrm{srf}} > 0$. The two signs in the solution (1.42) denote the two possible intersections of the ray with the solar surface sphere. The lower sign (with the smaller value α_{srf}) gives the visible intersection on the front side, the upper sign the intersection on the back side of the Sun. If $b^2 < c$, the pixel lies outside the solar disk.

Stereoscopic case: Intersection of two rays

In the previous sections, the parameters where considered for a single camera, or spacecraft. Now two observers, or cameras, are considered. The corresponding variables are marked by subscripts A and B, so that he spacecraft positions are $\mathbf{r}_{\mathrm{SC},A}$ and

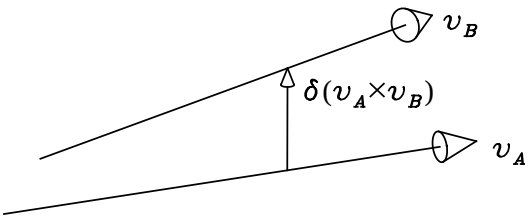

Figure 1.9: Illustration of two beams which do not intersect. The solution (1.47) yields the points on each beam with the least mutual distance $\delta \|\mathbf{v}_A \times \mathbf{v}_B\|$.

$\mathbf{r}_{\mathrm{SC},B}$, as well as the normalized pixel coordinates in images A and B are (t_{Ax}, t_{Ay}) and (t_{Bx}, t_{By}), respectively. Therefore from (1.33), the 3D intersection of the of two rays must satisfy

$$\mathbf{r}_{\mathrm{isect}} = \mathbf{r}_{\mathrm{SC},A} + \alpha_A \mathbf{v}_A(t_{Ax}, t_{Ay}) = \mathbf{r}_{\mathrm{SC},B} + \alpha_B \mathbf{v}_B(t_{Bx}, t_{By}), \tag{1.45}$$

and the distance parameters α_A and α_B of the intersection need to be found. From now on, the pixel arguments (t_{Ax}, t_{Ay}) and (t_{Bx}, t_{By}) of the view directions $\mathbf{v}_A$ and $\mathbf{v}_B$, respectively, will be omitted to have a more concise notation.

Substracting the two right hand sides of 1.45 gives

$$\mathbf{r}_{\mathrm{SC},A} - \mathbf{r}_{\mathrm{SC},B} = \mathbf{d}_{\mathrm{BAS}} = (\mathbf{v}_B, -\mathbf{v}_A) \begin{pmatrix} \alpha_B \\ \alpha_A \end{pmatrix} = \mathbf{V} \begin{pmatrix} \alpha_B \\ \alpha_A \end{pmatrix}. \tag{1.46}$$

The distance vector $\mathbf{r}_{\mathrm{SC},A} - \mathbf{r}_{\mathrm{SC},B}$ is called the stereo base $\mathbf{d}_{\mathrm{BAS}}$ and $\mathbf{V}$ is a 3×2 matrix with columns $\mathbf{v}_B$ and $-\mathbf{v}_A$.

The system (1.46) is overdetermined, so that it only has a solution if the pixel coordinates (t_{Ax}, t_{Ay}) and (t_{Bx}, t_{By}) are chosen such that the two view rays properly intersect. This is equivalent to placing them on a corresponding pair of epipolar lines in each image, which will be shown later.

If the two view rays do not intersect, the minimum square error solution can be obtained using the pseudoinverse of $\mathbf{V}$:

$$\begin{pmatrix} \alpha_B \\ \alpha_A \end{pmatrix} = (\mathbf{V}^\mathsf{T}\mathbf{V})^{-1}\mathbf{V}^\mathsf{T}\mathbf{d}_{\mathrm{BAS}} \tag{1.47}$$

The two view rays $\mathbf{r}_{\mathrm{SC},A} + \alpha_A \mathbf{v}_A$ and $\mathbf{r}_{\mathrm{SC},B} + \alpha_B \mathbf{v}_B$ in this case may not be intersecting, but do have the smallest possible distance. We can calculate the distance between the two solutions and decide whether it is small enough to be acceptable (see Fig. 1.9).

1.2.2 Epipolar Geometry

The stereoscopic analysis performed in this work is based on epipolar geometry. Therefore it is key to give a detailed introduction on the epipolar geometry approach to mathematically explain the basic concepts of epipolar geometry described at the beginning of this chapter.

A more systematic approach to solving the stereo problem is by transforming the problem to an orthogonal system adapted to the particular viewing geometry of the problem, defined solely by the position of the two spacecraft and an arbitrary

object or point at $\mathbf{r}$. Different $\mathbf{r}$ may give different epipolar planes, each forming a new orthogonal system. Among these, the plane through the solar center will serve as a base plane and is therefore labeled as 0. The orthogonal stereo system is defined by

$$\hat{\mathbf{e}}_{\mathrm{BAS}} = \frac{\mathbf{r}_{\mathrm{SC},A} - \mathbf{r}_{\mathrm{SC},B}}{d_{\mathrm{BAS}}}, \quad d_{\mathrm{BAS}} = \|\mathbf{r}_{\mathrm{SC},A} - \mathbf{r}_{\mathrm{SC},B}\| \quad \text{(stereo base)}, \tag{1.48}$$

$$\hat{\mathbf{e}}_{\mathrm{POL}}(0) = \frac{\mathbf{r}_{\mathrm{SC},B} \times \mathbf{r}_{\mathrm{SC},A}}{d^2_{\mathrm{POL}}}, \quad d^2_{\mathrm{POL}} = \|\mathbf{r}_{\mathrm{SC},B} \times \mathbf{r}_{\mathrm{SC},A}\| \quad \text{(mission plane normal)}, \tag{1.49}$$

$$\hat{\mathbf{e}}_{\mathrm{RAD}}(0) = \hat{\mathbf{e}}_{\mathrm{BAS}} \times \hat{\mathbf{e}}_{\mathrm{POL}}(0) \quad \text{(vector from origin to stereo base)}. \tag{1.50}$$

The mission plane is the plane containing both spacecraft and $\mathbf{r}$. The meaning of $\hat{\mathbf{e}}_{\mathrm{BAS}}$ and $\hat{\mathbf{e}}_{\mathrm{POL}}(0)$ is obvious, and $\hat{\mathbf{e}}_{\mathrm{RAD}}(0)$ is directed from the origin of the system to the point $\mathbf{r}_{AB}$ along the stereo base line closest to the origin (see Fig. 1.10).

The distance of $\mathbf{r}_{AB}$ to the system origin can be found with

$$\begin{aligned} \|\mathbf{r}_{\mathrm{AB}}\| = \hat{\mathbf{e}}_{\mathrm{RAD}}(0)^{\mathsf{T}}\mathbf{r}_{\mathrm{SC},A} &= \frac{\mathbf{r}^{\mathsf{T}}_{\mathrm{SC},A}(\mathbf{r}_{\mathrm{SC},A} - \mathbf{r}_{\mathrm{SC},B}) \times \hat{\mathbf{e}}_{\mathrm{POL}}(0)}{d_{\mathrm{BAS}}} \\ &= \frac{(\mathbf{r}_{\mathrm{SC},A} \times (\mathbf{r}_{\mathrm{SC},A} - \mathbf{r}_{\mathrm{SC},B}))^{\mathsf{T}}\hat{\mathbf{e}}_{\mathrm{POL}}(0)}{d_{\mathrm{BAS}}} = \frac{d^2_{\mathrm{POL}}}{d_{\mathrm{BAS}}}. \end{aligned} \tag{1.51}$$

The same result is obtained for $\hat{\mathbf{e}}_{\mathrm{RAD}}(0)^{\mathsf{T}}\mathbf{r}_{\mathrm{SC},B}$.

The other epipolar planes in the same system do not include the solar center. Instead, we define an origin on such a plane in the point on the plane which is closest to the Sun center. These planes will be labeled by their distance ζ from the solar center. For one stereo system, all the epipolar planes contain the stereo base

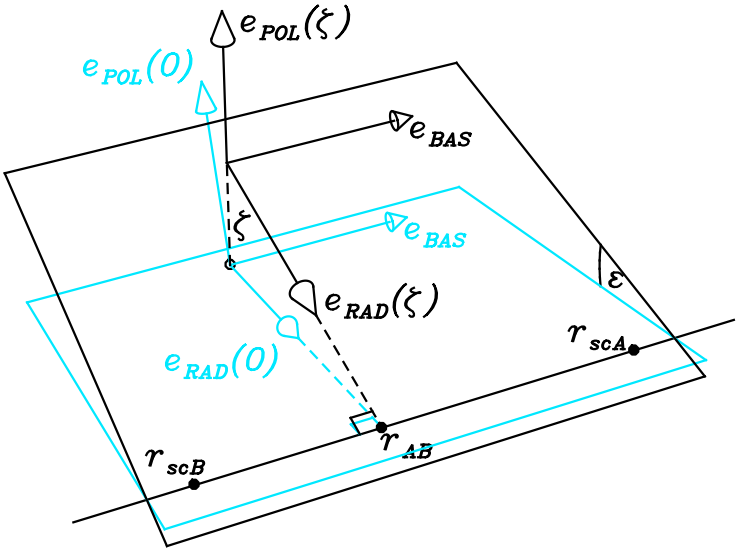

Figure 1.10: Two orthogonal epipolar coordinate systems for two observing spacecraft at $\mathbf{r}_{\mathrm{SC},A}$. In blue, the epipolar plane for $\zeta = 0$ with the solar center as the origin. In black an inclined epipolar plane with planar coordinate system that has its origin at the distance ζ from the Sun center is displayed.

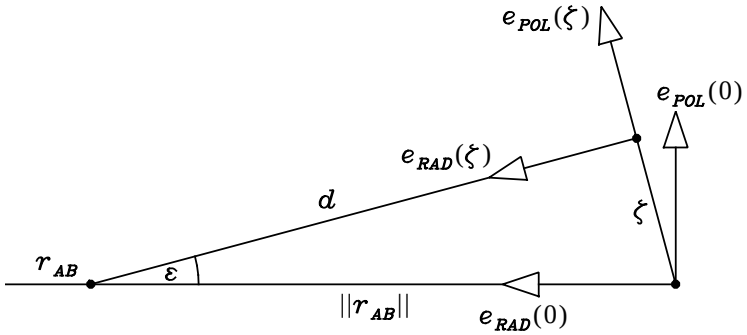

Figure 1.11: Illustration of the triangle in (1.54) in the plane orthogonal to the epipolar plane to find the relation between ζ and ε. The epipolar plane here corresponds to the line along $\hat{\mathbf{e}}_{\mathrm{RAD}}(\zeta)$. The distance from $\mathbf{r}_{AB}$ to the origin of the epipolar plane ζ is $d = ||\mathbf{r}_{AB}|| \cos\varepsilon$.

line (1.48) and therefore have the same $\hat{\mathbf{e}}_{\mathrm{BAS}}$. The plane normal $\hat{\mathbf{e}}_{\mathrm{POL}}(\zeta)$ and the third orthogonal $\hat{\mathbf{e}}_{\mathrm{RAD}}(\zeta)$ are rotated with respect to (1.49) and (1.50) by an angle ε (see Fig. 1.10).

The sign of ζ is defined as the sign of $\hat{\mathbf{e}}_{\mathrm{POL}}(\zeta)^{\mathsf{T}}\hat{\mathbf{e}}_{\mathrm{RAD}}(0)$. Any epipolar plane ζ has an inclination ε with respect to the plane $\zeta = 0$. Any point on the epipolar plane is given by the parameters α, β and

$$\mathbf{r} = \zeta\hat{\mathbf{e}}_{\mathrm{POL}}(\zeta) + \alpha\hat{\mathbf{e}}_{\mathrm{RAD}}(\zeta) + \beta\hat{\mathbf{e}}_{\mathrm{BAS}}(0),$$

where

$$\begin{aligned}
&\zeta\hat{\mathbf{e}}_{\mathrm{POL}}(\zeta) \qquad \text{is the origin on the plane} \\
&\hat{\mathbf{e}}_{\mathrm{POL}}(\zeta) = \hat{\mathbf{e}}_{\mathrm{POL}}(0)\cos\varepsilon + \hat{\mathbf{e}}_{\mathrm{RAD}}(0)\sin\varepsilon && (1.52)\\
&\hat{\mathbf{e}}_{\mathrm{RAD}}(\zeta) = \hat{\mathbf{e}}_{\mathrm{RAD}}(0)\cos\varepsilon - \hat{\mathbf{e}}_{\mathrm{POL}}(0)\sin\varepsilon = \hat{\mathbf{e}}_{\mathrm{BAS}} \times \hat{\mathbf{e}}_{\mathrm{POL}}(\zeta) && (1.53)
\end{aligned}$$

The points $\zeta\hat{\mathbf{e}}_{\mathrm{POL}}(\zeta)$, $\mathbf{r}_{AB}$ on the stereo base line and the Sun center form a right-angled triangle (see Fig. 1.11) so that

$$\zeta\hat{\mathbf{e}}_{\mathrm{POL}}(\zeta) + d\hat{\mathbf{e}}_{\mathrm{RAD}}(\zeta) = ||\mathbf{r}_{\mathrm{AB}}||\hat{\mathbf{e}}_{\mathrm{RAD}}(0). \tag{1.54}$$

Here, d is the distance of the new origin $\zeta\hat{\mathbf{e}}_{\mathrm{POL}}(\zeta)$ to the stereo base line located at $||\mathbf{r}_{\mathrm{AB}}||\hat{\mathbf{e}}_{\mathrm{RAD}}(0)$. Multiplying Eq. 1.54 with $\hat{\mathbf{e}}_{\mathrm{POL}}(\zeta)$ gives a relation between ζ and ε for each epipolar plane.

$$\zeta = ||\mathbf{r}_{\mathrm{AB}}||\hat{\mathbf{e}}_{\mathrm{POL}}(\zeta)^{\mathsf{T}}\hat{\mathbf{e}}_{\mathrm{RAD}}(0) = ||\mathbf{r}_{\mathrm{AB}}|| \sin \tag{1.55}$$

with $||\mathbf{r}_{\mathrm{AB}}||$ from (1.51), which can also be seen in Fig. 1.11.

Spacecraft Coordinates in Epipolar Geometry

Since the base vectors (1.48), (1.52) and (1.53) are orthogonal, it is straightforward to decompose the spacecraft coordinates with respect to them, recalling that $||\mathbf{r}_{\mathrm{AB}}||$ is the distance to the stereo base line (1.51).

$$\mathbf{r}_{\mathrm{SC},A} = b_A\hat{\mathbf{e}}_{\mathrm{BAS}} + ||\mathbf{r}_{\mathrm{AB}}||\hat{\mathbf{e}}_{\mathrm{RAD}}(0), \qquad \mathbf{r}_{\mathrm{SC},B} = b_B\hat{\mathbf{e}}_{\mathrm{BAS}} + ||\mathbf{r}_{\mathrm{AB}}||\hat{\mathbf{e}}_{\mathrm{RAD}}(0). \tag{1.56}$$

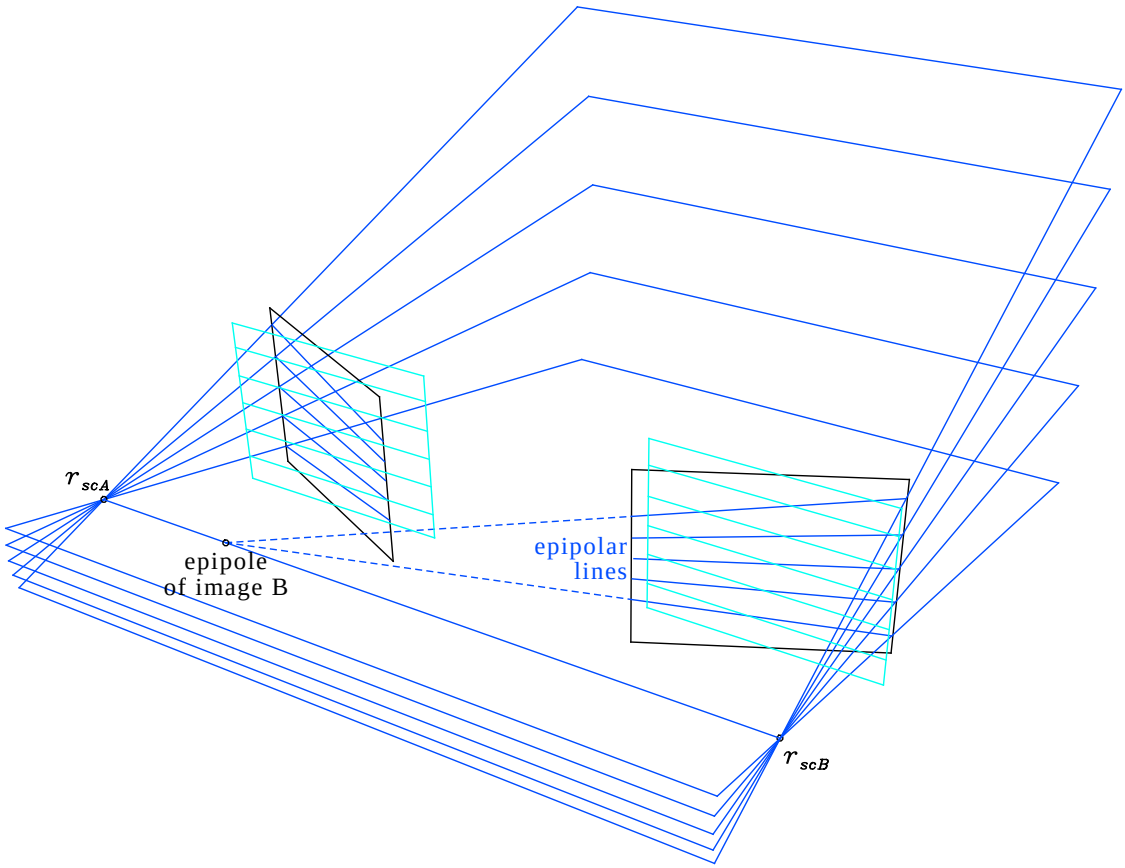

Figure 1.12: Illustration of rectification. $\mathbf{r_{scA}}$ and $\mathbf{r_{scB}}$ are the spacecraft positions, the black frames represent their respective retinal planes. After rectification, the frames are rotated (light blue) so that they have the same extrinsic matrix $\mathbf{R}'$.

The coefficients b_A and b_B can be calculated inserting the base vectors:

$$\hat{\mathbf{e}}_{\mathrm{BAS}}^{\mathsf{T}}\mathbf{r}_{\mathrm{SC},A} = \frac{r_{\mathrm{SC},A}^2 - \mathbf{r}_{\mathrm{SC},A}^{\mathsf{T}}\mathbf{r}_{\mathrm{SC},A}}{d_{\mathrm{BAS}}} = b_A, \quad \hat{\mathbf{e}}_{\mathrm{BAS}}^{\mathsf{T}}\mathbf{r}_{\mathrm{SC},B} = \frac{\mathbf{r}_{\mathrm{SC},A}^{\mathsf{T}}\mathbf{r}_{\mathrm{SC},A} - r_{\mathrm{SC},B}^2}{d_{\mathrm{BAS}}} = b_B \tag{1.57}$$

$$\text{with } b_A - b_B = \frac{\|\mathbf{r}_{\mathrm{SC},A} - \mathbf{r}_{\mathrm{SC},B}\|^2}{d_{\mathrm{BAS}}} = d_{\mathrm{BAS}}, \quad b_A + b_B = \frac{\mathbf{r}_{\mathrm{SC},A}^2 - \mathbf{r}_{\mathrm{SC},B}^2}{d_{\mathrm{BAS}}}.$$

Rectification

Rectification is a very useful tool for stereoscopic depth analysis and is key for the stereoscopic method developed in this work. A brief description will be given in this section, but more details on image rectification can be found in Fusiello et al. (2000). The procedure for rectifying is to calculate the view ray for a pixel (t_x, t_y) in the original extrinsic matrix frame $\mathbf{R}$ according to Eq. 1.32 and then to reproject the view ray back to a new retinal image plane but in a modified extrinsic frame $\mathbf{R}'$ with a rotated focal (and retinal) plane. $\mathbf{R}'$ is the rectified extrinsic frame. It can be seen in Fig. 1.12 that the goal of rectification is to move the epipole of one feature in the images to infinity so that the epipolar lines become parallel. This is very useful in stereoscopic depth reconstruction because corresponding pixels must lie on the same epipolar plane. Rectification ensures that corresponding features lie

on the same horizontal line between rectified images, so that the depth analysis is reduced to a series of independent 1D problems of finding the correspondence in the x direction along a pair of horizontal rows with the same y coordinate in both images.

To achieve rectification, the new extrinsic camera frame, which is common for the images from both spacecraft, must have its x-axis parallel to the stereo base (Eq. 1.48), the same plane normal in z and the y axis completes an orthogonal system. In other words, the x, y and z axes correspond to the orthogonal base for one of the epipolar planes ζ. The base plane $\zeta = 0$ will be used here, but the base for any other epipolar plane in the system is likewise possible. For the rectified extrinsic frame we set

$$\hat{\mathbf{e}}'_x = \hat{\mathbf{e}}_{\mathrm{BAS}}, \quad \hat{\mathbf{e}}'_y = \hat{\mathbf{e}}_{\mathrm{POL}}(0), \quad \hat{\mathbf{e}}'_z = -\hat{\mathbf{e}}_{\mathrm{RAD}}(0), \quad \mathbf{R}' = [\hat{\mathbf{e}}'_x, \hat{\mathbf{e}}'_y, \hat{\mathbf{e}}'_z]. \tag{1.58}$$

The image ray should not change in 3D coordinates, and therefore the transformed image coordinates can be calculated using (1.32), for example for image A:

$$\mathbf{v}_A(t_x, t_y) \propto \mathbf{R} \begin{pmatrix} t_x \\ t_y \\ 1 \end{pmatrix} \propto \mathbf{R}' \begin{pmatrix} t'_x \\ t'_y \\ 1 \end{pmatrix} \quad \text{or} \quad \begin{pmatrix} t'_x \\ t'_y \\ 1 \end{pmatrix} \propto \mathbf{R}'^{\mathsf{T}} \mathbf{R}_A \begin{pmatrix} t_x \\ t_y \\ 1 \end{pmatrix},$$

Similarly for image B. $\mathbf{R}_A$ and $\mathbf{R}_B$ are the extrinsic camera matrices for image A and B, respectively, and $\mathbf{R}'$ is the same for the rectified camera frame.

The proportionality term $\propto$ compensates for the different distances $d_{A\odot} \neq d_{B\odot}$ of the two spacecraft. The rectified pixel coordinates t'_x and t'_y then have to be interpreted as the tangent of the view angle with the new rectified axis direction $-\hat{\mathbf{e}}_{\mathrm{RAD}}(0)$ as seen from the cameras at the positions of the corresponding spacecraft. The rectification is performed by the following linear transformation. For image A:

$$\begin{pmatrix} t''_{Ax} \\ t''_{Ay} \\ t''_{Az} \end{pmatrix} = \mathbf{R}'^{\mathsf{T}} \mathbf{R}_A \begin{pmatrix} t_{Ax} \\ t_{Ay} \\ 1 \end{pmatrix}, \qquad \begin{pmatrix} t'_{Ax} \\ t'_{Ay} \\ 1 \end{pmatrix} = \begin{pmatrix} t''_{Ax}/t''_{Az} \\ t''_{Ay}/t''_{Az} \\ 1 \end{pmatrix}, \tag{1.59}$$

and equivalently for image B. The rectification requires retinal plane rotations, so it is expected that rectifying the images causes some distortion.

Figure 1.13 shows an extreme case to explain the effect of the rectification. The two spacecraft are separated by an angle of $175°$. The top panels show the image in normalized, not rectified, pixel coordinates, the solar disk in red, epipolar lines in dark blue and a regular pixel grid indicated by the black crosses. The extension of the epipolar lines towards their intersection yields the epipole of the respective image, shown in light blue. The bottom panels show the same images after they were rectified. The epipolar lines are now horizontal, but both the solar disk and the original pixel grid are distorted, as well as the tangent values of the coordinates, which are now larger in magnitude because the rectified optical axes point far off the solar center.

1.2.3 Previous Stereoscopic Studies of the Sun

Stereoscopic techniques have been used to study solar features for many years, focused mainly on discrete coronal features: loops, filaments and identifiable features

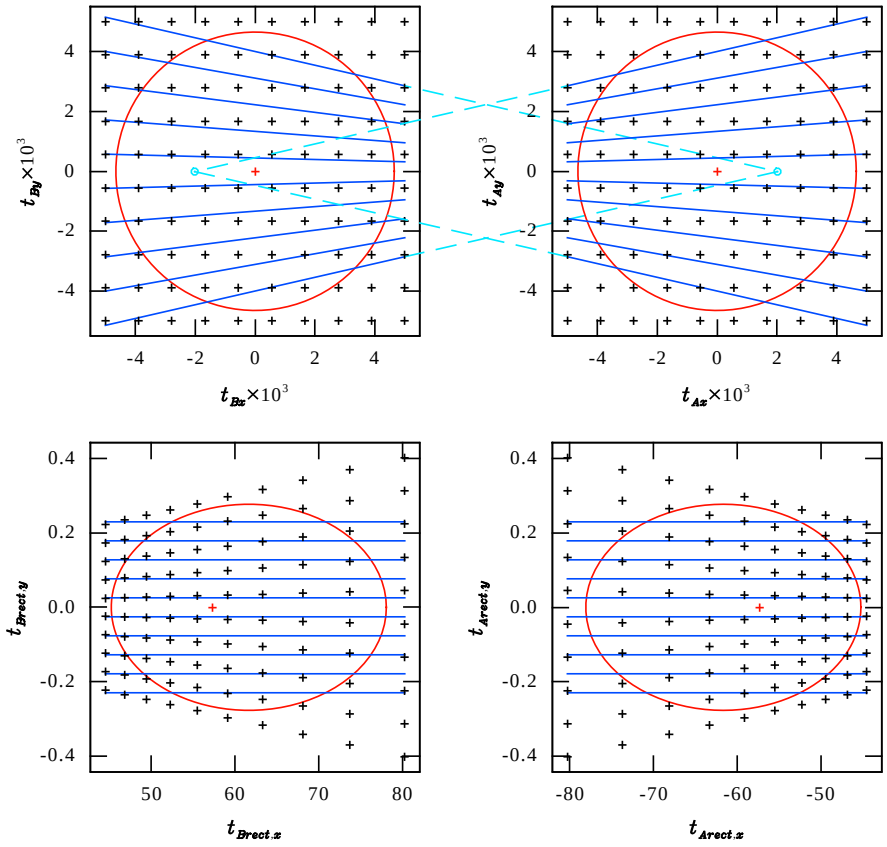

Figure 1.13: The effect of rectification of the original image pair (top row) to rectified images (bottom pair) for two spacecraft at $\|\mathbf{r}_{\mathrm{SC}}\| = 200R_{\odot}$ and longitudinal separation of $175°$. For further details see text.

of CMEs. The first solar stereoscopic attempts were applied to ground-based data at wavelengths in the optical EUV and radio ranges. They used the solar rotation to obtain a pair of independent images assuming that the object did not change in between. Koutchmy and Molodenskii (1992) used two white light pictures during the solar eclipse of 1991, observed 3 hours apart, to make a stereoscopic triangulation of ray-like coronal structures. Another application used high resolution radio images to synthesize altitude measurements at different frequencies and construct a 3D model of the magnetic field or the plasma density (Aschwanden et al., 1992; Aschwanden et al., 1995).

The first space-based stereoscopic studies also used the solar rotation, due to the fact that all the space missions dedicated to study the Sun at the time (i.e. SMM, Yohkoh, SOHO) had near Earth orbits. However, their imaging capabilities were better in comparison to earth-bound observatories. With this rotation-based stereoscopy, images from the mission *Skylab* were used to study coronal loops (Berton & Sakurai, 1985); images from Yohkoh were used to produce stereoscopic images of the soft X-ray corona (Hurlburt et al., 1994) and SOHO images to reconstruct the 3D geometry of solar prominences (Foullon, 2003) and EUV loops (Aschwanden, 2011).

Reconstruction of non stationary objects requires simultaneous observations from at least two vantage points. Such observations, necessary for any stereoscopic analysis of solar features, require to be coordinated. Early combined observations of the Earth-bound Nançay radioheliograph and the probe *Mars-3* measured solar type III bursts (Caroubalos & Steinberg, 1974). Hard X-ray bursts of solar flares were measured with multi-spacecraft observations by Kane (1981)

The first space mission dedicated to provide data for stereoscopic analysis of the Sun was the Solar TErrestrial RElations Observatory (STEREO), which consisted of two spacecraft. Most of the stereoscopic studies of the corona use data from STEREO (Inhester, 2006; Aschwanden, 2011) sometimes combined with images from SOHO or one observatory on Earth observing in the same spectral range. Both spacecraft from STEREO orbit the Sun at 1 AU, but independent from each other. They have Extreme Ultraviolet (EUV) imagers and coronagraphs to observe the Sun and the corona. These instruments do not allow for photospheric observations because the EUV corona lies well above the photosphere and in coronagraphs the solar disk is entirely occulted. Nevertheless, the Polarimetric Helioseismic Imager (SO/PHI, see Solanki et al., 2020) on board of the Solar Orbiter (SO/PHI), launched in 2020 (see Müller et al., 2020), can be used to observe the photosphere in white light and high resolution. This opens the possibility to perform stereoscopic studies of photospheric features, sunspots being the most obvious; if its observations are combined with observations from another spacecraft orbiting the Sun or with an Earth bound telescope in the same spectral range.

Even though no attempts to study sunspots using stereoscopy have yet been made, active regions (AR) studies using stereoscopy have been made. The 3D density and temperature distributions of active regions can be obtained with radio-stereoscopy. But stereoscopically triangulating the altitude $h(\lambda)$ of a radio source at a given wavelength requires a parametrization of these models (Aschwanden, 2011). A review on the 3D reconstruction, geometry and distributions of physical parameters in ARs is given in Aschwanden and Wülser (2011).

As it has been mentioned before, stereoscopic techniques to reconstruct surface features like sunspots require to identify clear features, edges or marks in a pair of

images. Photospheric images, due to their lower contrast, lack these clear features. In order to perform a stereoscopic analysis of the altitude variations on the solar surface a new different approach based on statistical correlations is necessary. The motivation of this thesis is to perform a stereoscopic analysis of the Wilson depression of sunspots of active regions. This is the most relevant height variation of the solar surface at an optical depth of $\tau = 1$.

Quantifying the height variations of the Wilson depression is relevant to better understand the magnetic and geometric structure of sunspots. In the following chapters of this work a new compound stereoscopic method, developed to measure variations in the photospheric altitude, will be presented and discussed. Chapter 2 consists on a general description of the method, and the basic concepts, definitions and assumptions are presented. In Chapter 3 the method is applied to images obtained to synthetic MHD data. Some practical reformulations of the method to be applied to these data, as well as a brief overview on the data is presented. Then the method's performance with the test data is presented and discussed. In Chapter 4 the method is applied to real data. The data, as well as the instruments with which it was obtained are described. Much more practical reformulations were needed when using real data, and they are described in this chapter. Some preliminary results and discussion of the performance of the method with real images are also included. Chapter 5 presents a discussion on the results obtained, the advantages and limitations of the developed method. Lastly, we present a chapter with an outlook for the possible results to be obtained and the possible scientific goals that could be achieved when applying the method presented here to further combined observations.

Chapter 2

A Method for Sunspot Stereoscopy

This chapter describes of the correlation-based method developed to perform stereoscopic analysis of the height variations of the solar surface in sunspots to estimate their Wilson depression. The results of applying this method to synthetic test data and real observations from two different spacecraft are presented in Chapters 3 and 4, respectively.

The basics of epipolar geometry were given in Section 1.2.2. With this basis some additional concepts can be introduced to describe the method and the procedure to perform a stereoscopic analysis of photospheric observations from two spacecraft. Figure 2.1 illustrates the epipolar configuration of two spacecraft observing a region on the Sun, and the corresponding epipolar profiles, which are the intersections of their respective epipolar plane with the solar sphere, which we assume to be a thin layer into which all the radiation is condensed (see Eq. 1.7). Equation 1.7 can be considered as the definition of the height variation that we want to obtain.

Most likely, in a scene as the one described above, the epipolar lines of each image will be oblique to heliospheric latitude circles and, mapped into an image as epipolar lines, oblique to the horizontal image axis. The idea of rectification is to reproject both images in order to move the epipole of each image to infinity so that the corresponding epipolar lines become horizontal and the calculations along the epipolar profiles are performed only in one direction.

If the rectification is performed correctly, corresponding features in both images should appear along the same epipolar profile, however their projected position along the epipolar profile is different for the two images. Given a feature $\mathbf{r}$ present in both rectified images with coordinates $(t'_{x,A}, t'_{y,A})$ in image A, and $(t'_{x,B}, t'_{y,B})$ in image B, the t'_y coordinate is the same one in both rectified images. The difference in the horizontal position can be measured as $d = t'_{x,A} - t'_{x,B}$, and its relation with the distance of P to the cameras optical centers is given by (Faugeras, 1993):

$$d = t'_{x,A} - t'_{x,B} = r_{AB}\frac{f}{z},$$

where z is the distance from $\mathbf{r}$ to r_{AB}, and f_c the distance from r_{AB} to the image plane. This difference in projection of a feature in different planes is called disparity and is a fundamental quantity in stereoscopic analysis, since the disparity of corresponding features is proportional to the distance of a feature to the image planes (Faugeras, 1993). Therefore, if the disparity between corresponding features can be found, the distance of the feature can be estimated. If the disparity is 0, then

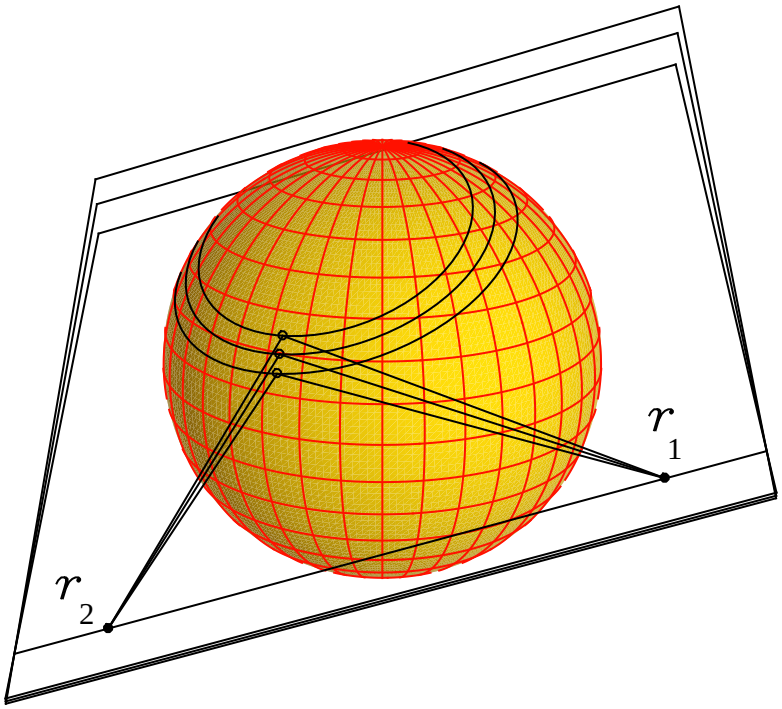

Figure 2.1: Illustration of three nearby epipolar planes for spacecraft at positions $\mathbf{r}_1$ and $\mathbf{r}_2$ and the epipolar plane intersections with the solar surface. Each of these intersections constitutes an epipolar surface profile on which our stereoscopic analysis is independently applied.

the observed feature is at infinity or at a distance larger than what the resolution of the images allow to distinguish.

The relation of disparity and depth above assumes that the camera geometry is such that the two retinal planes are the same. This applies for the particular case in which the two cameras are parallel (as displayed in Fig. 2.2), or if the images have been rectified, given that the aim of rectification is to reproject the images so that they are projected as if the cameras were parallel. If the cameras have arbitrary positions the relation between pixel coordinates of corresponding points is not as simple. However, the simple approach is intuitive and explains well the geometric principle of stereoscopy (for more details on disparity for a general camera case see Faugeras, 1993).

If discrete features cannot be discerned in the images an alternative is to determine the disparity by correlating the image intensities along the two epipolar profiles. This is the approach used in this work as well. It consists in shifting and correlating windows of data around a reference point $\mathbf{r}$ to estimate the disparity of $\mathbf{r}$ from the maximal correlation and subsequently convert the optimal shift into a height. In this approach it is assumed that the disparity is constant within the whole analyzed window, so that if the disparity gradient is high the method might not be precise. A drawback of this approach is that if the correlation function does not have a pronounced maximum, then the disparity cannot be determined very accurately (Faugeras, 1993).

The correlation method presented here is complemented with an optimization method. Optimization methods aim to find the best solution to a problem from all

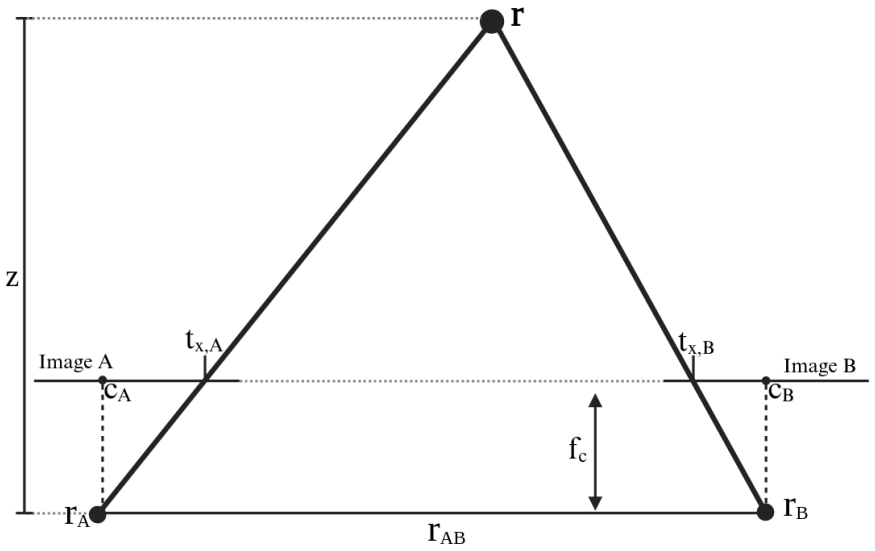

Figure 2.2: Parallel camera scheme. r_A and r_B represent the camera positions; r_{AB} the stereo base line connecting both cameras; c_A and c_B are the positions of the optical centers in the retinal plane, and $t_{x,A}$ and $t_{x,B}$ the horizontal coordinates of $\mathbf{r}$ on the retinal plane. A relation between depth and disparity is $d \propto f_c/z$, where f_c is the distance from R_{AB} to the retinal plane, and z the distance from $\mathbf{r}$ to r_{AB}, equivalent to the depth.

possible solutions. The optimization method presented in this work aims to find a height vector to reconstruct the image intensities of both cameras in a way such that the difference to the observed intensities at each point is as small as possible. A general description of both methods will be presented in the following sections of this chapter.

2.1 The Correlation Method

The stereoscopic analysis of a given feature in the solar surface seen from two different view points requires a precise geometric calibration of the two observing cameras, to set up the intrinsic and extrinsic matrices (see Chapter 1). In the method described here the stereoscopic analysis consists in performing the calculations to estimate the height for points along an epipolar profile. Epipolar profiles are displayed as image rows in the rectified images (Faugeras, 1993). Therefore the obtained height estimates from this analysis represent the height variation along the epipolar surface profiles (Fig. 2.1). In order to retrieve information from 2D Surface areas, successive adjacent epipolar profiles must be processed.

The conditions for applying stereoscopy depend strongly on the difference between the viewing angles from the two spacecraft at the points on an epipolar profile and their angle difference to the local surface normal. The viewing angle γ from one of the two spacecraft is defined as the angle between the projection of the surface normal at a given point onto the epipolar plane and the respective line of sight from that spacecraft. The viewing angles vary along the surface profile, roughly by 1 degree per each degree in longitude on the solar surface.

To determine the height variation along a profile it is necessary to first identify

the point of interest $\mathbf{r}$ on the solar surface in both images. As it was mentioned in the paragraph above, the correlation approach correlates the rectified image intensities around $\mathbf{r}$. Given the nature of the observations used in this work, it is not straightforward to simply use the intensities in the image rows to correlate them. The surface brightness observed in continuum observations of the solar photosphere are, after rectification, converted into virtual intensity profiles (VIPs, as they will be referred to further in this work) along an epipolar profile. To determine disparity and depth, the VIPs are shifted, windowed and correlated. The aim of the correlation is to find the shift for which the correlation is maximized, so that this shift can be converted into a height variation estimate around the standard solar surface.

In this chapter our approach is described in detail using the results of Chapter 1, specialized for stereoscopy on a spherical surface like that of the Sun.

The first step to estimate the height variations of a point $\mathbf{r}$ of interest on the solar surface as seen by two spacecraft, is to locate its pixel coordinates $(p_{x,A}, p_{y,A})$ in one of the original, not rectified images (in this case from spacecraft A). Then the pixel coordinates $(p_{x,A}, p_{y,A})$ of this point must be converted into normalized coordinates $(t_{x,A}, t_{y,A})$ using Eq. 1.25, and then the view ray vector $\mathbf{v}_A$ to that point from $\mathbf{r}_{\mathrm{SC},A}$ is found using Eq. 1.41 and Eq. 1.42, as well as its intersection at $\mathbf{r}$ with the solar standard sphere with $\|\mathbf{r}\| = R_\odot$ as the standard solar radius.

The three points $\mathbf{r}_{\mathrm{SC},A}$, $\mathbf{r}_{\mathrm{SC},B}$ and $\mathbf{r}$ now uniquely determine the epipolar plane for the epipolar profile to analyze, containing the point of interest. The parameters ζ and ε of this plane can be obtained from Section 1.2.2.

The epipolar base vectors $\hat{\mathbf{e}}_{\mathrm{POL}}(\zeta)$ and $\hat{\mathbf{e}}_{\mathrm{RAD}}(\zeta)$ must also be calculated. Here $\hat{\mathbf{e}}_{\mathrm{BAS}}(\zeta) = \hat{\mathbf{e}}_{\mathrm{BAS}}(0)$, which was obtained when the images were rectified; and $\hat{\mathbf{e}}_{\mathrm{RAD}}(\zeta)$, $\hat{\mathbf{e}}_{\mathrm{POL}}(\zeta)$ are rotated from the orthonormal base ($\zeta = 0$) by an elevation angle ε for any given ζ (see Eqs. 1.52 and 1.53).

The following sections then describe in detail the steps needed to compute the height variations $\mathbf{r}$ around the solar surface: how the grid is mapped onto the image, how the VIPs are produced, how the viewing angles γ are calculated along an epipolar profile, and how the VIPs are shifted to be correlated. Once these procedures have been introduced, a description of how the correlation coefficient of the two VIPs is computed at any given shift is introduced to find the disparity of $\mathbf{r}$. Finally the final computations to convert the disparity into a height variation dh are given.

It is important to remark that the following procedure considers images from observations of the solar surface from two cameras, or spacecraft, A and B. It is also considered that the images have been rectified, and therefore all the camera and epipolar parameters of the system, described in Chapter 1, have been determined, so that the correlation has to be performed along 1D profiles for each pair of images.

2.1.1 Mapping the Surface Grid to an Image

Once ζ, ε and the epipolar base have been determined, the next step is to define a grid along the epipolar surface profile on which the VIPs are be discretized. We then map this surface grid onto the images and the observed image intensity in this mapped grid cell is integrated to give the VIP value in this surface cell.

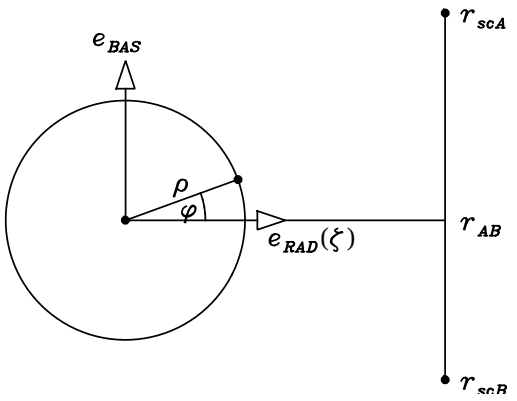

Figure 2.3: View of the epipolar plane defined by $\hat{\mathbf{e}}_{\mathrm{RAD}}(\zeta)$ and $\hat{\mathbf{e}}_{\mathrm{BAS}}$, which has the 3D vector $\zeta\hat{\mathbf{e}}_{\mathrm{POL}}(\zeta)$ at the origin, normal to the plane of the figure. The longitudinal coordinate φ is illustrated in this figure. The circle represents the intersection of the epipolar plane with the solar surface and has a radius $\rho = \sqrt{R_\odot^2 - \zeta^2}$.

For an arbitrary point $\mathbf{r}$ on an epipolar plane and the solar surface

$$\begin{gathered}\mathbf{r} = \zeta\hat{\mathbf{e}}_{\mathrm{POL}}(\zeta) + \rho(\hat{\mathbf{e}}_{\mathrm{RAD}}(\zeta)\cos\varphi + \hat{\mathbf{e}}_{\mathrm{BAS}}\sin\varphi),\\ R_\odot = \|\mathbf{r}\|, \quad \rho = \sqrt{R_\odot - \zeta^2}\\ \varphi = -\arctan\Big[\frac{\hat{\mathbf{e}}_{\mathrm{RAD}}^{\mathsf{T}}(\zeta)(\mathbf{r} - \zeta\hat{\mathbf{e}}_{\mathrm{POL}}(\zeta))}{\hat{\mathbf{e}}_{\mathrm{BAS}}^{\mathsf{T}}(\mathbf{r} - \zeta\hat{\mathbf{e}}_{\mathrm{POL}}(\zeta))}\Big],\end{gathered}$$

where ρ is the radius of the epipolar latitude circle of $\mathbf{r}$. This circle corresponds to the intersection of the epipolar plane ζ with the solar sphere of radius $R_\odot$ (see Fig. 2.3). If $\zeta > R_\odot$, the epipolar plane does not intersect the solar surface.

The parameter φ is the longitudinal coordinate from $\hat{\mathbf{e}}_{\mathrm{RAD}}$ and is defined such that it counts positively in counterclockwise direction. By discretizing the parameter φ for the ζ-plane, a discrete surface grid that covers the vicinity of $\mathbf{r}$ can be obtained. This grid has its grid centers at

$$\mathbf{r}_i(\varphi_i, \zeta) = \zeta\hat{\mathbf{e}}_{\mathrm{POL}}(\zeta) + \rho(\hat{\mathbf{e}}_{\mathrm{RAD}}(\zeta)\cos\varphi_i + \hat{\mathbf{e}}_{\mathrm{BAS}}\sin\varphi_i), \tag{2.1}$$

with an equidistant spacing $d\varphi$, which is one of the parameters that can be tuned for an optimal result. The distance of the grid points along the solar surface is $d\ell = \rho d\varphi$.

An advantage of mapping the grid onto the rectified images is that the problem becomes simplified in the sense that the corresponding epipolar planes appear as horizontal profiles with the same vertical position in the images. To map the surface grid to the rectified image Eq. 1.38 is used, only that now it is with the extrinsic matrix of the rectified frame, $\mathbf{R}'$ obtained from Eq. 1.58, which is the same for both cameras.

To map the surface grid coordinate φ_i on the epipolar plane ζ, to the rectified

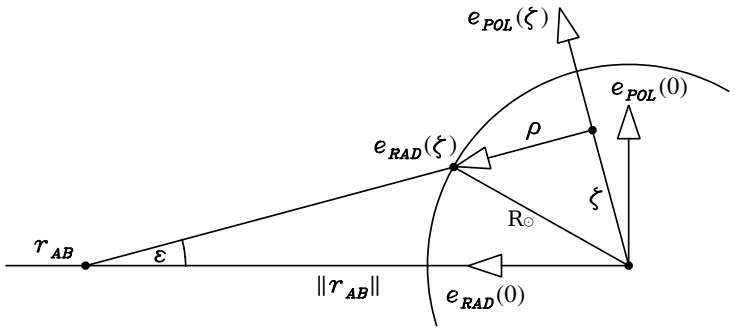

Figure 2.4: View of the plane defined by $\hat{\mathbf{e}}_{\mathrm{RAD}}(\zeta)$ and $\hat{\mathbf{e}}_{\mathrm{POL}}(\zeta)$, which is perpendicular to the epipolar plane, drawn here with the line that goes from $\mathbf{r}_{AB}$ to $\zeta\hat{\mathbf{e}}_{\mathrm{POL}}(\zeta)$. This figure displays the ζ-plane with respect to the 0-plane.

image coordinates, we combine Eqs. 1.38, 2.1 and 1.59:

$$\begin{pmatrix} t'_{x,i} \\ t'_{y,i} \\ 1 \end{pmatrix} \propto [\mathbf{R}'^{\mathsf{T}} \mid -\mathbf{R}'^{\mathsf{T}}\mathbf{r}_{\mathrm{SC}}] \begin{pmatrix} \mathbf{r}_i \\ 1 \end{pmatrix} = \begin{pmatrix} \hat{\mathbf{e}}^{\mathsf{T}}_{\mathrm{BAS}} \\ \hat{\mathbf{e}}^{\mathsf{T}}_{\mathrm{POL}}(0) \\ -\hat{\mathbf{e}}^{\mathsf{T}}_{\mathrm{RAD}}(0) \end{pmatrix} (\mathbf{r}_i - \mathbf{r}_{\mathrm{SC}})$$

$$= \begin{pmatrix} \hat{\mathbf{e}}^{\mathsf{T}}_{\mathrm{BAS}} \\ \hat{\mathbf{e}}^{\mathsf{T}}_{\mathrm{POL}}(0) \\ -\hat{\mathbf{e}}^{\mathsf{T}}_{\mathrm{RAD}}(0) \end{pmatrix} (\zeta\hat{\mathbf{e}}_{\mathrm{POL}}(\zeta) + \rho(\hat{\mathbf{e}}_{\mathrm{RAD}}(\zeta)\cos\varphi_i + \hat{\mathbf{e}}_{\mathrm{BAS}}\sin\varphi_i) - \mathbf{r}_{\mathrm{SC}})$$

$$= \begin{pmatrix} \rho\sin\varphi_i - \hat{\mathbf{e}}^{\mathsf{T}}_{\mathrm{BAS}}\mathbf{r}_{\mathrm{SC}} \\ \zeta\cos\varepsilon - \rho\cos\varphi_i\sin\varepsilon \\ -\zeta\sin\varepsilon - \rho\cos\varphi_i\cos\varepsilon + \hat{\mathbf{e}}^{\mathsf{T}}_{\mathrm{RAD}}(0)\mathbf{r}_{\mathrm{SC}} \end{pmatrix}.$$

From Fig. 2.4 and from Eq. 1.56, $\hat{\mathbf{e}}^{\mathsf{T}}_{\mathrm{BAS}}\mathbf{r}_{\mathrm{SC}} = b$ and $\hat{\mathbf{e}}^{\mathsf{T}}_{\mathrm{RAD}}(0)\mathbf{r}_{\mathrm{SC}} = \|\mathbf{r}_{AB}\| = \zeta/\sin\varepsilon$. Therefore

$$\begin{pmatrix} t'_{x,i} \\ t'_{y,i} \\ 1 \end{pmatrix} \propto \begin{pmatrix} \rho\sin\varphi_i - b \\ \zeta\cos\varepsilon - \rho\cos\varphi_i\sin\varepsilon \\ \zeta(1/\sin\varepsilon - \sin\varepsilon) - \rho\cos\varphi_i\cos\varepsilon \end{pmatrix} = \begin{pmatrix} \rho\sin\varphi_i - b \\ \zeta\cos\varepsilon - \rho\cos\varphi_i\sin\varepsilon \\ \zeta\frac{\cos^2\varepsilon}{\sin\varepsilon} - \rho\cos\varphi_i\cos\varepsilon \end{pmatrix}$$

$$\text{or} \quad t'_{y,i} = \frac{\zeta\cos\varepsilon - \rho\cos\varphi_i\sin\varepsilon}{\zeta\frac{\cos^2\varepsilon}{\sin\varepsilon} - \rho\cos\varphi_i\cos\varepsilon} = \tan\varepsilon \tag{2.2}$$

$$t'_{x,i} = \frac{\rho\sin\varphi_i - b}{\zeta\frac{\cos^2\varepsilon}{\sin\varepsilon} - \rho\cos\varphi_i\cos\varepsilon} = \frac{\rho\sin\varphi_i - b}{\|\mathbf{r}_{AB}\|\cos^2\varepsilon - \rho\cos\varphi_i\cos\varepsilon} \tag{2.3}$$

Here, b can be either b_A or b_B for space craft A or B according to Eq. 1.57, and ρ and ε are both functions of ζ. The fact that $t'_{y,i}$ in Eq. 2.2 is independent of the index i is a result of rectifying the image. The result for $t'_{x,i}$ can be geometrically explained by Fig. 2.4. Given that the distance from $\mathbf{r}_{AB}$ to the origin of the epipolar plane ζ is $\|\mathbf{r}_{AB}\|\cos\varepsilon$ (see Fig. 1.11), the tangents of the view direction angle to the projected rectified optical axis

$$\tan\phi_{A,i} = \frac{\mathbf{e}_{\mathrm{BAS}}\hat{\mathbf{v}}}{\mathbf{e}^{\mathsf{T}}_{\mathrm{RAD}}(\zeta)\hat{\mathbf{v}}} = \frac{\rho\sin\varphi_i - b}{\|\mathbf{r}_{AB}\|\cos\varepsilon - \rho\cos\varphi}, \tag{2.4}$$

for a grid point i. Finally, we project $\tan\phi_{A,i}$ from the epipolar plane ζ onto the epipolar plane $\zeta = 0$ because it contains the optical axis of the rectified camera

matrix. Then Eq. 2.3 is recovered by

$$t'_{x,i} = \frac{\mathbf{e}_{\mathrm{BAS}}\hat{\mathbf{v}}}{\mathbf{e}^{\mathsf{T}}_{\mathrm{RAD}}(0)\hat{\mathbf{v}}} = \frac{\mathbf{e}_{\mathrm{BAS}}\hat{\mathbf{v}}}{\cos(\varepsilon)\mathbf{e}^{\mathsf{T}}_{\mathrm{RAD}}(\zeta)\hat{\mathbf{v}}} = \frac{\tan\phi_{A,i}}{\cos\varepsilon} \tag{2.5}$$

The only difference in Eq. 2.3 between images A and B is due to b. Therefore grid points for corresponding i have the same t'_y in both images and their offset in t'_x is proportional to $|b_A - b_B| = d_{\mathrm{BAS}}$. The disparity, or the changes in t'_x due to radius variations in ρ in Eq. 2.4 are very small in comparison to $d_{\mathrm{BAS}}/|$ and $|\mathbf{r}_{AB}\|$. Therefore we need to know $d_{\mathrm{BAS}}/|$ and $|\mathbf{r}_{AB}\|$ very precisely to avoid any bias in our height estimate. By mapping the grid onto the rectified images, it is only necessary to interpolate in t'_x when correlating the virtual surface images along an epipolar profile. The t'_y coordinate of the epipolar surface profile is given by Eq. 2.2. It is the vertical coordinate in the rectified images.

Figure 2.5 illustrates a grid with multiple epipolar profiles mapped onto the original images. The equivalent mapping to the rectified image is obtained if $\mathbf{R}'$ is replaced to $\mathbf{R}_A$ or $\mathbf{R}_B$ in Eq. 1.58. In the example, the positions of both spacecraft with respect to the Sun are $\|\mathbf{r}_{\mathrm{SC},A}\| = 10R_\odot$ and $\|\mathbf{r}_{\mathrm{SC},B}\| = 20R_\odot$ and they are separated by $20°$. Spacecraft A is 0.5 $R_\odot$ above and spacecraft B 0.5 $R_\odot$ below the solar equator so that the epipolar lines are inclined. As intended, the grid in Fig. 2.6 runs along the horizontal direction at a given vertical coordinate t'_y in the rectified images, which simplifies the problem by making each grid line 1D.

2.1.2 Virtual Intensity Profiles

The next processing step towards the stereoscopic reconstruction is to map the rectified image intensity data of the two spacecraft to the VIPs on the surface grid. The VIPs represent a brightness distribution on a virtual solar sphere with radius $R_\odot$, which reproduces exactly (with discretization errors) one of the image observations. Once the VIPs have been created for an epipolar profile and for each of the images, the correlation method can be performed.

After the grid has been mapped onto each rectified image, the virtual intensity profiles, or VIPs, can be calculated along the profile. The grid boundaries $\varphi_{i\pm\frac{1}{2}}$ are mapped to the respective image coordinates $t'_{x,i\pm\frac{1}{2}}$ of the rectified image, as described in the previous section, and the image intensities between the grid boundaries are integrated for the virtual surface brightness of grid cell i. The VIP surface brightness J_i of each grid cell i from image A is then

$$S_{A,i} = \frac{1}{\varphi_{i+\frac{1}{2}} - \varphi_{i-\frac{1}{2}}} \int_{\varphi_{i-\frac{1}{2}}}^{\varphi_{i+\frac{1}{2}}} I_A(\varphi)\, d\varphi, \tag{2.6}$$

where $I(\varphi)$ is the rectified intensity along a given epipolar profile at epipolar longitude φ. The VIP of ain image A is abbreviated by the vector $\mathbf{J}_A = (S_{A,1},\ \ldots\ ,\ S_{A,N})$. This is done similarly for image B. These VIPs are calculated on a φ-grid from the observed rectified images where the image t'_x coordinate and the surface φ coordinate are related by equation 2.3.

Once the two surface brightnesses are integrated into the VIPs they are then correlated inside a symmetric window centered at φ for different shifts between both VIPs to find the disparity at $\mathbf{r}$, and therefore dh at this position.

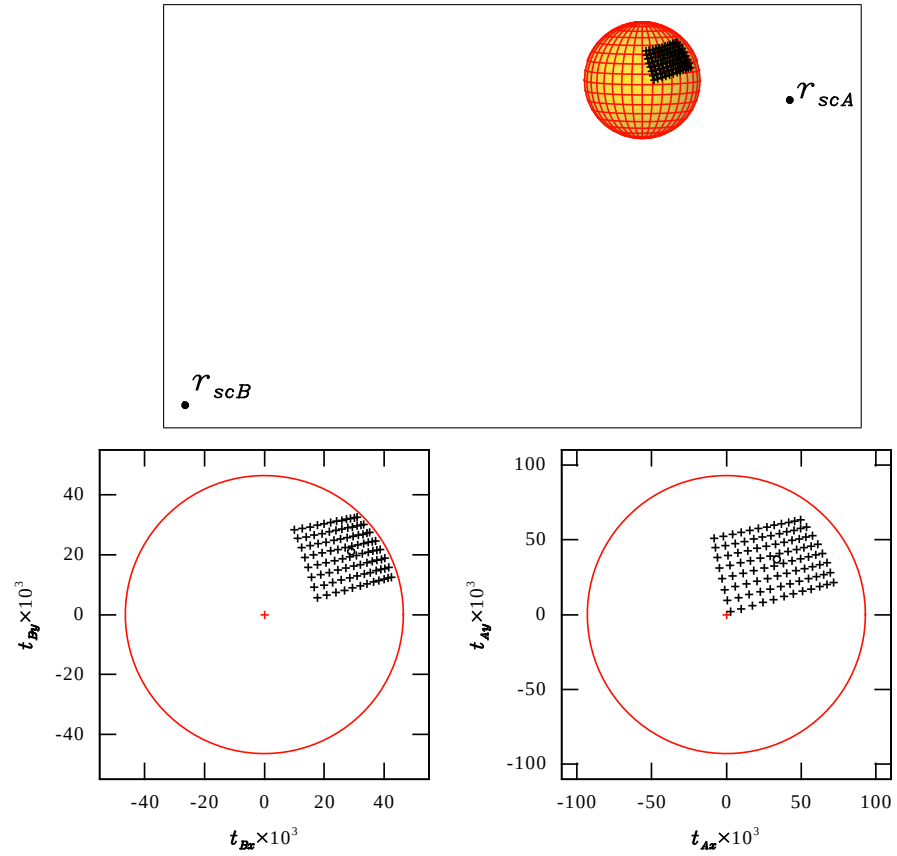

Figure 2.5: Illustration of two spacecraft at 10.8 (spacecraft A) and 21.5 $R_\odot$ (spacecraft B) observing the Sun, separated by $20°$. Spacecraft A is 0.5 $R_\odot$ above the solar equator and spacecraft B is one $R_\odot$ below. The upper diagram of the figure shows the spacecraft positions relative to the Sun's radius as seen by an external observer. The lower panels show the location of the surface grid in the respective spacecraft observations. The grid is equidistant parallel and perpendicular to the epipolar lines with about 50,000 km between the grid points in both directions. The small circle represents the reference point on the surface.

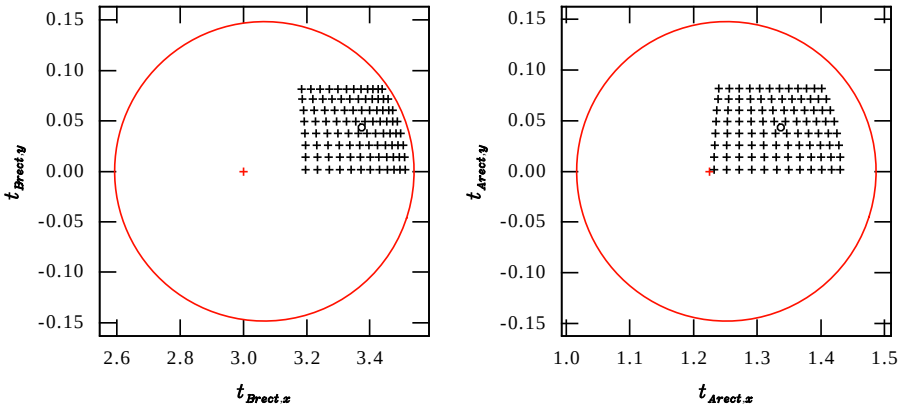

Figure 2.6: Grid points mapped onto the rectified image for the same viewing parameters as in Fig. 2.5. The grid points for the same epipolar plane ζ_j have the same y-coordinate in both images.

2.1.3 The Correlation Coefficient

Once the VIPs have been produced, the task is to find $d\rho$ from the correlation of the two virtual surface images. The coordinates of each point in the surface along an epipolar profile are $\xi = \rho\varphi$. With these coordinates, the height variations dh are now related to variations in the distance ρ from the epipolar center at $\zeta\hat{\mathbf{e}}_{\mathrm{POL}}(\zeta)$ (see Figs. 2.3, 2.4).

In order to find height variation estimates along an epipolar profile it is assumed that the disparity between the projection of $\mathbf{r}$ in the two epipolar lines is proportional to its height dh, relative to the standard solar radius. The approach used here consists of shifting windowed intervals of the VIPs, centered around $\mathbf{r}$, with respect to each other and computing the correlation value at each shift. The shift is determined for a range of different window widths. Under this approach the correlation will vary as a function of the shift between the VIPs at any given window width, so it can be assumed that the shift that yields the maximum correlation is proportional to the disparity between the VIPs and can be directly converted into a variation in height.

Once the two VIPs have been defined, a window function on the surface grid is defined centered around $\mathbf{r}$. The window function ($\mathbf{W}$) we use for the correlation must be continuous, symmetric, with a finite support and has to decay towards its boundaries. The window has the same resolution on the surface as the grid and the same grid size as the VIPs. Here we consider ξ as the distance variable along the epipolar surface profile. $\mathbf{J}_A$ and $\mathbf{J}_B$ are continuous along ξ, then $\mathbf{W} = \mathbf{W}(\xi', \xi_{\mathrm{width}})$, and:

$$\begin{aligned} \mathbf{W}(\xi', \xi_{\mathrm{width}}) &= \mathbf{W}(-\xi', \xi_{\mathrm{width}}) \quad \text{is symmetric} \\ \mathbf{W}(\xi', \xi_{\mathrm{width}}) &= 0 \quad \text{for } \xi' \geq \xi_{\mathrm{width}}., \quad \text{has finite support} \end{aligned}$$

where ξ' is a given surface position within the window, and ξ_{width} is half the window support. We use here

$$\mathbf{W} = \begin{cases} 1 & \text{if } \varrho\xi_{\mathrm{width}} \leq \xi' \leq \xi_{\mathrm{width}} \\ \frac{1}{2}\left(1 - \cos\left(\pi \frac{\xi'}{\varrho\xi_{\mathrm{width}}}\right)\right) & \text{if } 0 \leq \xi' \leq \varrho\xi_{\mathrm{width}}, \end{cases}$$

where ϱ is the tapered fraction of the window.

To estimate dh at each position along the profile, the VIPs are shifted within the window and then the correlation is performed for each shift. We use a weighted version of Pearson's correlation coefficient. This requires that the VIPs are centered and normalized to 1, so that the intensity variations occur around the 0 level and sensitivity differences between the images are largely eliminated..

We define the weighted mean ($\mathcal{M}$) of a VIP $\mathbf{J}$ at a given position ξ:

$$\mathcal{M}(\mathbf{J}; \xi) = \frac{\int_{-\xi_{\mathrm{width}}}^{\xi_{\mathrm{width}}} \mathbf{J}(\xi' + \xi)\mathbf{W}(\xi', \xi_{\mathrm{width}})d\xi'}{\int_{-\xi_{width}}^{\xi_{width}} \mathbf{W}(\xi', \xi_{\mathrm{width}})d\xi'}, \tag{2.7}$$

and a windowed product ($\mathcal{P}$) of the shifted VIPs $\mathbf{J}_A$ and $\mathbf{J}_B$:

$$\mathcal{P}(\mathbf{J}_A, \mathbf{J}_B; \xi, d\xi_A, d\xi_B) = \frac{\int_{-\xi_{\text{width}}}^{\xi_{\text{width}}} \mathbf{J}_A(\xi' + \xi + d\xi_A)\mathbf{J}_B(\xi' + \xi + d\xi_B)\mathbf{W}(\xi', \xi_{\text{width}})d\xi'}{\int_{-\xi_{\text{width}}}^{\xi_{\text{width}}} \mathbf{W}(\xi', \xi_{\text{width}})d\xi'}, \tag{2.8}$$

where $d\xi_A$ and $d\xi_B$ are the shifts of the VIPs A and B, respectively. Using Eq. 2.7 a centered vector ($\mathbf{J}_c$) can be obtained by

$$\mathbf{J}_c(\xi) = \mathbf{J}(\xi) - \mathcal{M}(\mathbf{J}; \xi), \tag{2.9}$$

and a centered and scaled vector ($\mathbf{J}_{cs}$) by

$$\mathbf{J}_{cs}(\xi) = \frac{\mathbf{J}_c(\xi)}{\sqrt{\mathcal{P}(\mathbf{J}_c, \mathbf{J}_c; \xi, 0, 0)}}. \tag{2.10}$$

The centering and scaling above applies likewise to $\mathbf{J}_A$ and $\mathbf{J}_B$. Following Eqs. 2.7 to 2.10, the Pearson coefficient (Pearson, 1895) for shifted VIPs $\mathbf{J}_{A,cs}$ and $\mathbf{J}_{B,cs}$ centered at ξ can be defined using Eq. 2.8 as

$$\mathcal{C}_{Pearson}(\xi, \xi_{\text{width}}, d\xi_A, d\xi_B) = \mathcal{P}(\mathbf{J}_{A,cs}, \mathbf{J}_{B,cs}; \xi, d\xi_A, d\xi_B). \tag{2.11}$$

The correlation coefficient of $\mathbf{J}_{A,cs}$ and $\mathbf{J}_{B,cs}$ for a given position $\varphi = \xi/\rho$ is calculated for a number k of shifts $d\varphi_{A,k} = k\delta\varphi \tan\gamma_A$ and $d\varphi_{B,k} = k\delta\varphi \tan\gamma_B$, along an epipolar profile for the VIPs A and B, respectively, where $d\varphi$ is a constant shift step size and $k = -M, \ldots, M$. Once the largest correlation is found for a given k, a second order interpolation around the maximum is calculated to find a reliable maximum at some non-integer shift $d\varphi_A = d\varphi_{A,kmax}$ and $d\varphi_B = d\varphi_{B,kmax}$.

The shift that yields the maximum correlation between $\mathbf{J}_{A,cs}$ and $\mathbf{J}_{B,cs}$ is considered as the local disparity between the images at $\mathbf{r}$. This shift is then converted onto the radius variations around ρ of this point, and lastly into dh. The way the shift is converted into a height is not straightforward, but it is explained in the following section.

This procedure considers a fixed window size ξ_{width}, but the correlation for one point can be performed for varying window sizes as well, so that dh is computed for the best combination of shift and window size.

2.1.4 Shift Between the VIPs, Viewing Angles and Surface Normals

Considering that a change from ρ into $\rho+d\rho$ for a surface point at a fixed $\varphi = \varphi_A = \varphi_B$, and a shift of the surface coordinates $\varphi_A = \varphi - d\varphi_A$ and $\varphi_B = \varphi + d\varphi_B$ for the standard distance ρ are approximately equivalent (see Fig. 2.7), then it is only necessary to calculate the VIPs once for the standard distance ρ and correlate them for different shifts. Once the optimal shifts in $d\varphi_A$ and $d\varphi_B$ for ρ have been found, then they can be converted into an equivalent $d\rho$ change for $\varphi_A = \varphi_B = \varphi$ using equation 2.3.

For spacecraft A,

$$\frac{\rho\sin(\varphi - d\varphi_A) - b_A}{||\mathbf{r}_{AB}||\cos^2\varepsilon - \rho\cos(\varphi - d\varphi_A)\cos\varepsilon} = \frac{(\rho + d\rho)\sin(\varphi) - b_A}{||\mathbf{r}_{AB}||\cos^2\varepsilon - (\rho + d\rho)\cos(\varphi)\cos\varepsilon}, \tag{2.12}$$

which is equivalent for B. This implies that in order to determine $d\rho$ at a given coordinate φ, the shifts $d\varphi_A$ and $d\varphi_B$ are not independent and must follow a relation when they are varied in search of the highest correlation.

To find the relation between the best angular shift and $d\rho$ we need the local viewing angle γ between the view direction to $\mathbf{r}$ from each spacecraft and the local surface normal projected into the epipolar plane. Using Eq. 2.1, the unit vector $\hat{\mathbf{r}} = \mathbf{r}/R_\odot$ is the radial surface normal at $\mathbf{r}$, and

$$\hat{\boldsymbol{\rho}} = \frac{\mathbf{r} - \zeta\hat{\mathbf{e}}_{\mathrm{POL}}(\zeta)}{\rho} = \hat{\mathbf{e}}_{\mathrm{RAD}}(\zeta)\cos(\varphi) + \hat{\mathbf{e}}_{\mathrm{BAS}}\sin(\varphi)$$

is the surface normal projected in the epipolar plane.

When expressing a point by its epipolar grid coordinates, there are three relevant directions: $\hat{\mathbf{r}}$, $\hat{\boldsymbol{\rho}}$ and the unit view direction

$$\hat{\mathbf{v}} = \frac{1}{\sqrt{1 + t_x^2 + t_y^2}}\,\mathbf{R}\begin{pmatrix} t_x \\ t_y \\ 1 \end{pmatrix}$$

from a pixel (t_x, t_y).

The viewing angle γ is defined as the angle of the view ray $\hat{\mathbf{v}}$ to the surface point at $\mathbf{r}$ with respect to the surface normal projected in the epipolar plane $\hat{\boldsymbol{\rho}}$. The angle γ is then given by

$$\sin\gamma = \hat{\mathbf{e}}_{\mathrm{POL}}^{\mathsf{T}}(\zeta)(\hat{\boldsymbol{\rho}} \times \hat{\mathbf{v}}) \tag{2.13}$$

The sign of the angle is defined as in Fig. 2.7: γ is positive for a view direction clockwise tilted with respect to $\hat{\boldsymbol{\rho}}$ when looking downward onto the epipolar plane in $-\hat{\mathbf{e}}_{\mathrm{POL}}^{\mathsf{T}}(\zeta)$ direction.

If $d\varphi$ and $d\rho$ are small compared to $\pi/2$ and ρ, respectively, then the ρ-curve in Fig. 2.7 can be considered as a straight line and $\mathbf{v}$ and $\mathbf{v}'$ as parallel for both A and B. Then

$$d\rho = \frac{\rho d\varphi_A}{\tan\gamma_A} = \frac{\rho d\varphi_B}{\tan\gamma_B}, \tag{2.14}$$

so that $d\varphi_A$ and $d\varphi_B$ have to be varied with a constant ratio $d\varphi_A/d\varphi_B = \tan\gamma_A/\tan\gamma_B$. This ratio makes sure that the height change dh is calculated at φ and not at a surface coordinate displaced from φ.

Associated to the viewing angles is the theoretical height resolution h_{th} at $\mathbf{r}$. If the pixel size for each camera is such that the pixel corresponds to a viewing beam of width ΔA and ΔB, respectively a theoretical rhombus is formed by the intersection of both beams. The theoretical height resolution is the height of this rhombus (see Fig. 2.8) and is

$$h_{th} = \frac{\Delta B\cos\gamma_A + \Delta A\cos\gamma_B}{\sin(|\gamma_A| + |\gamma_B|)}. \tag{2.15}$$

The maximum possible geometric error along the ρ direction is $\pm\frac{1}{2}h_{th}$. The mean error, determined by the standard deviation, is one third to one half of $\pm\frac{1}{2}h_{th}$, depending on the shape of the rhombus in Fig. 2.8, i.e., on the view angles and the

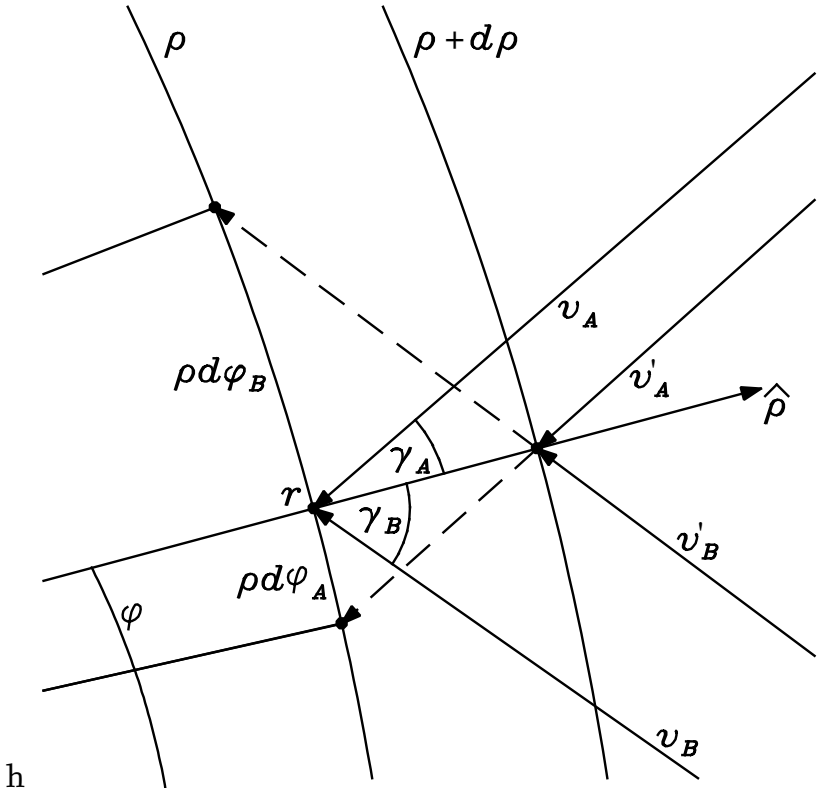

Figure 2.7: A zoom into the region around $\mathbf{r}$. The view rays $\mathbf{v}_A$ from $\mathbf{r}_{scA}$ and $\mathbf{v}_B$ from $\mathbf{r}_{scB}$ to the surface point $\mathbf{r}$ are shown. The direction of $\mathbf{v}_A$ makes an angle γ_A with the rectified optical axis projected into the epipolar plane ζ and with the projected surface normal direction $\hat{\rho}$ in the epipolar plane. This figure illustrates the changes of the view rays when the surface point is slightly elevated to distance $\rho + d\rho$. The new rays $\mathbf{v}'_A$ and $\mathbf{v}'_B$ are the same which result for ρ but with an appropriate shift in the surface coordinates by $d\varphi_A$ and $d\varphi_B$, respectively, as displayed with the dashed lines. φ counts positively in counterclockwise direction.

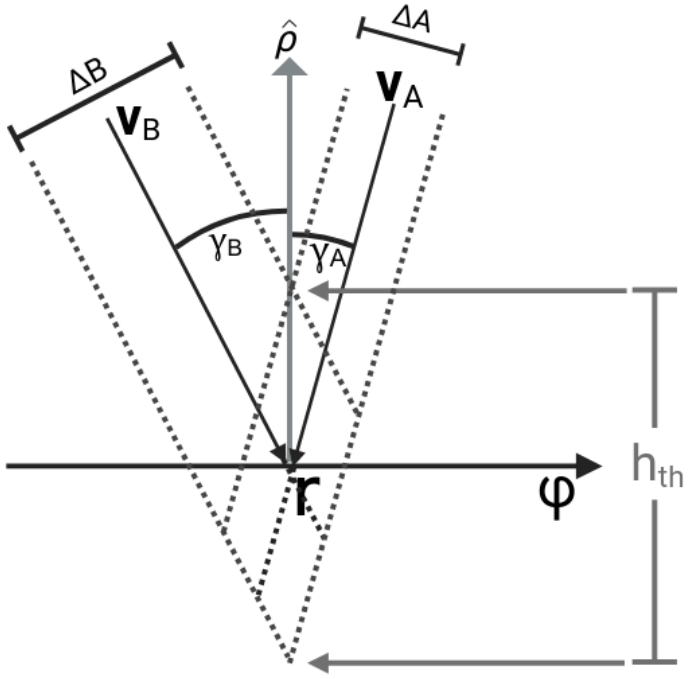

Figure 2.8: Theoretical height resolution. h_{th} is the height of the rhomboid formed by the intersection of the beams of width ΔA and ΔB, at inclination angles γ_A and γ_B, respectively, and $\bar{h}_{th}$ its mean, which measures the maximum geometrical error.

ratio of ΔA to ΔB. As an estimate for the geometrical mean error we will use $\frac{1}{4}h_{th}$. Height variations smaller than this cannot reliably be reproduced and fluctuations smaller than this size in our results may be random artifacts. We hope, however, that our effective height error is somewhat better than the above estimate. The optimal shift of the intensity profiles from which the height is determined employs a subpixel interpolation of the correlation function (see Sections 2.1.3 and 2.1.5, here more details of the height determination are described). This probably yields a height estimate with an error better than the geometrical uncertainty presented in Fig. 2.8 due to the intersection of only two pixel beams.

2.1.5 Computing Height Variations From the Optimal Shifts

The last step to estimate dh for $\mathbf{r}$ from the optimal shift of the VIPs. This optimal shift of the window from φ to $\varphi_A \to \varphi - \Delta\varphi_A$ and $\varphi_B \to \varphi + \Delta\varphi_B$ is equivalent to a change of the view rays of $\mathbf{v}_A \to \mathbf{v}'_A$ and $\mathbf{v}_B \to \mathbf{v}'_B$ (see Fig. 2.7) which corresponds to the view rays pointing at φ but for an elevated radius $\rho + d\rho$. This radius change can be calculated by Eq. 2.12 or by Eq. 2.14.The corresponding change in height then is

$$dh = \sqrt{(\rho + d\rho)^2 + \zeta^2} - R_\odot \;=\; \sqrt{R_\odot^2 + 2\rho d\rho + d\rho^2} - R_\odot. \tag{2.16}$$

To obtain the height variations along an epipolar profile, this procedure is repeated throughout each cell φ_i within an epipolar profile.The analysis of successive epipolar profiles can be performed similarly as above by varying ζ. This is equivalent to just varying t'_y in the rectified images.

2.2 The Optimization Method

Additionally, an optimization procedure was applied to extend the correlation method when applied to the test data. The practical reformulations of the method to be applied to test data are presented in Chapter 3. However, a brief description of the optimization procedure is included in this section to give an introduction of the calculations performed later in this work.

With the correlation method, the idea is to maximize $\mathcal{C}_{Pearson}$ to find the disparity of $\mathbf{r}$ between $\mathbf{J}_A$ and $\mathbf{J}_B$. As alternative to the correlation, a cost function can be minimized by varying the height vector h used to map the image intensities onto the surface grid. The cost function is defined such that

$$f_{cost} = 1 - \mathcal{C}_{Pearson} \tag{2.17}$$

so that the idea to maximize the correlation between the VIPs is now replaced by the attempt to minimize a suitable cost function of them. f_{cost} is divided by the number of surface grid cells so that the results obtained with different grid sizes are comparable. Under this approach the task is to find a height vector h, such that each f_{cost} is minimized wherever the surface grid is positioned.

Under this approach the support of the window may cover the entire profile and all height values $h(\xi)$ are determined simultaneously. As opposed to the correlation method which considered one height dh for the entire window range, the optimization always considers a height vector. A solution is achieved by solving a non linear optimization problem.

For this method a height vector determines how the image intensities from both spacecraft are mapped onto the surface grid, therefore $f_{cost} = f_{cost}(h)$ is the quantity to be minimized. This requires the gradient of f_{cost} with respect to the h-vector so that h is changed iteratively so as to make f_{cost} smaller.

A change in h causes a change in $\mathbf{J}_A$ and $\mathbf{J_B}$ through their mapping onto the surface grid. To map the image intensities onto the surface grid, with the use of a height vector, the position of a grid cell has a corresponding pixel position in the image, which is the one integrated into that surface cell. If the height of a given surface cell changes, the corresponding image position will change as well, producing a different VIP. Figure 2.9 illustrates how a change in h_i yields a different mapping onto ξ.

If both VIPs are produced using the same height vector to map the image intensities onto the surface grid, the optimal height vector would be that one that produces two identical VIPs. This is the aim of the optimization method: to iteratively change h so that after each iteration both VIPs are more similar to each other and $f_{cost}(h)$ is as small as possible. However, the algorithm might reach more than one minimum, and it is therefore convenient that the initial height $h(\xi)$ at the start of the iterative solution of Eq. 2.17 is a good guess. For this purpose the computed height vector obtained through the correlation is useful.

The optimization algorithm used in this work is named after Broyden, Fletcher, Goldfarb and Shanno, or BFGS. This is a second order optimization algorithm based on a gradient search, which means that the algorithm makes use of the first and second derivative of the cost function f_{cost} at each iteration. More information on this optimization procedure can be found in Nocedal and Wright (2006).

An effect of the optimization algorithm used here, is that the final iteration of $f_{cost}(h)$ might yield a h vector with irregular fluctuations in regions due to noise in

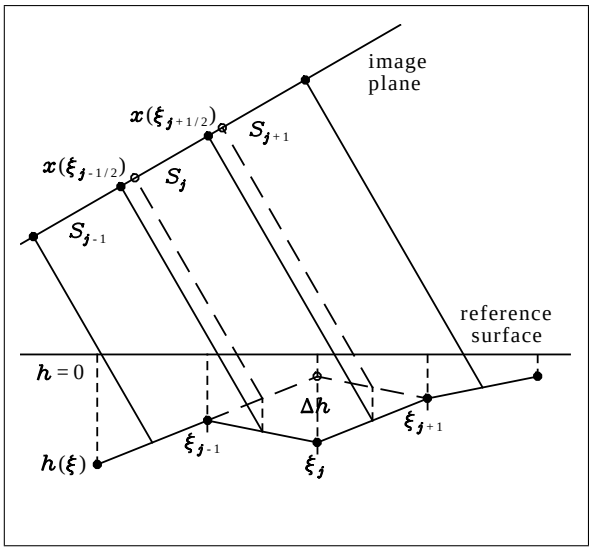

Figure 2.9: Sketch to illustrate the effect of a change in h_j on the integration ranges in the image. If h_j increases by Δh, the heights $h(\frac{1}{2}(\xi_{j-1}+\xi_j))$ and $h(\frac{1}{2}(\xi_j+\xi_{j+1}))$ at the grid boundaries increase by $\Delta h/2$. Consequently, the projections of the two grid boundaries move in the image by $\Delta h/2$ and affects the integration range of elements S_{j-1}, S_j and S_{j+1}. If the projections of the two grid boundaries fall into the same image pixel, S_j does not change because the contributions from both boundaries cancel. Recall that the view angle for the example in the figure is $\gamma < 0$.

the data. These fluctuations do not result in a clear change in the mapping of the VIPs, especially where the VIPs are almost flat. Here, f_{cost} is sensitive to changes in h. Therefore f_{cost} may still be small, but with fluctuations in h that are not realistic. To avoid too strong oscillations on the final solution, a regularization term is added to f_{cost}, to reduce the impact of the second derivative of h:

$$f_{cost,regularized} \simeq f_{cost} + \mu \int \left(\frac{d^2h}{d\xi}\right)^2 d\xi. \tag{2.18}$$

In the expression above, μ is the regularization parameter, which helps obtain a solution that is balanced between sufficient fine structure, obtained by decreasing μ, and smaller irregular fluctuations, which are suppressed by increasing μ. The regularization term must always be positive, so that if the second derivative of h becomes too large, its impact is to enhance f_{cost}.

Chapter 3

Application of the Method to Test Data*

The method for solar stereoscopy developed for this work was applied to synthetic MHD data of a photospheric pore in order to test the performance of the method and understand its limitations and performance before applying it to real observations of sunspots. The way the synthetic MHD images were produced has an ideal and simplified geometry, in which the epipolar lines are already horizontal. For this reason both the mapping and the correlation procedures were modified to be applied to them, and are described in this chapter.

3.1 Test Data

In order to produce the synthetic data to test the stereoscopic method, the MURaM numerical simulation code (Vögler et al., 2005) was used to carry out 3D radiation MHD simulations of a typical photospheric structure (for details on the simulation see Riethmüller et al., 2017). The results obtained with MURaM are in good agreement with observational data (e.g. Schüssler et al., 2003; Keller et al., 2004; Hirzberger et al., 2010; Riethmüller et al., 2014), therefore it can be assumed the results obtained for this particular simulation (Riethmüller et al., 2017) are close to real observational data, so their output can be used as the test data to reconstruct height variations in the solar surface using the method previously described.

The test data consist of a slice of small unipolar flux concentrations, namely a photospheric pore, surrounded by small scale magnetic structures within a quiet-Sun-like area (see figure 3.1). In this work a 812×812 pixels slice of the simulation, performed over a height range of 700 km, is used. The resolution of the grid in the ξ, y, and z coordinates of the box simulation was $[41.67, 41.67, 15.89]$ km, respectively.

In order to produce synthetic observations from different viewing angles γ, a standard procedure within the SPINOR radiative transfer inversion code (see Solanki, 1987; Frutiger et al., 2000) was applied to its forward calculation mode. This allows to compute synthetic Stokes spectra around the Fe I 617.3 nm line as the Polarimetric Helioseismic Imager on board the Solar Orbiter SO/PHI (see Solanki et al., 2020) and the Helioseismic and Magnetic Imager aboard the Solar Dynamics Observatory (SDO/HMI) (see Scherrer et al., 2012) would observe them. The applied spectral

* This chapter is strongly based on the paper *Photospheric Stereoscopy: Direct Estimation of Solar Surface-Height Variations* from Romero Avila et al. (2024), but the content was adapted to fit the format of this thesis. All the figures in this chapter were were taken and modified from this paper.

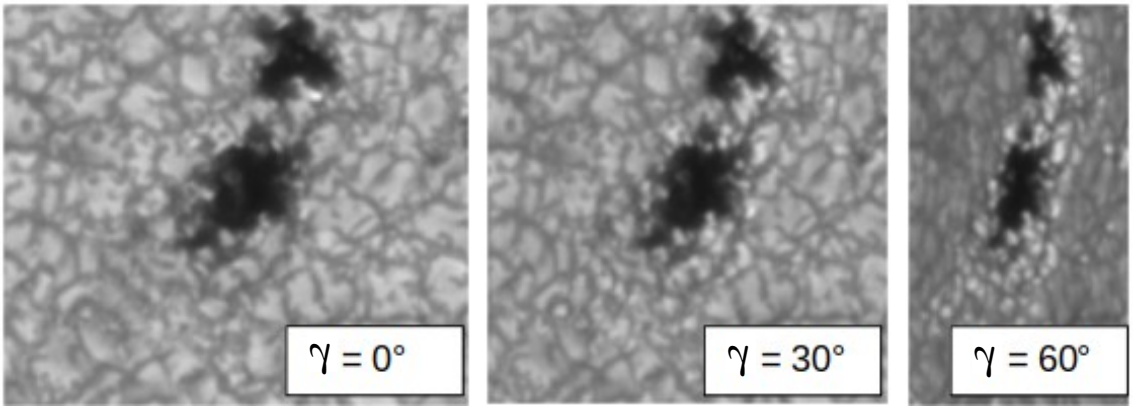

Figure 3.1: Test data for the views corresponding to $\gamma = 0°$ (i.e. from directly above), $\gamma = 30°$, and $\gamma = 60°$.

synthesis procedures can be found in Valori et al. (2022), where they already been described. More information on SO/PHI and SDO/HMI can be found in Chapter 4.

The resulting data contain the synthesized contributions to the observed intensity of each simulation cell along each ray across the MURaM simulation cube. The contribution of each cell can be described in terms of their response functions (Landi Degl'Innocenti & Landi Degl'Innocenti, 1977; Ruiz Cobo & del Toro Iniesta, 1994), which are then used as weight functions for the integration of the line-of-sight integration with optical depth τ. The computation of the response functions is done from the atmospheric model created by SPINOR for an inversion of synthetic observation. SPINOR has a subroutine called MapTau, that transforms the response function in a way that they depend on the geometrical height instead of the optical depth, to find the average formation heights of the emitted rays. This subroutine computes the radiative transport through the MURaM simulation for each viewing angle γ. Its output is a height coordinate along the line-of-sight, which is compatible with the optical depth scale of the response functions. To obtain a reference height, or the best possible estimate of the formation height of the observed light, the dataset is re-binned to match the spatial resolution of the observations and is integrated over the line-of-sight for each ray path. The resulting filtergrams and reference height maps for different values of γ are used as the data to test the height variation estimates obtained with the method described in the previous Chapter 2.

In this work, only data in the continuum spectral region are used. The data was synthesised in the continuum region close to the Fe I 6173 Å line (300 mÅ outside the mean line center as observed with SO/PHI). Continuum observations from different vantage points, or different inclination angles γ, are formed at different geometrical heights, so an intrinsic error in direct comparison results from the formation height differences. To maintain this intrinsic error small, the differences in the inclination angles are small (at least for the reference cases shown in Sect. 3.3.1 and 3.3.2), and in some cases even symmetric around $\gamma = 0°$.

3.2 Practical Reformulations of our Method for the Test Data

The way the synthetic images were produced corresponds to a simplified case for the application of the stereoscopic method. For the simulated data used in this chapter, a very simplified spacecraft configuration geometry is assumed. The surface plane is spanned by the ξ, y-axes, being ξ the length coordinate along the surface profile line. The virtual viewing points are in the ξ, z-plane, in the direction of the assumed view angles γ, and at an infinite distance.

The images have an orientation such that the epipolar lines are oriented along their horizontal axis, so that any surface profile line will map to the corresponding epipolar line in the images. The surface profiles on the different epipolar planes are parallel and can be labeled by their y-coordinate.

It is convenient to determine a unique physical reference point $\mathbf{p}_{\mathrm{ref}}$ on the surface profile of both images. In the case of the test images, the absolute height reference $z = 0$ was implicitly defined in the radiative transfer integrations from the MHD box. Nevertheless, the computed height variations and the z-dimension in the obtained results represent relative quantities, not absolute height levels in the solar photosphere. This is because the MapTau routine computes response functions relative to an arbitrary depth $z = 0$, which is given by the horizontal average of the optical depth $\tau = 1$ layer at 5000 Å for vertical emergence (for more details see Martínez Pillet and Vázquez, 1993; Mathew et al., 2004; Löptien et al., 2018). The tests performed in this chapter focus on relative height variations along the surface profile lines.

The next processing step towards the stereoscopic reconstruction is to map the image intensity data of the two spacecraft to virtual intensity profiles (VIPs, see Chapter 2) on the surface profile line.

To obtain the VIPs, first the reference point $\mathbf{p}_{\mathrm{ref}}$ has to lie on the surface profile line at a coordinate value ξ_{ref}. Then its respective pixel coordinate along the epipolar line of both images has to be found. The test images are equivalent to the rectified images in Chapter 2, so each epipolar line lies exactly along the image x axis. With these data we replace t'_x for p_x along the epipolar lines in the images, and the surface coordinate $\rho\varphi$ now becomes ξ. In this case, $p_{x,A}$ and $p_{x,B}$ are the respective coordinates along the epipolar line, with a scale of one pixel width per $p_{x,A}$ and $p_{x,B}$ unit, with arbitrary coordinate origins. Using these definitions, a simple mapping between pixel and surface coordinates is given by

$$p_{x,A}(\xi) = p_{\mathrm{ref},x,A} + \frac{1}{\Delta\xi_A}\left((\xi - \xi_{\mathrm{ref}})\cos\gamma_A - h(\xi)\sin\gamma_A\right), \tag{3.1}$$

and similarly for B (see figure 3.2). Here, ξ and h are scaled to the same units. $\Delta\xi_A$ is a surface element spaced by one image pixel of image A (and equivalently for image B) with a vertical view.

The VIP along a surface profile line in image A (and equivalently in image B) is then

$$\mathbf{J}_A(\xi \mid h) = I_A(p_{x,A}(\xi))\left|\frac{dp_{x,A}}{d\xi}\right|\Delta\xi_A, \tag{3.2}$$

where $I_A(p_{x,A})$ is the pixel intensity along the epipolar line. The dependency on the function h as input for $\mathbf{J}_A$ is mentioned explicitly because it is required for the

mapping of (3.1) and for the Jacobian derivative $|dp_{x,A}/d\xi|$. The factor $\Delta\xi_A$ in Eqs. 3.1 and 3.2 makes up for different resolutions of the different images A and B while the derivative in Eq. 3.2 takes account of the intensity changes visible on the inclined true surface $h(\xi)$. $\mathbf{J}_A(\xi \mid h) = I_A(p_{x,A}(\xi))$ is independent of h for a vertical view $\gamma_A = 0$. For (3.1) it is required that $\tan\gamma_A < dh/d\xi$. If this limit is exceeded, the slope of $h(\xi)$ at a given point is steeper than the view direction's inclination, so that part of the surface remains hidden from this viewing point.

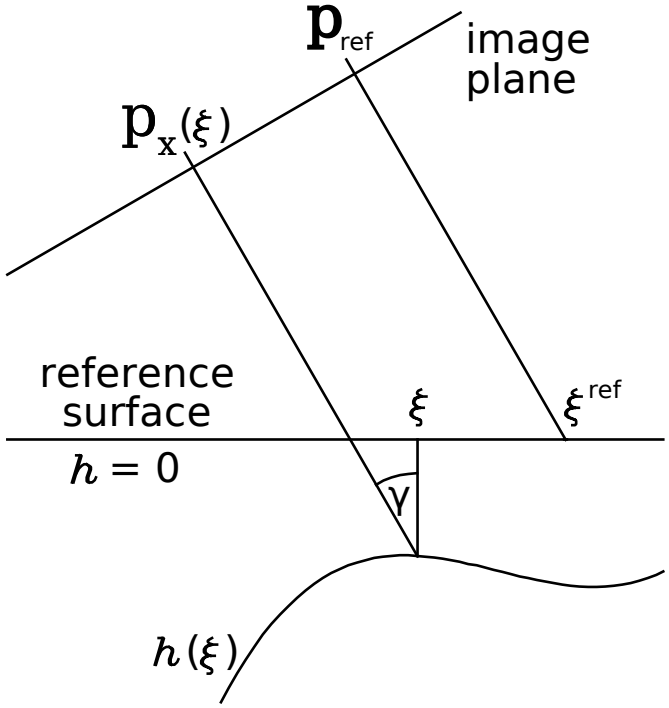

Figure 3.2: Scheme of the relation of Eq. 3.1 for one image with an inclined view direction.

After the mapping, the VIPs $\mathbf{J}_A(\xi)$ and $\mathbf{J}_B(\xi)$ can be directly compared and if the assumption about the response function holds and $h(\xi)$ was chosen correctly, the VIPs should be identical.

Choosing a wrong height in a section of the line profile, would result in a local shift (disparity) of corresponding structures between $\mathbf{J}_A(\xi)$ and $\mathbf{J}_B(\xi)$. Therefore $h(\xi)$ is only sensitive where the image intensity along the line has small-scale variations that can be measured.

As described in Section 2.1.5 of Chapter 2, $\mathbf{J}_A(\xi \mid h)$ and $\mathbf{J}_B(\xi \mid h)$ must be windowed, centered and scaled for the stereoscopic comparison. In this chapter two different approaches to determine $h(\xi)$ by comparing $\mathbf{J}_{A,cs}(\xi \mid h)$ and $\mathbf{J}_{B,cs}(\xi \mid h)$ are presented.

3.2.1 Correlation Method

With this approach the local height $h(\xi_{\text{cent}})$ at the center of the window ξ_{cent} is obtained by solving

$$h_{\text{corr}}(\xi, \xi_{\text{width}}) = \underset{h_{\text{cent}}}{\operatorname{argmax}}\, \mathcal{C}(\xi_{cent}, \xi_{\text{width}}, h_{\text{cent}}),$$

where the dependency on the shifts $d\xi_A$ and $d\xi_B$ (see Eq. 2.11) is replaced by the dependency on h_{cent}. Instead of using the full profile function $h(\xi)$, a constant height h_{cent} inside each window, considered representative for the height at the window center ξ_{cent} is used.

From Eq. 3.1 we see that all the image data inside the window is shifted in ξ by $h_{\text{cent}} \tan\gamma_A$ and $h_{\text{cent}} \tan\gamma_B$. Since $\tan\gamma_A \neq \tan\gamma_B$, the surface profile brightnesses, I_A and I_A, are shifted differently until the correlation is maximized at the correct value of h_{cent}.

Replacing $h(\xi)$ by a constant h_{cent} inside the window around ξ_{cent} causes some inconsistency, which is larger the larger the window width ξ_{width}. For this reason, Eq. 3.2.1 is used initially as a first estimate for the correct $h(\xi_{\text{cent}})$ for a window size ξ_{width} that is sufficiently large to find a stable minimum.

Afterwards, ξ_{width} is iterated to smaller sizes and the computed minima of h_{corr} is compared with the resulting one from the previous wider window sizes. While ξ_{width} decreases, the solution of Eq. 3.2.1 becomes increasingly prone to errors induced by local intensity variations and noise.

The iteration is stopped when the discrepancy between predicted and computed h_{corr} becomes too large or if a minimum ξ_{width} is reached, and the latest h_{corr} is taken as $h(\xi_{\text{cent}})$.

3.2.2 Optimization Method

As mentioned in Section 2.2 of Chapter 2, an optimization procedure was applied to extend the correlation method when it is applied to the test data. This second approach helps to avoid the inconsistency of the correlation method by minimizing $f_{\text{cost}}(\xi_{cent}, \xi_{\text{width}}, h)$ with respect to $h(\xi)$

As stated in Chapter 2, the Broyden–Fletcher–Goldfarb–Shanno (BFGS) algorithm is used. This algorithm is based on a gradient search, meaning that it requires the gradient $\nabla_h f_{\text{cost}}(\xi_{cent}, \xi_{\text{width}}, h)$, that can be analytically calculated by tracing the h-dependence by chain rule down to (3.1) and (3.2).

For the calculations, it is assumed that the grid for ξ is equidistant, and then it is mapped to the images by (3.1). Changing a single height element $h(\xi_i) \to h(\xi_i) + \Delta h$ will result in a shift in the mapping of the grid boundaries of cell i onto the image and will therefore affect the values of $J_k(\xi_j)$ at $j = i-1, i, i+1$ (see Fig. 2.9). However, these modifications proportional to Δh become small in regions where the image data $I_k(x_k(\xi)$ has little structure, so that the local gradient $\nabla_h f_{\text{cost}}$ becomes small and the minimization algorithm becomes insensitive to changes in $h(\xi)$, and data noise may have a larger influence on f_{cost}. The regularization term in (2.18), proportional to the regularization parameter μ is added to keep the noise dependence small. Depending on the magnitude of μ, this term will smooth $h(\xi)$ and lead to some loss of resolution and detail, but it will also stabilize the solution where $f_{\text{cost}}(\xi_{cent}, \xi_{\text{width}}, h)$ is too insensitive.

3.3 Performance on the Method With Test Data

To judge the performance of our method, the resulting height variations are then compared to the height variation of the response function $R_T(\xi, z)$.

The methods described in Section 3.2 depend on a number of parameters which may have an effect on the results, and it is convenient to first determine which set of parameters yields the best results. In both approaches, the correlation and the optimization, a free parameter is the surface grid spacing $\Delta\xi$ to which the VIPs from both view points are discretized. Another free parameter is the width ξ_{wdth} of the window function w used for the scaled intensity profiles S_k. It can be expected that for the optimization method, ξ_{wdth} has a minor influence on the results, but it requires another parameter, the regularization coefficient μ, which controls the main smoothing of $h(\xi)$.

To display the influence of these parameters on the results, their effects are shown for a standard case, with viewing configuration of $\gamma = \mp 20^\circ$ to the vertical view and images without noise. Once the set of optimal parameters for the standard case mentioned was found, other parameters given by different observational circumstances like different viewing angles, different sizes of the image pixels and different noise levels, are investigated.

The biggest advantage of working with synthetic data is the capacity to quantitatively compare the resulting height variation estimates along a surface profile with the vertical variation of the response function. For this reason we characterize the moments p of the response function relative to an arbitrary height reference

$$M_p(\xi) = \int (z - z_{\mathrm{ref}})^p R_T(\xi, z)\, dz. \tag{3.3}$$

The response function $R_T(\xi, z)$ used above was calculated for a vertical view direction. Now, a local, ξ-dependent parameter Err is introduced, which measures the distance between $h(\xi)$ and the vertical mean h_{mean} of the response function with respect to its height extent h_{wdth}:

$$\mathrm{Err}(\xi) = \frac{|h(\xi) - h_{\mathrm{mean}}(\xi)|}{h_{\mathrm{wdth}}(\xi)}, \tag{3.4}$$

$$\text{where} \qquad h_{\mathrm{mean}}(\xi) = \frac{M_1(\xi)}{M_0(\xi)} \qquad \text{and} \qquad h_{\mathrm{wdth}}(\xi) = \sqrt{\frac{M_2(\xi)}{M_0(\xi)} - h^2_{\mathrm{mean}}(\xi)}. \tag{3.5}$$

Figure 3.3 displays an example of a typical response function $R_T(\xi, z)$. For a single point in the quiet Sun, the response function is shown as a function of the optical depth (top) and of geometrical height (bottom). $R_T(\xi, z)$ is often skewed so that the maximum of $R_T(\xi, z)$ generally lies below h_{mean} by around h_{wdth}. Additionally, a global measure to asses the quality of our results along an entire ξ-profile is defined as

$$\epsilon = \left(\frac{\int Err^2(\xi) d\xi}{\int d\xi} \right)^{\frac{1}{2}}. \tag{3.6}$$

3.3.1 Test of the Correlation Method

The critical parameters in this method are how $J_k(x_k(\xi))$ is discretized (see equation 3.2) and the smallest window size ξ_{wdth} used in (2.1.3). To test both parameters a standard surface grid spacing $\Delta\xi = dx$ is chosen which corresponds to the pixel size dx (in km) at a vertical view direction $\gamma = 0^\circ$ mapped to the surface. This spacing will

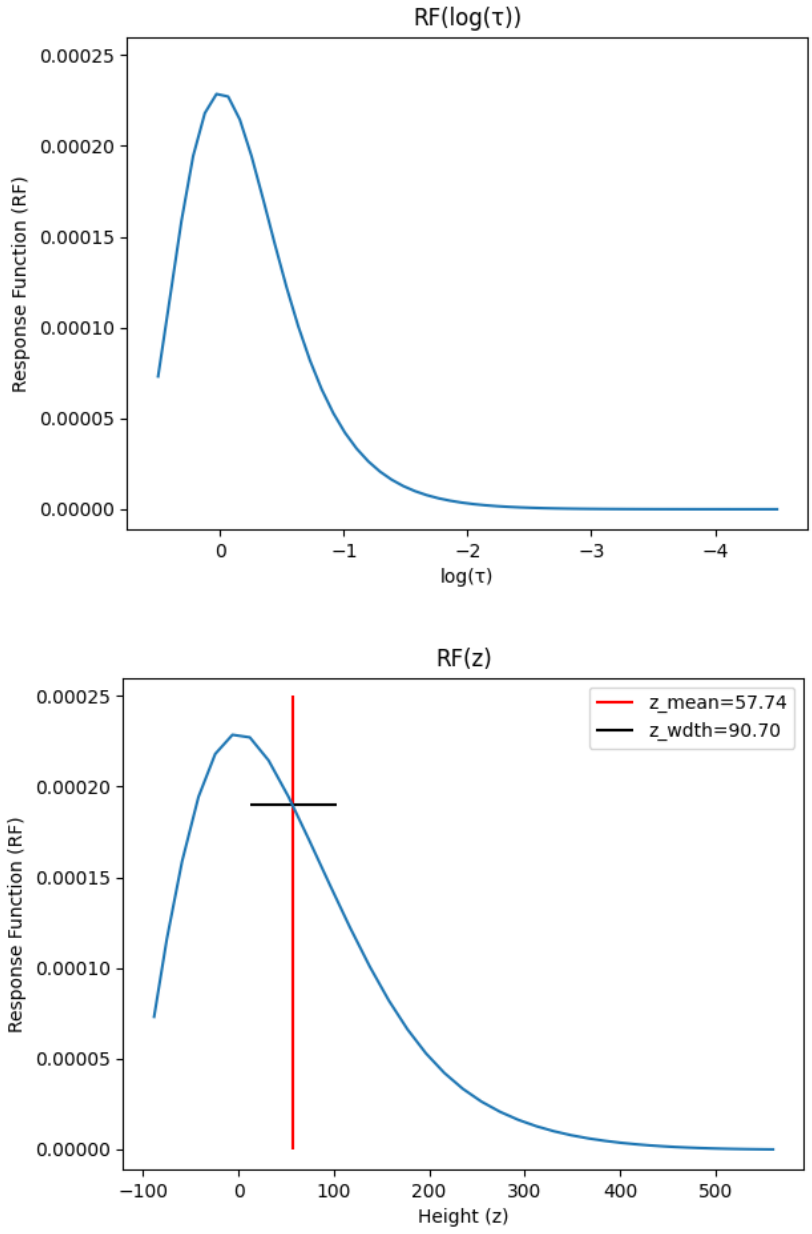

Figure 3.3: An example of the RF as a function of the optical depth τ (top), and of the height h (bottom) at a given position ξ along the profile. In the right diagram is marked h_{mean} with a red vertical line and the height extent $\pm h_{\mathrm{wdth}}$ as the black horizontal range.

be called $\Delta\xi_{\mathrm{or}}$ further on. For oblique views, a grid interpolation is required when $\mathbf{J}_A(p_{x,A}(\xi))$ and $\mathbf{J}_B(p_{x,B}(\xi))$ are convolved with the window function in order to obtain $\mathbf{J}_{A,cs}$ and $\mathbf{J}_{B,cs}$ in (2.7).

The reconstructed height $h(\xi)$ is displayed along a surface profile across the simulated active region in figure 3.4. The height was calculated separately for two different window size ranges of $\xi_{\mathrm{wdth}} = 15$ to $20\Delta\xi_{\mathrm{or}}$ (top) and $\xi_{\mathrm{wdth}} = 30$ to $60\Delta\xi_{\mathrm{or}}$ (bottom). First the correlation height was estimated using the maximum allowed ξ_{wdth} and then ξ_{wdth} was reduced until the smallest size for which the height could not be estimated anymore due to a lack of structure inside of the window, or until the smallest ξ_{wdth} of the allowed range was reached.

The determined height $h(\xi)$ is the one obtained from the smallest window size inside the respective size range, displayed by the red curves in figure 3.4. At some points in ξ, the correlation procedure will yield wrong localized outliers, which arise from numerical errors and are to be expected. To reduce these outliers, $h(\xi)$ is smoothed using a rolling average of 8 data points, after which the height estimate of the green curves is obtained.

To have a visual comparison of the height $h(\xi)$ reconstructed with this method with the reference height from the simulation for test images (referred to as true height), a range of heights associated to $R_T(\xi,\tau)$ is displayed in a gray scale. The lightest gray range represents $R_T/R_{Tmax} \simeq 0.5$, the intermediate range to $R_T/R_{Tmax} \simeq 0.7$, and the darkest to $R_T/R_{Tmax} \simeq 0.9$, where R_{Tmax} is the maximum value of the response function at a fixed ξ_{cent}. These curves represent the height variation around the response function maximum with respect to the optical depth.

The mean error ϵ derived from Eq. 3.6, for the two window size ranges of ξ_{wdth} are $\epsilon = 1.44$ for $\xi_{\mathrm{wdth}} = 15$ to $20\Delta\xi_{\mathrm{or}}$, and $\epsilon = 2.26$ for $\xi_{\mathrm{wdth}} = 30$ to $60\Delta\xi_{\mathrm{or}}$. The minimal cost function for each case is 0.11 and 0.09, respectively. The reconstructed height $h(\xi)$ has a better agreement with the true height for the narrower window size ranges, while for the wider window size range a smaller cost function was obtained. When using real data, the cost function value, which measures the agreement between the two VIPs $\mathbf{J}_{A,cs}$ and $\mathbf{J}_{B,cs}$, is the only number that can be used to assess the quality of the results, since a reference true height is not available. Therefore, using the cost function as a quality parameter must be done with some care.

In this comparison, and in all the further results that will be shown in this chapter, the calculated height $h(\xi)$ for the quiet Sun systematically lies below the height of the maximum response function, or true height. The response function in the quiet Sun is very skewed with a tail upwards, so that the vertical barycenter h_{mean} of the response function is even higher than the height of the maximum response function. This difference grows for more inclined view directions. However, this difference is much smaller in the umbra of the active region.

The relative error (Eq. 3.5) is displayed in all the figures in the bottom panels. Err measures the mean error with respect to the width of the response function, so for any error smaller than $Err = 1$, the height estimate can be considered to have a good agreement with the true height. $Err = 1$ is marked in the figures as a dashed line. The agreement is best in the deepest parts of the active region, and discrepancies arise towards the quiet Sun. The most visible discrepancies arise in the penumbral area, where strong, fast height gradients occur. Even though we can only calculate relative height variations with this method, the error number Err allows to know the regions where the estimated height behaves similarly to the true

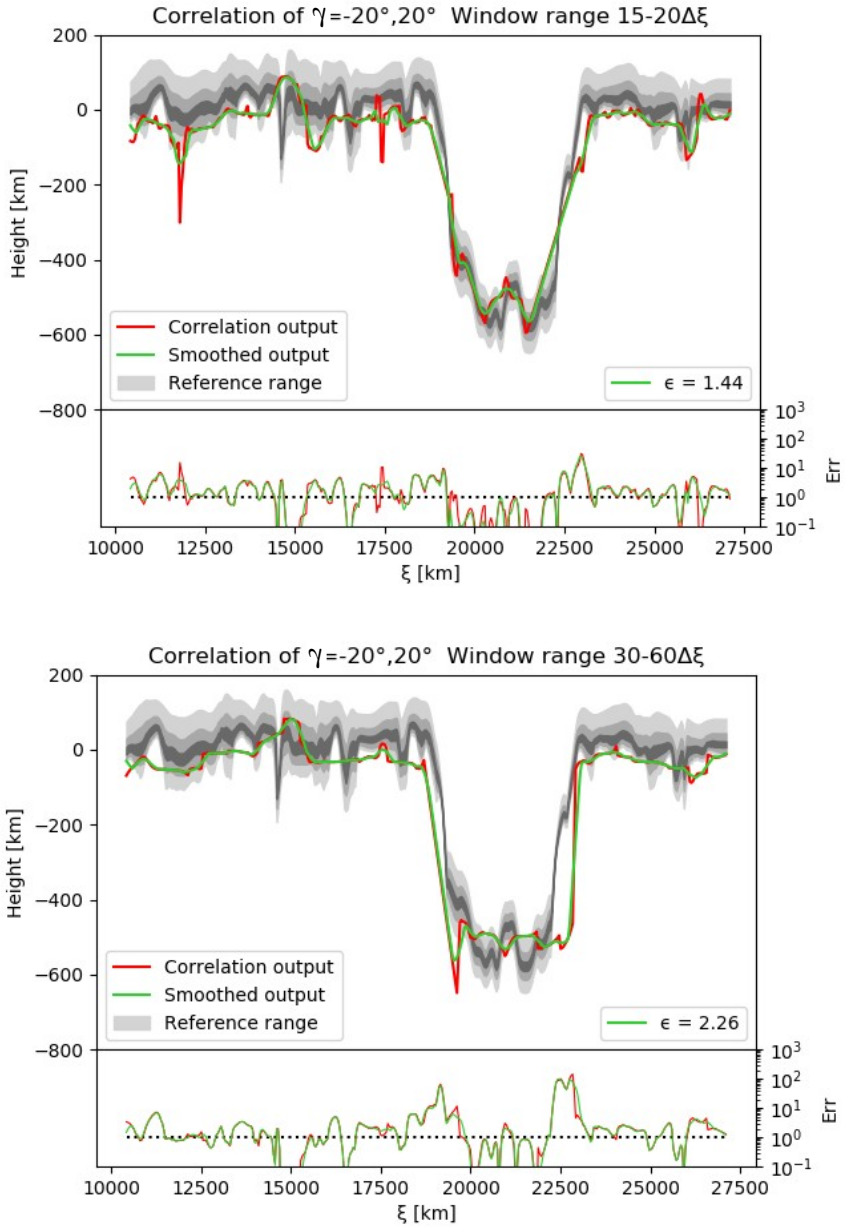

Figure 3.4: Correlation method results with a ξ_{wdth} range of 15 to 20 $\Delta\xi_{\text{or}}$ (top) and a ξ_{wdth} range of 30 to 60 $\Delta\xi_{\text{or}}$ (bottom), where $\Delta\xi_{\text{or}} = 41.7$km, for the viewing angles $\gamma = -20°$ and $\gamma = 20°$.

height, even if there is an offset present in the results, and where the estimated height has discrepancies that even after an offset correction they would be wrong.

The next parameter that was studied was the grid spacing $\Delta\xi$ at which the VIPs $\mathbf{J}_A$ and $\mathbf{J}_B$ were discretized. The standard spacing $\Delta\xi = \Delta\xi_{\text{or}}$ yielded the best result for the correlation method. Using a finer grid results in oversampling of the data, increasing the computation time and the number of outliers; and using a coarser grid yields more stable results but the spatial resolution is reduced. The effect of changing $\Delta\xi$ is discussed more in the next sections, with the tests of the optimization method.

	Grid Spacing $\Delta\xi_{or}$		Grid Spacing $2\Delta\xi_{or}$	
	ϵ	f_{cost}	ϵ	f_{cost}
Correlation	1.44	0.11	2.35	0.09
$\mu = 10^{-8}$	1.44	0.05	2.63	0.05
$\mu = 10^{-7}$	1.44	0.04	2.63	0.05
$\mu = 10^{-6}$	1.44	0.05	2.63	0.05
$\mu = 10^{-5}$	1.43	0.05	2.52	0.04
$\mu = 10^{-4}$	1.91	0.08	1.97	0.08
$\mu = 10^{-3}$	2.60	0.16	2.74	0.16
$\mu = 10^{-2}$	3.24	0.24	3.21	0.24

Table 3.1: ϵ and f_{cost} function numbers for the results of figure 3.4(a) with a ξ_{wdth} of 15 to 20 $\Delta\xi_{or}$, and their optimization using different μ values, using the standard grid spacing $\Delta\xi_{or}$ (left) and $2\Delta\xi_{or}$, for the view angles $\gamma = -20°$ and $\gamma = 20°$.

3.3.2 Test of the Optimization Method

Even though the optimization method is methodologically more consistent, it involves a non-convex optimization problem and is non-linear because the matrices that must be inverted at each iteration step depend on $\mathbf{J}_A$ and $\mathbf{J}_B$, and therefore on the $h(\xi)$ estimate at each iteration step.

The smoothed result from the correlation method (green curves in figure 3.5) are used as the initial $h(\xi)$ of the optimization iterations. The calculations were performed for different grid spacings $\Delta\xi$ and also for different values of the regularization parameter μ to test the performance of this second method.

Table 3.1 summarizes the error number ϵ and the finally reached cost function. The table shows the results for the surface grid spacing $\Delta\xi_{or}$ on the left section, while the results on the right were computed using a coarser grid size of $2\Delta\xi_{or}$. The "Correlation" row refers to the initial height $h(\xi)$ obtained from the correlation method, while the results obtained by optimization iterations with different regularization parameters are shown in the rows below. The lowest error values ϵ and cost function are underlined.

With the optimization method the cost function decreases from its initial value, obtained by the correlation method. Reducing the cost function of the profiles is the aim of the optimization method. However, the regularization parameter that yields the smallest cost function and the one that gives the smallest ϵ do not agree. For both grid spacing cases, the μ that yields the smallest ϵ, is larger than the one that yields the smallest cost function.

The reconstructed height $h(\xi)$ after the optimization for different grid spacing and μ values are shown in figure 3.5. These figures have the same format as figure 3.4 and the results were computed along the same surface profile. As in Table 3.1, the top plot shows the results for the standard grid spacing, while the bottom one shows those for the coarser grid spacing of $\Delta\xi = 2\Delta\xi_{or}$.

In both plots of figure 3.5 the curves show to the resulting height vectors using $\mu = 10^{-6}, 10^{-5}$ and 10^{-4} as the regularization parameter, plotted in red, green and blue, respectively. Figure 3.5 shows the effect that the regularization parameter has on the results: very small μ values make no significant changes on the re-

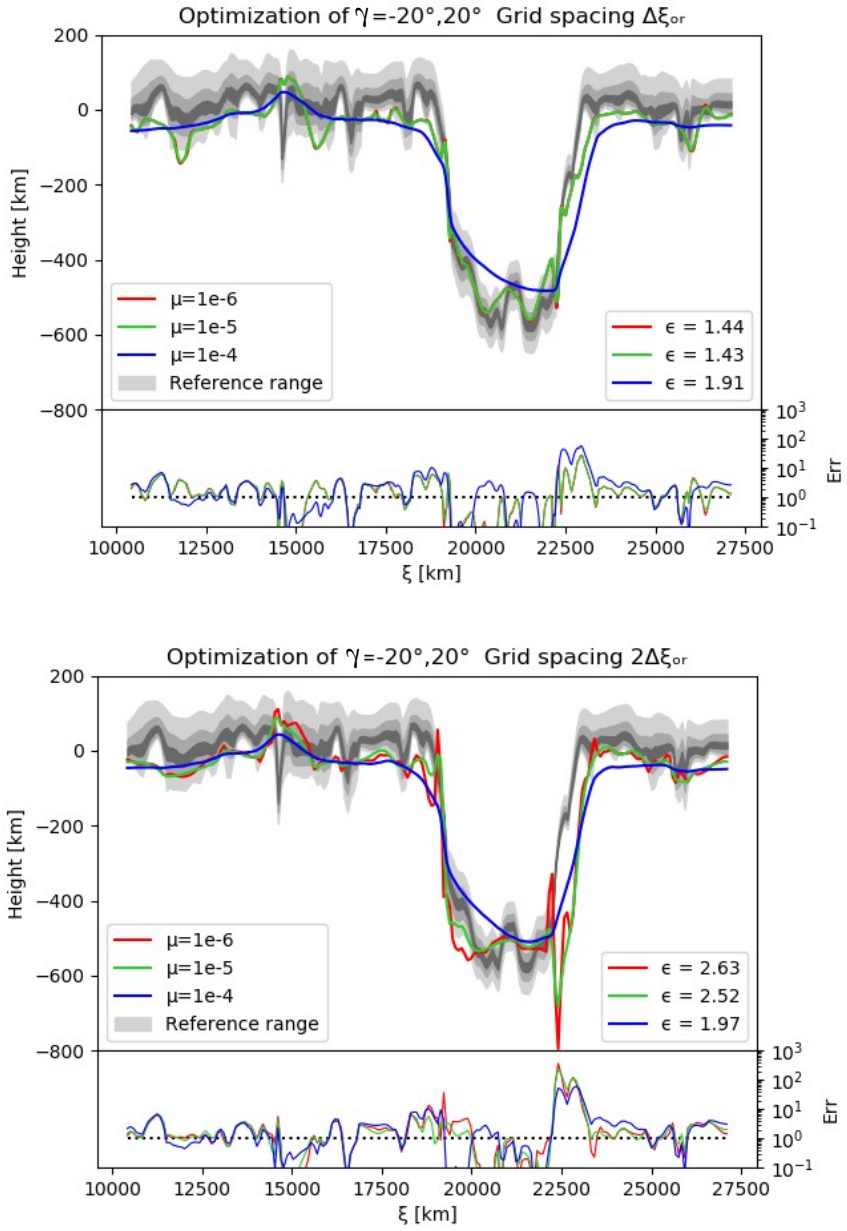

Figure 3.5: Height vector optimization results for the views of $\gamma = -20°$ and $\gamma = 20°$ with a grid spacing of $\Delta\xi_{\text{or}} = 41.7$ km (top), $2\Delta\xi_{\text{or}} = 83.4$ km (botom) and different values of μ.

constructed height $h(\xi)$ obtained first with the correlation method, while larger μ values smooth out many small-scale structures but reduce the number of outliers. A value of $\mu = 10^{-5}$ is chosen as the standard parameter for the further tests, along with the standard grid spacing $\Delta\xi_{\mathrm{or}}$, since it is a value that smooths out some of the outliers while still keeping a reasonable amount of detail in the reconstructed height.

It was mentioned already in Section 3.3.1 that a smaller cost function does not necessarily mean that the reconstructed height has a better agreement with the true height. It means that a pair of VIPs are very similar to each other. Two very similar VIPs, and therefore a small cost function, can be produced with a height vector that has a great number of outliers even if it has poor agreement with the true height. The VIPs can locally be insensitive to changes in $h(\xi)$ in regions where there is not much structure, so that the vector might have many outliers in these regions and not affect the cost function. On the other hand, a smaller μ allows to reproduce more details in the height variation. However, in the quiet Sun area, the reconstructed details do not always agree with the fine-scale height variations of the true height.

3.3.3 Test of the Effect of Viewing Angles

The parameters that yield the best results, i.e. the smallest number of outliers while displaying enough detail, are used as the standard set of parameters from now on to evaluate the effect that different viewing parameters have on the results. These parameters are the window size range ξ_{wdth} set to 15 to 20 $\Delta\xi_{\mathrm{or}}$, the surface grid spacing of $\Delta\xi = \Delta\xi_{\mathrm{or}}$, and the regularization parameter set to $\mu = 10^{-5}$. In this section the height $h(\xi)$ is reconstructed for different sets of viewing geometry in order to study the effects that the viewing geometry has on the results.

The effect that increasing observing angles has is displayed in figure 3.6. The tests for both the correlation and the optimization methods were performed with a combination of a completely vertical view at $\gamma = 0°$ and inclined views at $\gamma = -30°$ and $\gamma = 30°$. In both cases, on the respective near-sided slope of the active region there is a large disagreement between the reconstructed height and the true height. The reason for this discrepancy is the fact that the $\pm 30°$ view directions come close to the slope inclination of the respective height profile. In each image, the structures on the near-side slope appear compressed in the image and correlating them with the vertical view is likely to be less stable. This effect is consistent for both viewing directions displayed in Figure 3.6, only on opposite sides of the sunspot. Because of the large discrepancy present in both cases, the mean error of the reconstructed height vector increased to $\epsilon = 3.23$ for the viewing geometry of $\gamma = -30°$ and $0°$ (top), and $\epsilon = 2.24$ for the viewing geometry of $\gamma = 0°$ and $30°$ (bottom).

Figure 3.7 shows another example of an asymmetrical viewing configuration, where the angles are $-10°$ and $+20°$, so that the total separation between the viewing points is again $30°$, like in Fig. 3.6, but in this case none of the view directions has a view angle larger than $|\theta| = 20°$. The final reconstructed height after the optimization has a mean error of $\epsilon = 1.37$. The general agreement of the reconstructed height of Fig. 3.6 with the true height is good, even though some of the smaller scale structures have been smoothed out during the optimization.

In the two earlier cases the separation angle of the viewing points was of $30°$. Now the effect of the viewing geometry is studied by reconstructing the height for

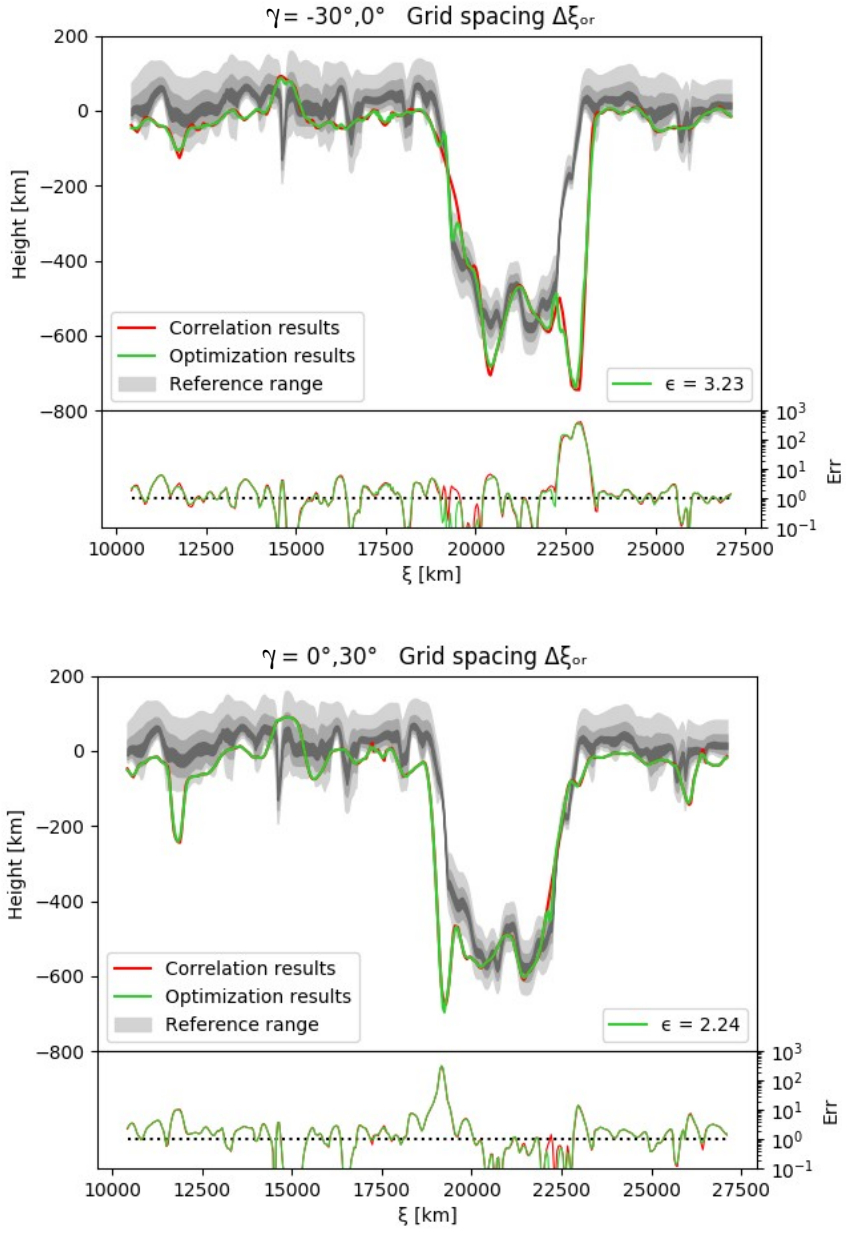

Figure 3.6: Results for the reconstructed height vector for the viewing angles of $\gamma = 0°$ and $-30°$ (top) and $\gamma = 30°$ and $0°$ (bottom), using a grid spacing of $\Delta\xi_{\text{or}} = 41.7$ km and a regularization parameter of $\mu = 10^{-5}$

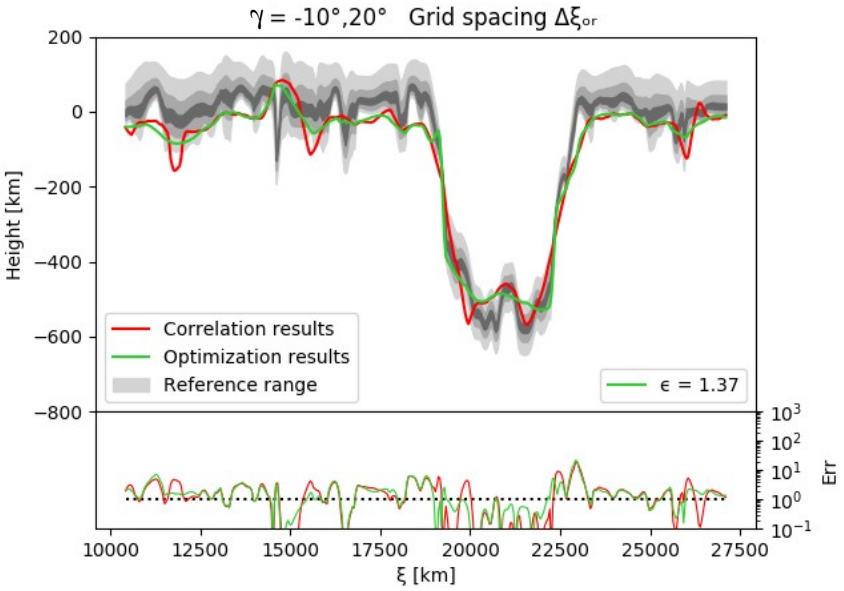

Figure 3.7: Results for the reconstructed height vector for the viewing angles of $\gamma = -10°$ and $+20°$ using a grid spacing of $\Delta\xi_{or} = 41.7$ km and a regularization parameter of $\mu = 10^{-5}$.

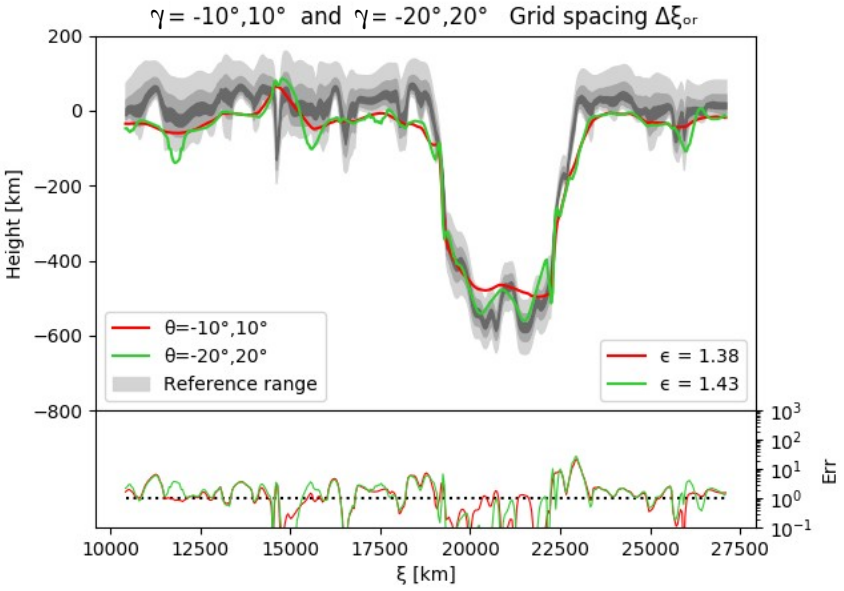

Figure 3.8: Comparison of the reconstructed height vectors for $\gamma = \mp 10°$ (red) and $\mp 20°$ (green), using a grid spacing of $\Delta\xi_{or} = 41.7$ km and a regularization parameter of $\mu = 10^{-5}$.

symmetrical view angles but with different separations of $\gamma = \mp 10°$ and $\gamma = \mp 20°$. The results are shown in figure 3.8 as the red and green curves, respectively, but only the optimization results for both view angle pairs is presented.

The results in figure 3.8 show that the reconstructed height has a better agreement if the observations are symmetric. The mean error for $\gamma = \mp 10°$ is $\epsilon = 1.38$, and for $\gamma = \mp 20°$ the error is $\epsilon = 1.43$, in both cases smaller than the error obtained in the previous two tests. The overall error is smaller for symmetrical viewing geometry than for asymmetrical viewing geometry, while the error is also smaller if the separation angle is smaller. Nevertheless, for the pixel size of the synthetic images of $dx = \Delta\xi_{\text{or}} = 41.67$ km and a given viewing angle γ the depth resolution is roughly limited to $\Delta h = dx/\sin\gamma = 122$ km for $\gamma = 20°$ and 240 km for $\gamma = 10°$.

The obtained height for $\gamma = \mp 10°$ has a good agreement with the true height, even though the height curve is very smooth, so some of the smaller scale details have been lost due to the lack of resolution and over-regularization with the chosen standard value for μ. A large μ value during the optimization may over-smooth the reconstructed height.

Comparing reconstructed height profiles for the different sets of viewing angles gives information on how the viewing geometry affects the results: the reconstructed height has a smaller ϵ if both views are symmetrical and for smaller separation angles up to $\pm 10°$. Errors might arise on the slopes of the active regions if one of the viewing angles is too large so that the view direction comes close to being parallel to the respective near-side slope. If the total separation of the viewing angles is small enough, the results from the correlation method are already reliable and the optimization does not improve the results considerably.

3.3.4 Analysis of a Second Profile of the Active Region

Another intensity profile from the same simulated active region was analyzed, this time for a different epipolar line profile in the images. This new profile has more structure inside the active region and is therefore more complicated. The height was reconstructed for the standard view geometry of $\gamma = \mp 20°$, with both the standard grid spacing $\Delta\xi$ and the coarser one. The effect of observing with asymmetrical viewing geometry of $\gamma = 0°$ and $\mp 30°$ using the standard set of parameters from Section 3.3.2 is also studied.

Like the results presented in Section 3.3.2, the reconstructed height $h(\xi)$ has a better agreement with the true height when the standard grid spacing $\Delta\xi = \Delta\xi_{\text{or}}$ was used, compared to $\Delta\xi = 2\Delta\xi_{\text{or}}$. The reconstructed height curves in figure 3.9 show the results of the correlation method in red, and the optimization method with the standard grid in green and in blue for the coarser grid spacing, both using a regularization parameter of $\mu = 10^{-5}$. The mean error for the correlation results is $\epsilon = 2.18$, and for the optimization are $\epsilon = 2.15$ for $\Delta\xi = \Delta\xi_{\text{or}}$, and $\epsilon = 2.27$ for $\Delta\xi = 2\Delta\xi_{\text{or}}$.

This profile of the active region has a structure on the left slope of the penumbra where the true height profile has a sharp peak. The analysis from $\gamma = \mp 20°$ does not reproduce this feature well, even after optimizing the height vector. However, if the viewing geometry is different it can be reproduced, as demonstrated in the left plot of figure 3.10. Both curves in figure 3.10 correspond to the reconstructed height for the vertical view of $\gamma = 0°$, and for $\gamma = -30°$ (top), and $\gamma = 30°$ (bottom). As in figure

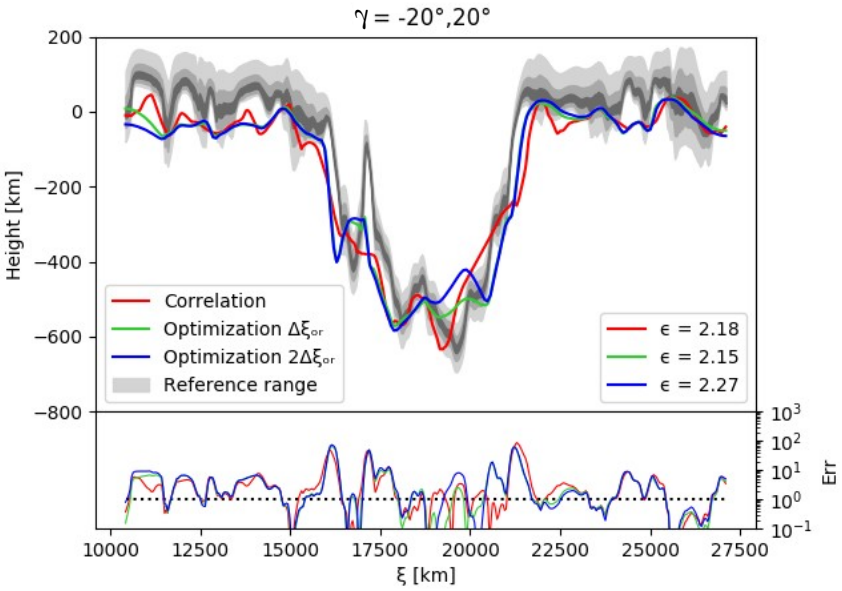

Figure 3.9: Correlation and optimization results for the reconstructed height vector for the viewing angles of $\gamma = \mp 20°$ with different grid spacings of $\Delta\xi_{\mathrm{or}} = 41.7$ km and $2\Delta\xi_{\mathrm{or}} = 83.4$ km and a regularization parameter of $\mu = 10^{-5}$

3.6, a disagreement with the true height at each near-side slope arises. Nevertheless, in the bottom plot of figure 3.10, even when there is a disagreement with the true height on the right, near-side slope due to the viewing effect previously described (figure 3.6), the local peak feature inside the active region is well reproduced, since it lies on the far-side slope. Specially after the optimization, displayed in the green curve, this feature on the left slope is very well reproduced, while the disagreement with the true height decreases considerably after the optimization. This happens in both diagrams of figure 3.10.

For the first profile, which was simpler, presented in Sections 3.3.1 and 3.3.2 the correlation results generally have a good agreement with the true height and the optimization procedure did not change or improve the agreement with the true height significantly. On this second profile, due to the complex structure previously mentioned, the correlation method does not yield by itself such good results, and the optimization makes a clear improvement here. This suggests that depending on the structure within the active regions, either the correlation or the optimization method can be chosen in order to achieve the best results. The results depend strongly on the viewing geometry and errors arise when the angle between one of the view directions and the local tangent of the surface becomes too small.

3.3.5 Testing the Effect of Noise in the Reconstructed Height

Real observations always have an amount of noise, so the performance of the method developed in this work also has to be tested with noisy images. For this the calculations were run while noise was increasingly added to continuum intensity images. To only have the noise level as a variable, the standard parameters were used for the calculation: view angles of $\gamma = \mp 20°$ and the single grid spacing. The cost function

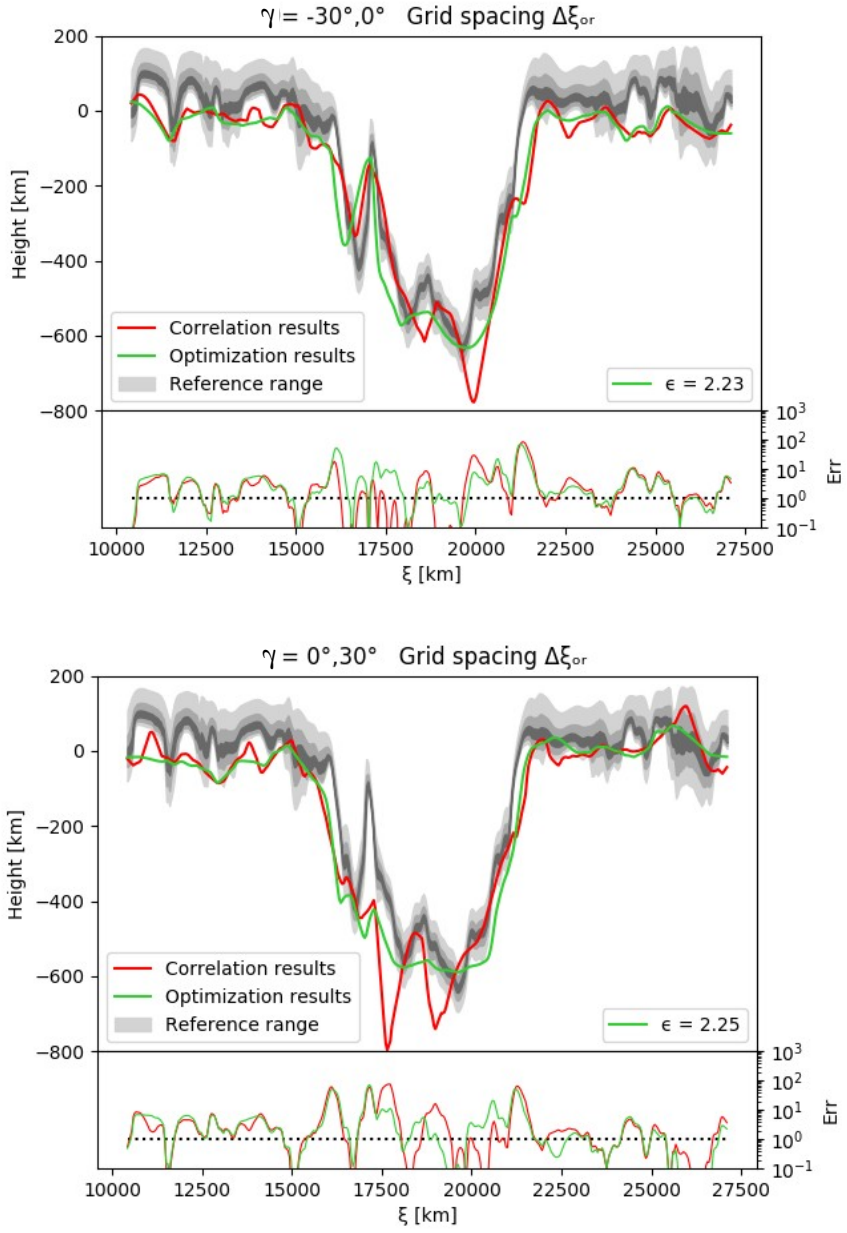

Figure 3.10: Results for the reconstructed height vector for the viewing angles of $\gamma = -30°$ and $-0°$ (top) and $\gamma = 30°$ and $0°$ (bottom), using a grid spacing of $\Delta\xi_{\text{or}} = 41.7$ km and a regularization parameter of $\mu = 10^{-5}$.

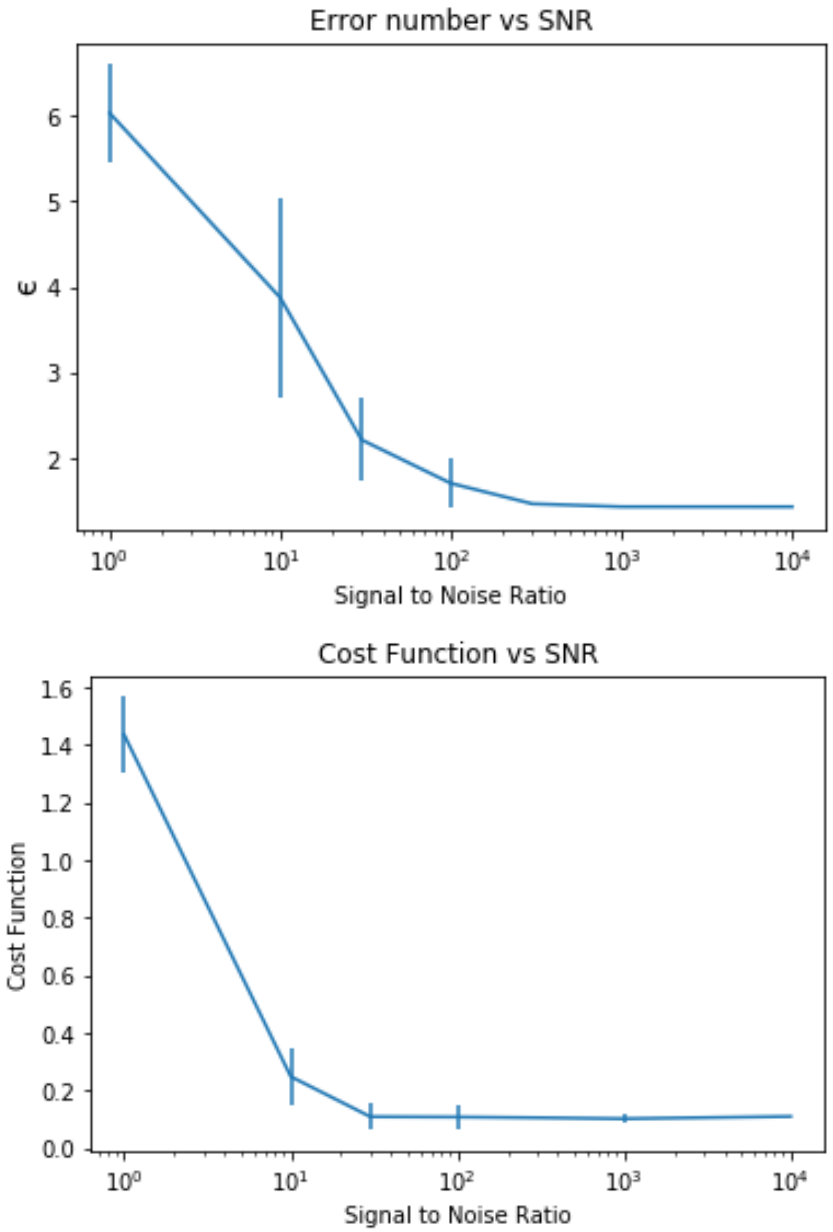

Figure 3.11: ϵ (top) and cost function f_{cost} (bottom) curves as a function of the signal to noise ratio.

and ϵ were determined for the reconstructed height obtained from images in which the noise levels were successively increased by a factor of ten. For each increase level of the image signal-to-noise ratio (SNR) the mean and standard deviation of ϵ and the cost function was determined.

In figure 3.11 the mean ϵ and cost function as functions of the SNR are displayed. The error bars for each point represent the corresponding standard deviation. As it was to be expected, the mean error and the cost function decrease with the noise level. Above SNR of about $\simeq 10^2$ the decrease is not relevant and the error and cost function result to the level that is intrinsic to the developed method. Oppositely, noise influences the height estimates significantly only for a SNR smaller than 10^2.

In figure 3.12 the results of reconstructing the height vector at some of the noise levels are displayed. The red curve corresponds to the reconstructed height for pro-

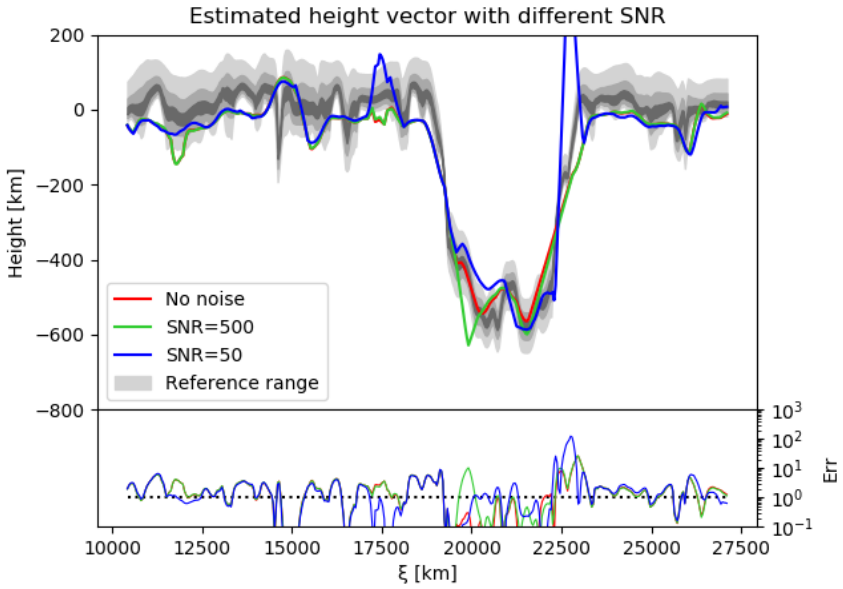

Figure 3.12: Reconstructed height vector for for the VIPS of the viewing angles of $\gamma = -20°$ and $\gamma = 20°$ with different levels of added noise.

files with no added noise. The reconstructed height of the green curve was obtained from profiles with a SNR of 500, and the blue curve from profiles with a SNR of 50. These two SNR values were presented because a SNR of 500 or higher can be expected for real observations (see Solanki et al., 2020). If the SNR is 50 the obtained results are still reliable on average, but where the slopes are steep this method may yield locally larger errors. The number of these localized errors increases with decreasing SNR.

3.3.6 Full 2D Height Maps

In the earlier sections of this chapter only the results for single individual profiles across the active region were displayed. If adjacent epipolar lines in the y direction are successively processed and then the reconstructed 2D profiles are stacked , full 2D surface areas can be scanned in order to obtain 2D maps of the reconstructed height.

For the production of these maps the selected parameters are the same throughout all the successive epipolar lines, and each profile is calculated individually. The selected parameters for this task were the standard parameters: viewing angles of $\gamma = \mp 20°$, a surface grid size of $\Delta\xi = \Delta\xi_{\text{or}}$, a window size range of $\xi_{\text{wdth}} = 15$ to $20\,\Delta\xi$ for the correlation, and a regularization parameter of $\mu = 10^{-5}$ for the optimization method. Just like in the previous sections, an initial reconstructed height $h(\xi)$ was obtained from the correlation method, then smoothed and used as the initial vector for the optimization. Therefore each horizontal line in the 2D height maps is the reconstructed height of the respective profiles after the optimization. No smoothing was applied in the y-direction.

To visualize the effect that different image resolution has on the results, the horizontal (x direction) resolution of the images was successively degraded by a factor

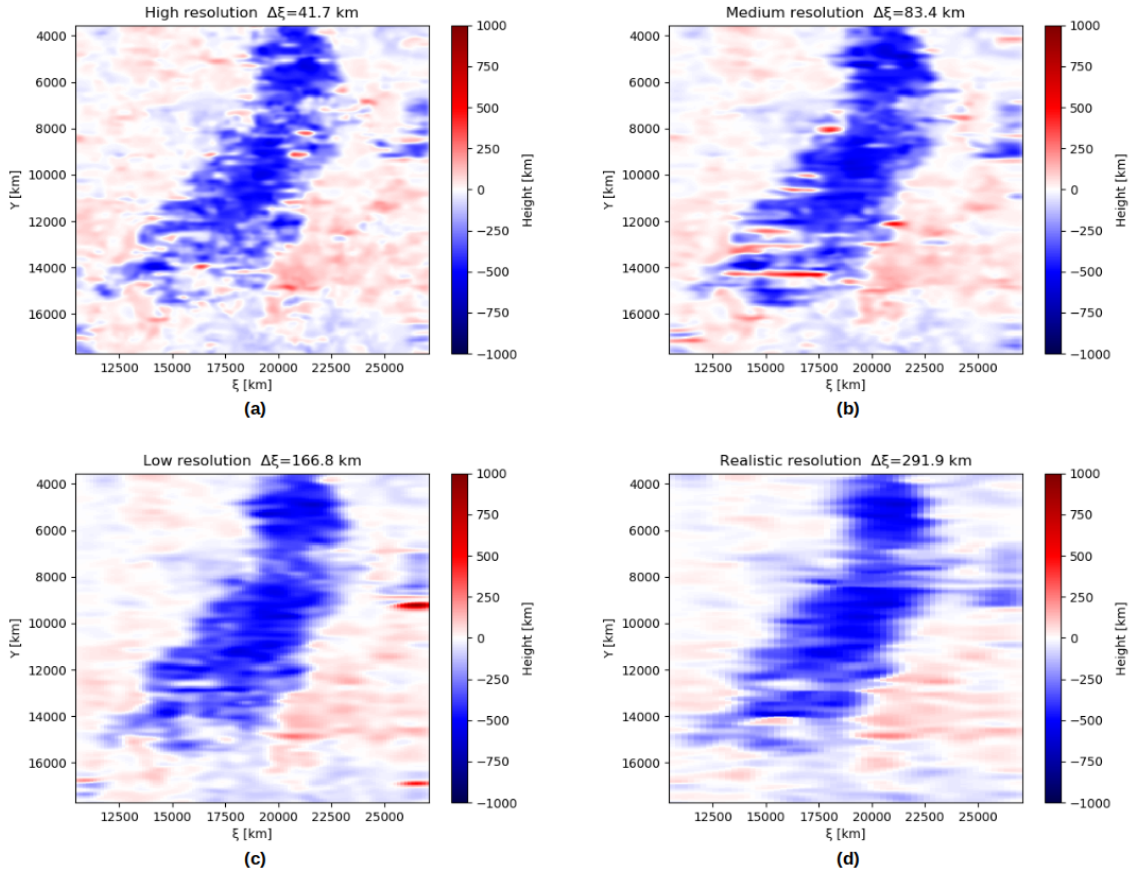

Figure 3.13: 2D height maps obtained from the successive reconstruction of epipolar profiles using image pairs with view direction $\gamma = -20°$ and $\gamma = 20°$. Increasing image pixel sizes of 41.7 km, 83.4 km, 166.8 km, and 291.9 km in the x-direction in figure (a), (b), (c), and (d), respectively, have been used. In the y-direction the pixel size is always 41.7 km.

2 each time, producing four different image sets with image pixel sizes $dx = \Delta\xi_{\text{or}} = 41.7$ km, 83.4 km, 166.8 km, and 291.9 km, so that a different resolution was used for each 2D height map. The pixel size in y was not degraded, and the resolution was kept the same for both views in each map. The resulting 2D height maps are shown in figure 3.13(a), (b), (c), and (d).

The trade-off between resolution and quality is clearly shown in the height maps in figure 3.13. Again, to assess the quality of the results, they are compared with the true height map, obtained from the barycenter height of the response function $R_T(\xi, z)$ for the vertical view direction of $\gamma = 0°$. The reference height map was computed directly from the MHD simulation, and is presented in figure 3.14. The maps obtained from the comparison of images with higher spatial resolution show more visible errors, which appear as bright red or dark blue regions. On the other hand, the lower resolution maps show fewer errors, but many of the smaller scale structures, especially the structures inside the pore are not reproduced. The resolution of figure 3.13 (d) is comparable to the best resolution that real images, obtained from observations of SO/PHI and another spacecraft, e.g. SDO/HMI, at a distance of roughly 1 AU, will have.

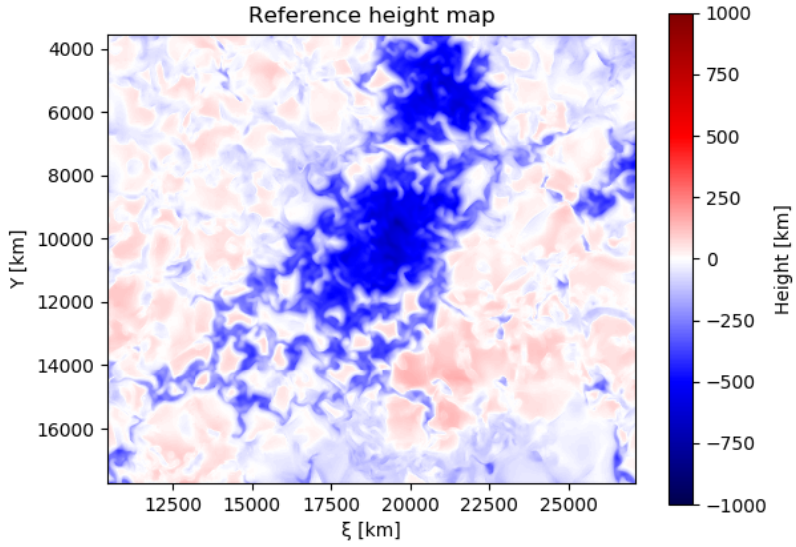

Figure 3.14: True height map obtained from the average of the heights associated to the response function $R_T(\xi, z)$ (see Eq. 3.3 within a range of $R/R_{max} \simeq 0.5$ of the full resolution synthetic data.

Another remark is that in figure 3.13 the resolution was degraded only in the horizontal direction of the images. All images are vertically composed of 340 reconstructed height vectors with a resolution on the vertical direction of $\Delta\xi_{\text{or}} = 41.7$ km.

3.3.7 Estimating a Height Vector for Two Views With Different Resolution

The last tests conducted with the test data aimed to evaluate the results obtained if the image resolution is different for both views. Real photospheric observations for stereoscopy use combined data, in the case of this work obtained by SO/PHI with SDO/HMI, so it is to be expected that both of the images that will be used to estimate the photospheric height variations with this stereoscopic method will have different resolutions. The synthetic images from both views were degraded to different and realistic resolutions for this test.

The respective results for the reconstructed height along the epipolar profile used in Sections 3.3.1, 3.3.2 and 3.3.3 is displayed in figure 3.15. The view directions were $\gamma = -20°$ for the higher resolution image, with a horizontal resolution of 166.7 km and $\gamma = 20°$ for the lower resolution image with a horizontal resolution of 291.9 km. The height was reconstructed, for this pair of images, first using a surface grid spacing of $\Delta\xi = 4\Delta\xi_{\text{or}} = 166.7$ km (top diagram), and then of $\Delta\xi = 7\Delta\xi_{\text{or}} = 291.9$ km (bottom diagram). The parameters used were the same as in the previous section.

The surface grid $\Delta\xi$ had the same spacing for either of the intensity profiles. The left diagram in figure 3.15 displays the reconstructed height obtained by mapping both images to the higher surface resolution grid, and therefore increasing the size of the low resolution image. The error number in this case was of $\epsilon = 4.59$. The right

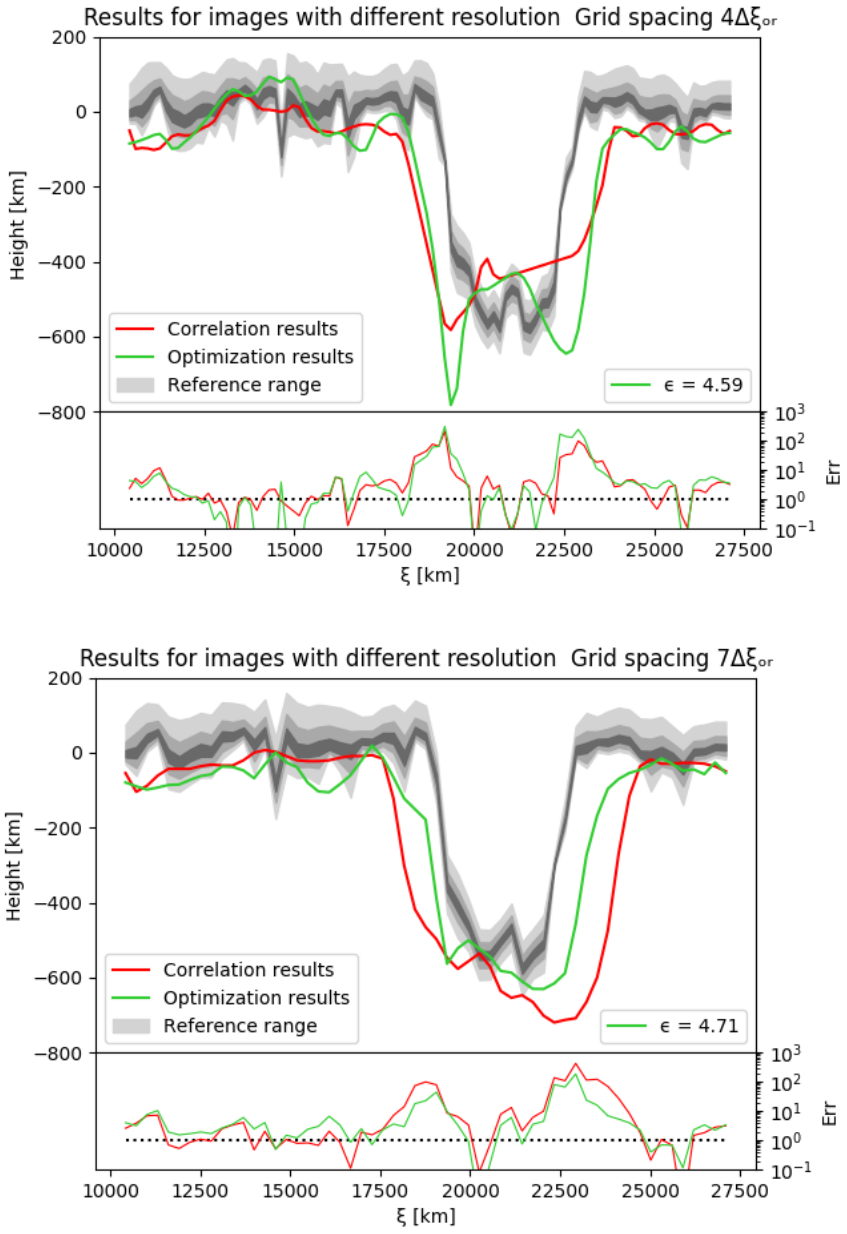

Figure 3.15: Reconstructed height vector from optimization method applied to images with different pixel resolution. The $\gamma = -20°$ view has a a pixel size of 166.8 km while the view of $\gamma = 20°$ has one of 291.9 km. The spacing of the surface grid is $\Delta\xi = 166.7$ km (top) and $\Delta\xi = 291.9$ km (bottom).

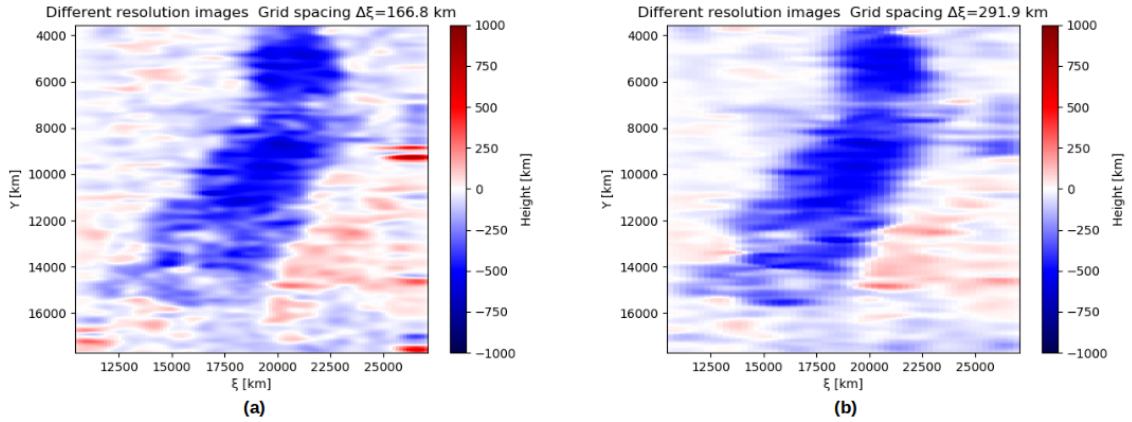

Figure 3.16: 2D height map calculated for the viewing angles of $\gamma = -20°$ with a pixel size of 166.8 km and $\gamma = 20°$ with 291.9 km. The grid spacing in (a) is of $\Delta\xi = 4\Delta\xi_{\text{or}} = 166.7km$, and for (b) it is $\Delta\xi = 7\Delta\xi_{\text{or}} = 291.7km$.

diagram displays the reconstructed height when both images were mapped to the lower surface resolution grid, so that the size and resolution of the higher resolution image profile were degraded. The error number here was slightly increased, being $\epsilon = 4.71$. These results show that the resolution of the lower resolution image limits the quality of the reconstructed height.

Both reconstructed height vectors have higher error numbers than the results of the previous sections of this chapter due to the larger pixel sizes used here. This implies that the resolution of the data limits the quality that can be achieved in the reconstructed height, and additionally, the lower resolution image plays a determining role in the quality or resolution that can be achieved in the results. The error is roughly tripled, in comparison to the standard case in the left diagram of figure 3.5, while the pixel sizes used in this section where larger by a factor 4 and 7. Comparing them to the earlier results of this chapter, the depth of the sunspot is still relatively well reproduced, but the depression is estimated to be have a much larger size than has, so that the depression of the solar surface is estimated to cover a larger area as well.

To finish the analysis of the performance of this method with the test data, the 2D height maps for the results from different resolution images are shown in figure 3.16. The geometry and resolution is the same as for the single profile test of figure 3.15, but for these maps the heights obtained over the whole image are presented. The resolution of both images is very low, which limits the amount of detail that can be reconstructed. However, very few outliers are present in these results. This is another example of the trade-off between quality and resolution that is always present in the results of this chapter.

3.4 Summary and Discussion

The tests conducted with the synthetic MHD data of the performance of the method show that the stereoscopic method developed in this work allows to estimate height variations on the solar surface from the observations obtained from two different

viewing points. The Wilson depression of the simulated active region was of around 600 km, and the reconstructed height profiles agree with this quantity.

With the synthetic data, the Wilson depression can be estimated with good precision, and even some of the structures within sunspots or large pores can be reproduced if the observing conditions are adequate. Of course, the test data used in this chapter represents a very simplified test case, but by running the tests here provided, a good idea of how this method will perform when applied to real observations can be obtained.

The results yielded by the stereoscopy method are robust for viewing points with a separation ranging from $10°$ to $40°$, approximately. If the separation angle is smaller than $10°$, the geometrical resolution error of the height vector should theoretically increase as $1/\sin(|\gamma_A - \gamma_B|/2)$. If the separation angle is larger, it eventually leads to problems if one of the viewing direction tangentially approaches the slope at the edges of the sunspot.

The method also produces stable results when applied to images that were contaminated by a limited amount of noise. The Wilson depression could be reproduced for all the intensity profiles with SNR ≤ 50. For larger levels of noise, the precision with which smaller scale structures are reproduced decreases, and only larger scale structures are reproduced.

A big advantage that this stereoscopic method has is that it requires only two surface images as input to perform the calculations to obtain height variation estimates. Previous methods required a series of assumptions to indirectly estimate the Wilson depression (see, for example Löptien et al., 2020). For our method only the two intensity profiles taken from two different vantage points in the same spectral window is needed.

The biggest limiting factor for the performance of our method is the spatial resolution of the images. The higher the image resolution, the smaller are the structures that can be reproduced. The theoretical height resolution (see Eq. 2.15) for the synthetic images under the standard viewing geometry is of 60 km, and at any given point the height estimate has an error of $\bar{h}_{th} \approx \pm 30$ km, so any given fluctuations smaller than that are uncertain and and may be produced by our method due to the limited resolution of the image data. For the resolution of the synthetic images employed in this paper, the Wilson depression and even some of the finer structure within, or in the quiet Sun can be reproduced. However, it is to be expected that when applying the method to real observations, only the Wilson depression can be estimated, because of the limiting resolution that the real data will have.

Another factor that sets a limit on the resolution is the finite thickness of the photospheric opacity layer. A fundamental assumption of out method is the assumption that this layer is infinitely thin so that it can be characterized by a single height $h(\xi)$, instead of by a height distribution (see Eq. 1.7). For real observations the height distribution barycenter varies with the view angle, so that the height $h(\xi)$ obtained can only be approximate. The formation of the observed radiation is shifted further to higher altitudes, the larger the angle between view direction and surface normal.

In some cases (see Table 3.1, figure 3.6 left), the agreement between the calculated height and the true height is not improved by the optimization method, as compared to the correlation results. This happens because the optimization improves the cost function and not necessarily the error number ϵ. The optimization

procedure deals with small scale differences between the two intensity profiles by producing a height vector that yields similar mapped VIPs from both views, even if this does not necessarily produce a better agreement with the true height.

The main systematic discrepancy is a small offset between the calculated height and the reference height. This offset appears through the entire epipolar profile, but changes for different viewing conditions. This could be due to differences in the formation height (Carlsson et al., 2004) of the observed radiation. In these tests all the height variations were compared with the true height obtained only for the vertical view. Throughout all the results, regardless of the offset, the quiet Sun height estimates systematically fall below the true height; while the estimated depth of the umbra agrees much better with it. This offset at the quiet Sun might be produced by asymmetries in the $\tau = 1$ layer by observing the photosphere from an inclined viewing point. These asymmetries may result in a shift of the quiet-Sun features and therefore an artificial disparity, interpreted as a vertical offset by the correlation algorithm. For this reason it is to be expected that the estimates of the Wilson Depression, derived from the height difference between the quiet Sun and the umbra, are a few tens of kilometers smaller than in the reference data. The reason that our estimate of the Wilson depression is slightly smaller might be a combined effect of the averaging of the depth profile within the correlation window, the flattening of the $\tau = 1$ layer that appears when observing the photosphere from an inclined viewpoint, and the asymmetry of the observations from different directions, which could increase the disparity of the structures on the quiet Sun. When using real data, a margin of error of this order can be expected, as well as an offset in the results.

The main aim of the method presented in this work is to apply it to real observations in order to produce real estimates of the Wilson depression. Real observations have different levels of resolution, noise distortion, and projection. In order to apply this method to real observed images, some pre-processing will be needed so that two images taken from arbitrary positions appear similar to the test data used in this chapter. In the next chapter, these necessary pre-processing steps are explained.

Chapter 4

Application of the Method to Real Data

In this chapter results from applying the correlation method to real observations are reported. The content of this chapter is as follows. In the first section the observations are presented and a brief overview of the detectors with which the observations were made is given. An example of the transformation of pixel coordinates into homogeneous coordinates is given and an example of the rectification of the images is presented as well. For rectifying the images the WCS header entries of the observations need to be corrected, so that a next section in this chapter shows a brief algorithm for this. Lastly, the results of applying the correlation method to the real data are presented and the performance of the method is discussed. Different from Chapter 3, the optimization method was not applied to the real observations, since the correlation method gave results that are reliable enough, and not significantly improved by the optimization.

4.1 Observations From SO/PHI and SDO/HMI: Some Information on the Instruments and Their Images

In this work we combine observations from the Polarimetric Helioseismic Imager on board the Solar Orbiter spacecraft (SO/PHI) and the Helioseismic and Magnetic Imager on board the Solar Dynamics Observatory (SDO/HMI).

Solar Orbiter (SO) (Müller et al., 2020) is a joint mission of ESA and NASA dedicated to solar and heliospheric physics, launched on February 10th, 2020. It has 10 instruments on board, SO/PHI being one of them. SO/PHI (Solanki et al., 2020) is a diffraction limited, wavelength tunable, quasi-monochromatic, polarisation sensitive imager. The instrument provides maps of the magnetic field vector and of the line-of-sight (LOS) velocity in the solar photosphere as well as the continuum intensity around 6173 Å in an Fe I line. It probes the deepest layers of the solar atmosphere among all the instruments on Solar Orbiter. It is composed of two telescopes: the High Resolution Telescope (HRT) and the Full Disk Telescope (FDT). All the images from SO/PHI used in this work are HRT images. HRT has an aperture diameter of 140 mm,and observes only a fraction of the solar disk at a resolution of up to 200 km at perihelion. For more information on SO/PHI see Gandorfer et al. (2011), Solanki et al. (2015), and Gandorfer et al. (2018).

The Solar Dynamics Observatory (SDO) is the first mission launched as part of NASA's Living With a Star (LWS) Program, aimed to understand the solar variability

and its causes and impacts on Earth. SDO studies the solar atmosphere in many wavelengths simultaneously in order to help understand the influence of the Sun on the Earth and near-Earth space. On board SDO are three instruments, one of them being SDO/HMI.

SDO/HMI is an instrument designed to study the oscillations and magnetic field in the photosphere. It observes the full solar disk at 6173 Å, observing the same Fe I line as SO/PHI, with a resolution of 1 arcsecond. Both instruments provide dopplergrams, continuum filtergrams, and both line-of-sight and vector magnetograms. For more information on SDO/HMI see Scherrer et al. (2012) and Schou et al. (2012).

In this work only continuum observations from both instruments are used. The signal to noise ratio (SNR) of the continuum observations of SO/PHI and SDO/HMI for the quiet Sun is of around 15000 and 10000, respectively , with a decrease to around 4000 in the umbra due to the decreased intensity in the umbra. There are combined observations from SO/PHI and SDO/HMI from multiple dates, those on March 3rd, March 17th and October 29th of 2022 are used in this work. Even though the correlation method is only applied to the observations of the last date, images of the first two dates will also be presented, mainly to illustrate how rectification works, the issues that arose while rectifying the images, and how they were solved.

Figure 4.1 displays continuum observations of the solar photosphere on March 3rd of 2022 at 09:45 UT. The time mentioned in this chapter ia the time on Earth, but the corresponding time adjustment is made for the corresponding observations of SO/PHI and SDO/HMI, considering the light travel time. Since the SO/PHI observations are performed with the High Resolution Telescope, and the SDO/HMI ones are performed with a full disk telescope, the FOV of both spacecraft is very different. For these observations, the resolution of the SO/PHI images is 198 km per pixel, and that of SDO/HMI 366 km per pixel. For this reason only a part of the FOV of SDO/HMI centered on the sunspot group is displayed in the next figures. At the time of the observations, SDO/HMI was the spacecraft ahead, and SO/PHI was the spacecraft behind. The position of the spacecraft in HEEQ coordinates is $[1.47 \times 10^8,\ 1.25 \times 10^5,\ -1.87 \times 10^7]$km, and $[8.11 \times 10^7,\ -8.60 \times 10^{\cdot}\ -5.91 \times 10^6]$km, respectively. Their respective distances from the Sun center were approximately 1 and 0.55 AU, with a separation of approximately 7° between both spacecraft.

After setting the intrinsic parameters for both spacecraft, it is possible to visualize the observations in normalized coordinates, instead of pixel coordinates (see Chapter 1.2.1). The observations from figure 4.1 displayed in normalized coordinates are shown in figure 4.2. The obvious difference between the images is a manifestation of their different extrinsic matrix parameters.

As has been previously described, the stereoscopic analysis has to be performed on the rectified observations. In figure 4.3 we show the positions of both spacecraft with respect to the Sun and the position of the central epipolar plane. This is required for rectifying the images and transforming the problem to a common coordinate system particular to the spacecraft configuration at the time of these observations. The images are rectified such that the rectified view direction of both spacecraft are parallel and in the epipolar plane with the label $\zeta = 0$ (see Eq. 1.58).

In figure 4.3 it is seen that the epipolar plane is oblique to the heliospheric equator. The rectified images are therefore rotated from the HEEQ axis frame. The rectified images are shown in figure 4.4, and not only are they obliquely reprojected, but it can also be seen that the sunspot in the images has now the same orientation,

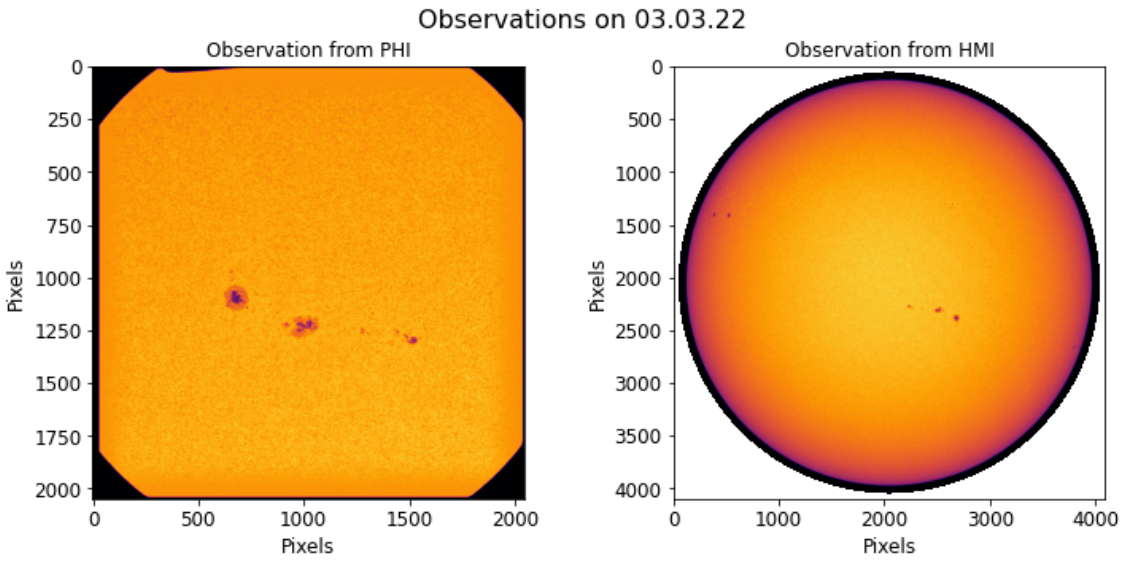

Figure 4.1: Continuum intensity observations from SDO/HMI and SO/PHI on March 3rd of 2022 displayed in pixel coordinates.

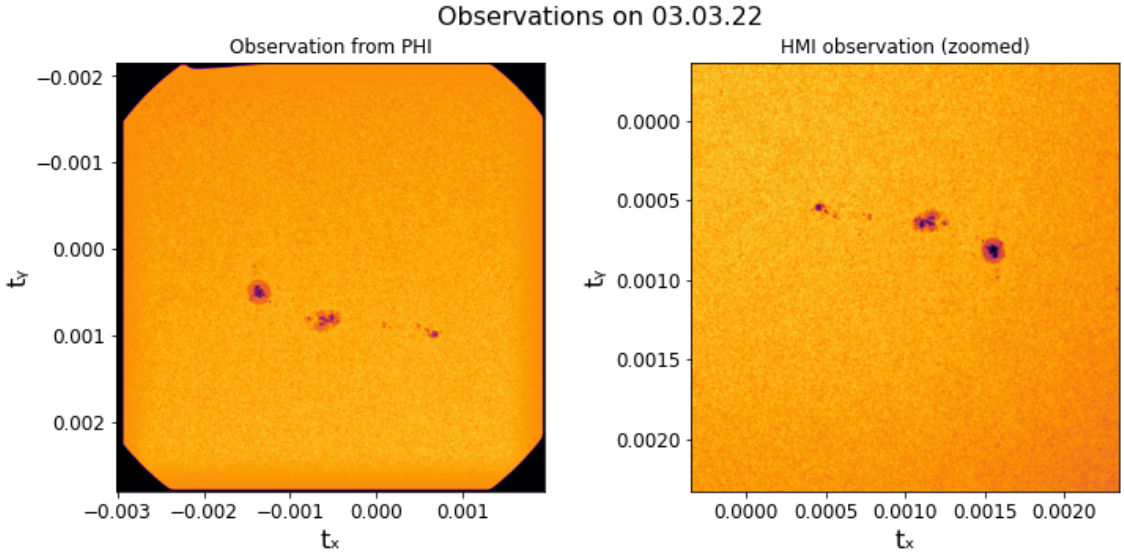

Figure 4.2: Continuum intensity observations from SDO/HMI and SO/PHI on March 3rd of 2022 displayed in homogeneous coordinates.

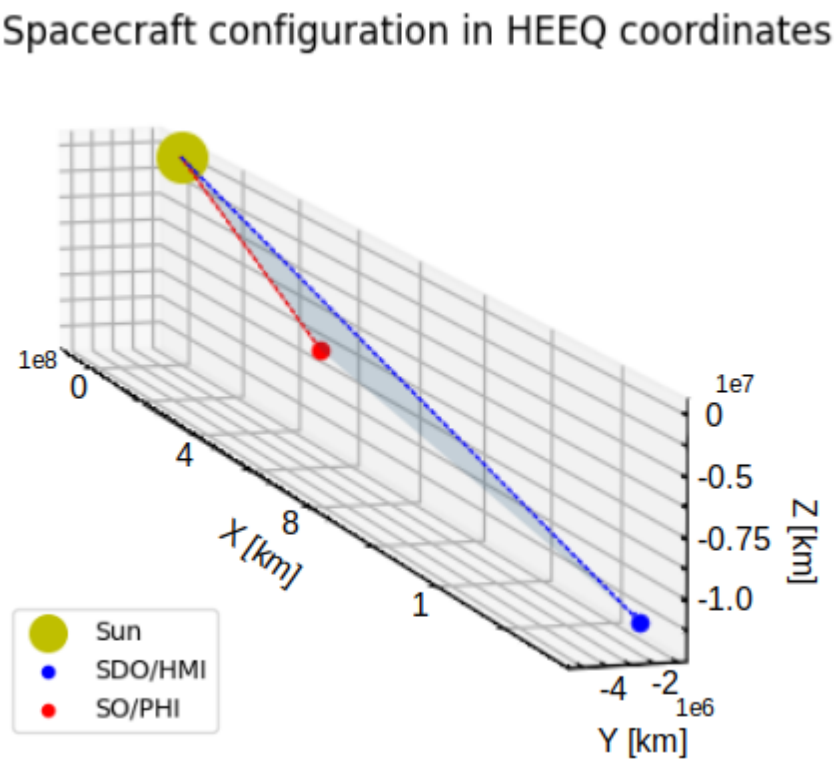

Figure 4.3: Configuration in HEEQ coordinates of the position of both spacecraft on March 3rd of 2022. The shadowed plane formed by both spacecraft and the Sun center is the central epipolar plane with the label $\zeta = 0$ and to which the observations are rectified.

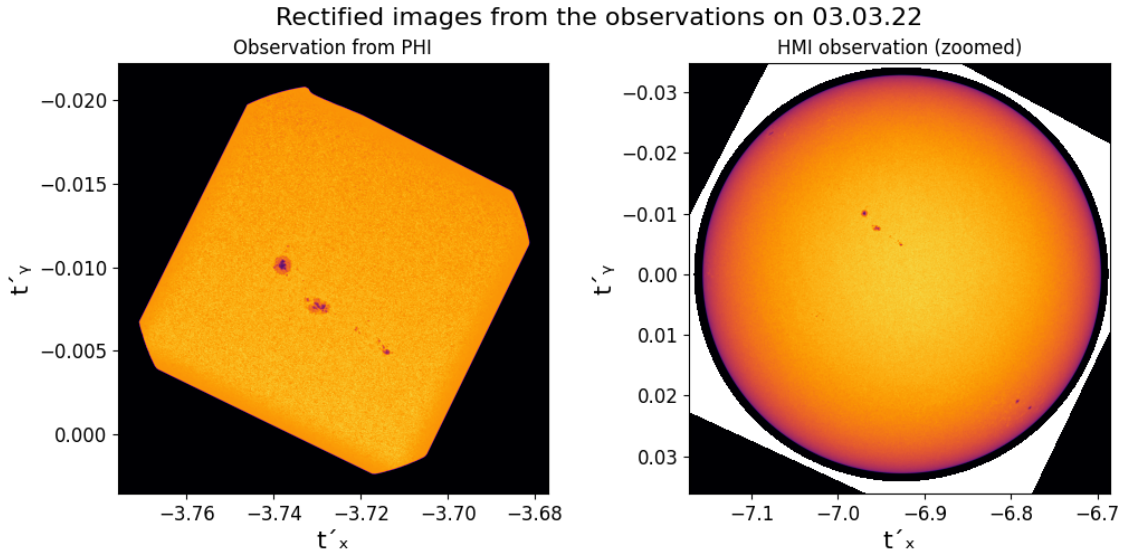

Figure 4.4: Continuum intensity observations from SDO/HMI and SO/PHI on March 3rd of 2022 after rectification.

and differences in projection should now only arise in the horizontal direction t_x in both images.

Upon further inspection of the rectified images it was seen that corresponding features were not exactly aligned in both images. The position in the t'_y direction of a feature should be the same in both rectified images, but after zooming into these images one can compare the features that appear at a given t'_y. It becomes evident that the rectification process did not provide perfect alignment. Figure 4.5 shows this: both images are zoomed in to display only the sunspot and its near surroundings. A dashed line is plotted on top of both images at the same position $t'_y = 0.01$. If the rectification was correct, the dashed line would intersect the sunspot at the same place, which is not the case.

The most probable reason for this error in the rectification is that the WCS header entries of the SO/PHI images are still inaccurate because the pointing of the SO spacecraft, and therefore of SO/PHI and SO/PHI-HRT, is known only with limited precision. While this thesis was written, the SO/PHI team was still working on determining the correct header values and also removing a small image distortion. The header entries which are probably inaccurate and induce errors in the rectification are `CRPIX1` `CRPIX2`, and `CRVAL` (see Table 1.1). These header quantities are needed to determine the cameras' intrinsic and extrinsic matrices, so errors in these quantities end up as errors in the rectification.

The quantities in the header of the SO/PHI image were corrected using an iterative approach that is explained in detail in Section 4.1.1 of this chapter. After correcting the WCS header entries and determining the intrinsic and extrinsic parameters, and rectifying the images to this new corrected frame, the features in both images have now the same t'_y, as shown in figure 4.6 .

A similar case is presented for combined observations on March 17th, 2022. In this case SO/PHI was the spacecraft ahead, and SDO/HMI behind, with HEEQ coordinates of $[5.05\times10^7,\ 2.52\times10^7,\ -3.73\times10^6]$ km and $[1.48\times10^8,\ 3.58\times10^7,\ 2.50\times10^6]$

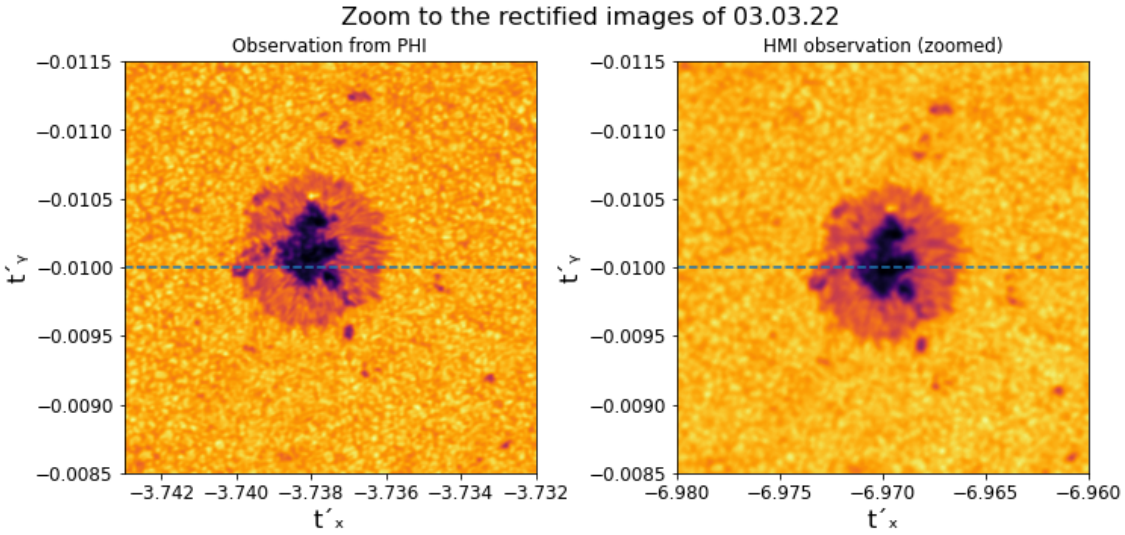

Figure 4.5: Closeup to the rectified continuum intensity observations from SDO/HMI and SO/PHI on March 3rd of 2022 displayed in rectified homogeneous coordinates.

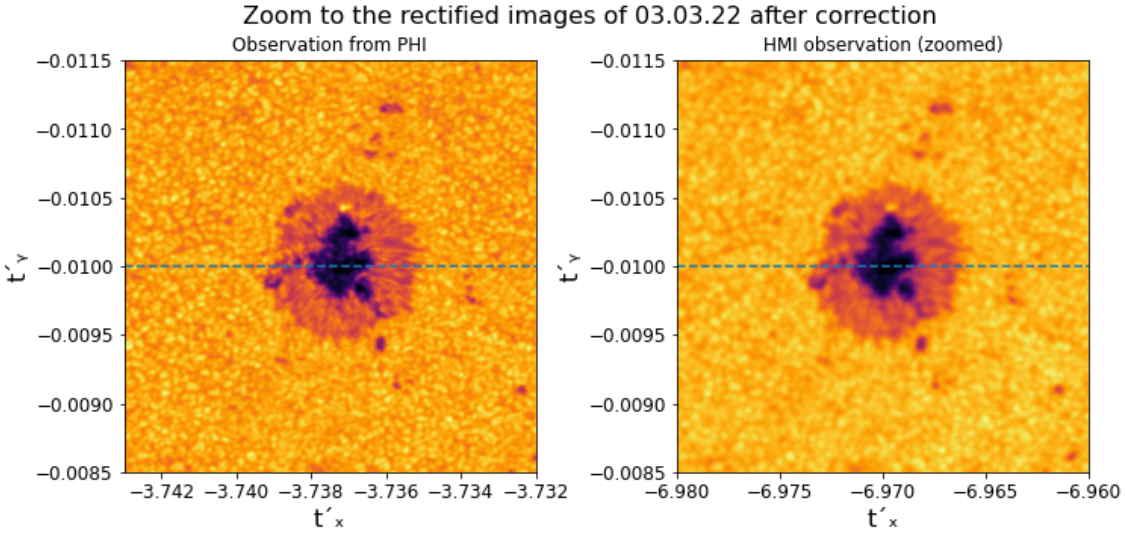

Figure 4.6: Closeup to the rectified continuum intensity observations from SDO/HMI and SO/PHI on March 3rd of 2022 displayed in rectified homogeneous coordinates after the WCS correction.

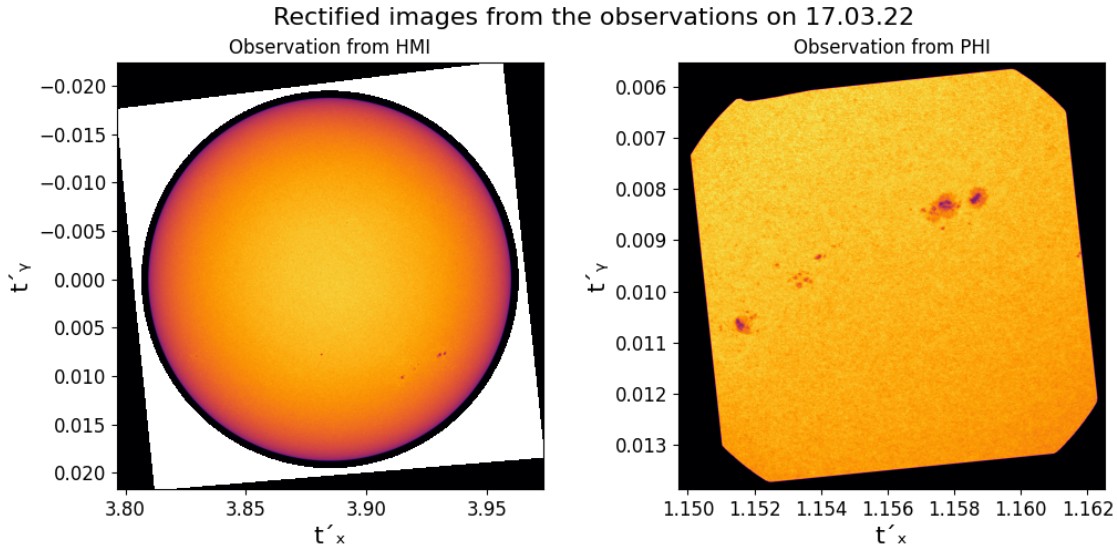

Figure 4.7: Continuum intensity observations from SO/PHI and SDO/HMI on March 17th of 2022 after rectification.

km, respectively, or approximately 0.38 and 1 AU. The separation angle between both spacecraft was $26°$.

Figure 4.7 displays the full rectified images of the above mentioned observations. In figure 4.8 a close up to the sunspot in both rectified images is presented. Here, a dashed line is again plotted on a given t'_y coordinate in both images, to show that even after rectification, corresponding structures do not have the same vertical coordinate. This is again due to inaccuracies in the WCS header entries. This case is more dramatic than the one presented in figure 4.5. Here, the positioning is very different and the dashed line goes through completely different regions in the image, and the overall field of view in the close ups is different.

Figure 4.9 displays the rectified images after correcting the header entries of the SO/PHI image. Now the dashed line is intersecting the sunspot in the same part and coordinate in both images. The projection in the images is different, because the sunspot in the observations from SDO/HMI appears close to the limb, so there is a foreshortening effect in the horizontal direction. This effect is to be expected and, does not mean that the rectification is wrong, as long as the corresponding features are vertically aligned in the rectified images.

After the correction of the header entries has been applied, the rectified images are suitable for the stereoscopic analysis. This correction has to be applied to each set of observations, since the inaccuracies in the SO/PHI header entries are not constant throughout different observations. The next steps for the stereoscopic analysis are, as described in Chapter 2, to map a surface grid onto the rectified images, to produce the corresponding VIPs by integrating the pixel intensities within each grid cell, and finally applying the correlation method to them to find the changes in height for the corresponding epipolar profile.

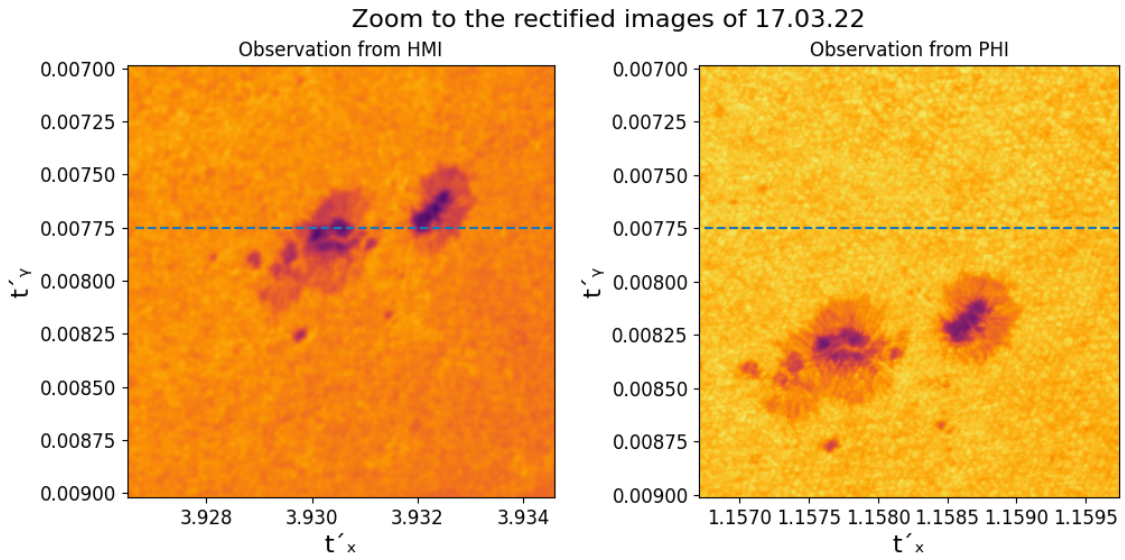

Figure 4.8: Closeup to the rectified continuum intensity observations from SO/PHI and SDO/HMI on March 17TH of 2022 displayed in rectified homogeneous coordinates.

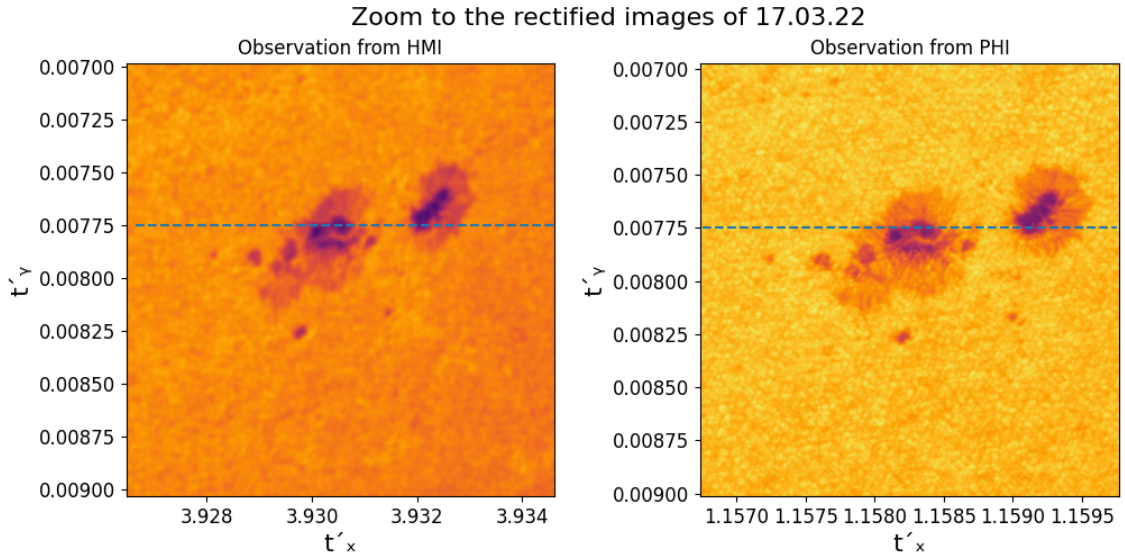

Figure 4.9: Closeup to the rectified continuum intensity observations from SO/PHI and SDO/HMI on March 17TH of 2022 after the WCS header entries correction.

4.1.1 Correction of the WCS Parameters for SO/PHI Data

A continuous problem of high resolution imaging of the solar surface is that there is not enough context available needed to accurately determine the camera's view direction and roll angle information. In order to compare observations from a high resolution camera with observations taken independently from another spacecraft or telescope, this information is necessary, and the higher the resolution of the image, the more accurate the information of the camera must be.

In this section we describe our procedure to correct the FITS header in more detail. The goal is to bring the SO/PHI-HRT image to the best agreement with reference images of another spacecraft, in this case SDO/HMI. This approach uses a transformation to move two or more well identified objects in the reference image from SDO/HMI to their correct position. This transformation yields the parameters by which the FITS header of the SO/PHI image has to be modified.

With the stereoscopic camera calibration we reverse the mapping problem. This calibration requires a set of known and well identified points. we assume that these points on the solar surface, called trigonometric points here, have known 3D positions, obtained from the SDO/HMI images.

Assuming that the position of the spacecraft is well known, the only parameters that are considered uncertain and to be corrected are the attitude parameters `CROTA`, i.e. `PC`, and `CRPIX1`, `CRPIX2` from the SO/PHI observations. This situation is often encountered in solar imaging where the spacecraft position is well known from orbit predictions with a precision of a few meters, while the spacecraft attitude is not.

We use at least two (but more can be used in this calibration) trigonometric points $\mathbf{r}_i$, and their corresponding observed pixel coordinates $(p_{x,i}, p_{y,i})_{obs}$ to correct the attitude parameters in $\mathbf{K}$ and $\mathbf{R}$, so that their mapped pixel coordinates $(p_{x,i}, p_{y,i})_{map}$ agree with the observed pixel coordinates.

Each trigonometric point is related to a feature that can be identified in both SDO/HMI and SO/PHI images. Their 3D HEEQ coordinates can be derived from their position in the SDO/HMI image and the spacecraft position as described in Section 1.2.1.

Once the HEEQ coordinates of each trigonometric point have been determined, their normalized coordinates in the observations of both spacecraft can be found with equation (1.23), and and then again their pixel coordinates using the mapping of Eq. 1.27. If $\mathbf{R}$ and $\mathbf{K}$ are correct, the pixel coordinates obtained for each point in the SDO/HMI image should be the same as the observed ones. Else, a correction must be applied with the procedure described here.

For each point in the SO/PHI image, there are two pixel positions: the mapped pixel position $(p_{x,i}, p_{y,i})_{map}$, obtained from the HEEQ coordinates of each point, derived using the intrinsic and extrinsic camera matrices of the SDO/HMI image, and the observed pixel position $(p_{x,i}, p_{y,i})_{obs}$, where the trigonometric point is actually seen in the SO/PHI image.

We define a discrepancy vector of the stacked distances of all trigonometric points

$$d\mathbf{r} = (d\mathbf{r}_1, d\mathbf{r}_2, ..., d\mathbf{r}_N) \tag{4.1}$$

where N is the number of trigonometric points used, and

$$d\mathbf{r}_i = (p_{x,i,map} - p_{x,i,obs}, p_{y,i,map} - p_{y,i,obs}). \tag{4.2}$$

Similar to $d\mathbf{r}$, by measuring the distance between $(p_{x,i}, p_{y,i})_{obs}$ and the rotation center of the image at CRPIX, another vector is given by

$$\mathbf{r} = (\mathbf{r}_1, \mathbf{r}_2, ..., \mathbf{r}_N) \tag{4.3}$$

where

$$\mathbf{r}_i = (\texttt{CRPIX1} - p_{x,i,obs}, \texttt{CRPIX2} - p_{y,i,obs}). \tag{4.4}$$

The quantities from the SO/PHI header that will be corrected are CRPIX1, CRPIX2, and CROTA. Assuming that the corrections are small, the corrected values are given by

$$\begin{aligned}\texttt{CROTA}' &= \texttt{CROTA} + dA \\ \texttt{CRPIX1}' &= \texttt{CRPIX1} + dP_x \\ \texttt{CRPIX2}' &= \texttt{CRPIX2} + dP_y.\end{aligned}$$

The mapped positions of each point can then be found from

$$\begin{aligned}(\texttt{CRPIX1} - p_{x,i,obs}) + (p_{x,i,map} - p_{x,i,obs}) = \\ \cos(dA) * (\texttt{CRPIX1} - p_{x,i,obs}) - \sin(dA) * (\texttt{CRPIX2} - p_{y,i,obs}) + dP_x\end{aligned} \tag{4.5}$$

and

$$\begin{aligned}(\texttt{CRPIX2} - p_{y,i,obs}) + (p_{y,i,map} - p_{y,i,obs}) = \\ \sin(dA) * (\texttt{CRPIX1} - p_{x,i,obs}) + \cos(dA) * (\texttt{CRPIX2} - p_{y,i,obs}) + dP_y.\end{aligned} \tag{4.6}$$

A a $2N \times 3$ rotation matrix can be defined from Eq. 4.4 as

$$\mathbf{M} = \begin{pmatrix} -(\texttt{CRPIX2} - p_{y,1,obs}) & 1 & 0 \\ (\texttt{CRPIX1} - p_{x,1,obs}) & 0 & 1 \\ -(\texttt{CRPIX2} - p_{y,2,obs}) & 1 & 0 \\ (\texttt{CRPIX1} - p_{x,2,obs}) & 0 & 1 \\ \cdots & & \\ -(\texttt{CRPIX2} - p_{y,N,obs}) & 1 & 0 \\ (\texttt{CRPIX1} - p_{x,N,obs}) & 0 & 1 \end{pmatrix}, \tag{4.7}$$

and the vector containing the increments to the original header values is

$$d\mathbf{P} = (dA, dP_x, dP_y). \tag{4.8}$$

Then the system to solve (Eqs. 4.5 and 4.6) is determined by the distance vector $d\mathbf{r}$, the rotation matrix $\mathbf{M}$ and $d\mathbf{P}$. This problem is overdetermined, so that a least square minimization is required to find a solution for the system. The expression to be minimized is

$$\|d\mathbf{r} - \mathbf{M} * d\mathbf{P}\|^2, \tag{4.9}$$

such that the the features have the smallest possible distance to their mapped positions, or such that $d\mathbf{r}$ is as small as possible, once the corrections have been applied.

Expanding 4.9 and then equating the gradient in $d\mathbf{P}$ to zero yields after solving for $d\mathbf{P}$

$$\|d\mathbf{r} - \mathbf{M} * d\mathbf{P}\|^2 = dr^2 - 2dr^T MdP + dP^T M^T MdP$$
$$-dr^T M + M^T MdP = 0$$

$$d\mathbf{P} = (\mathbf{M}^T * \mathbf{M})^{-1}\mathbf{M}^T * d\mathbf{r}. \tag{4.10}$$

which according to equation 4.8 is the vector with the increments to be added to `CROTA`, `CRPIX1`, and `CRPIX2`, respectively.

In this case, for any given number N of points used for this affine correction, the distance vector dr and the rotation matrix $\mathbf{M}$ grow, having a size of $2N$, and $2N \times 3$, respectively, which can still be solved using expression 4.10, regardless of the amount of points used.

The minimization of equation 4.10 gives a set of corrections to the WCS header entries that is fitted to the points used. Since after each iteration `CRPIX1`, `CRPIX2`, `CROTA` and therefore $(p_{x,i}, p_{y,i})_{map}$ are updated, matrix (4.7) changes also and multiple iterations are necessary. The values `CROTA`, `CRPIX1` and `CPRIX2` are updated in each iteration, and the whole correction is repeated until convergence. After a few iterations the quantities in $d\mathbf{P}$ are smaller than the precision given in the headers, so that the final corrections to the WCS header entries are contained in $d\mathbf{P}$ after the last iteration.

This algorithm yields good corrections to obtain the smallest possible $d\mathbf{r}$ on the SO/PHI image, with $(p_{x,i}, p_{y,i})_{map}$ obtained from $(p_{x,i}, p_{y,i})_{obs}$ in the SDO/HMI image. It does not take into consideration other effects, like distortion in the images, so that the agreement between $(p_{x,i}, p_{y,i})_{obs}$ and $(p_{x,i}, p_{y,i})_{map}$ is as good as possible but not always perfect.

Another fact to consider is the resolution of the images. The SDO/HMI images have a much larger pixel than those of SO/PHI, so even if the discrepancy is larger than a pixel in the SO/PHI images, it still might be smaller than one SDO/HMI pixel, meaning that the correction is good enough for the purposes of the stereoscopic analysis of this work.

This procedure was applied to the observations from SO/PHI and SDO/HMI presented and described in the previous section. In this section, the observations from March 3rd are used to visualize how the procedure works. Figure 4.10 shows a sunspot group in both images. For the calibration, two features in the quiet Sun were selected, marked with two different symbols in the upper panel. Assuming that both features are located at 1 solar radius, their 3D coordinates can be found using equation 1.41. To localize the sub pixel position of the minimum intensity of both points, the image intensities were interpolated.

In the lower panel of figure 4.10 is the observation from SO/PHI. When mapping the points into the SO/PHI image, the mapped pixel positions are off from the observed positions by about 60 SO/PHI pixels. The mapped points are marked with corresponding symbols from the SDO/HMI image. The symbols are plotted at $(p_{x,i}, p_{y,i})_{map}$, while the dashed line points to $(p_{x,i}, p_{y,i})_{obs}$, being elements of the distance vector $d\mathbf{r}$, lines $d\mathbf{r}_1$ and $d\mathbf{r}_2$.

Figure 4.11 shows $\mathbf{r}_1$ and $\mathbf{r}_2$, again marked with a dashed line in the SO/PHI image.

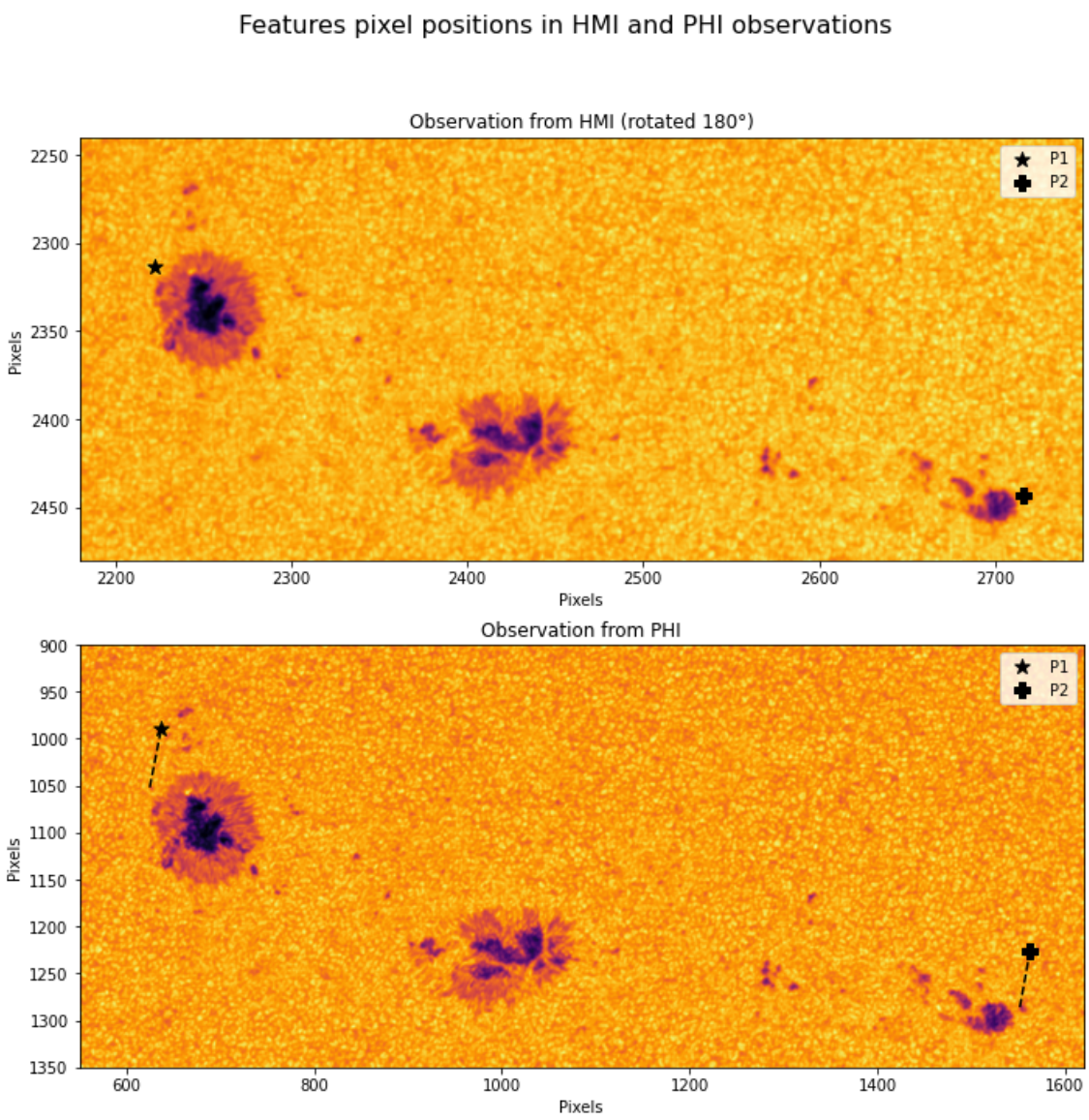

Figure 4.10: Close up to the field of view and the identified features for the correction. The top panel is the SDO/HMI image and the two symbols are the positions of the two features. The bottom panel is the image from SO/PHI , where the symbols are the positions of the features according to the SDO/HMI projection. In dashed lines is the vector from the projected position to the actual position.

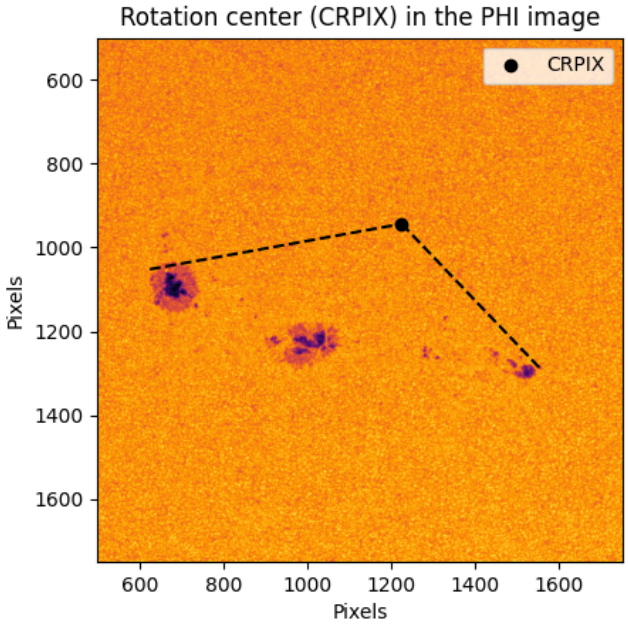

Figure 4.11: r vector from the position of the observed features to the position of CRPIX in the SO/PHI image.

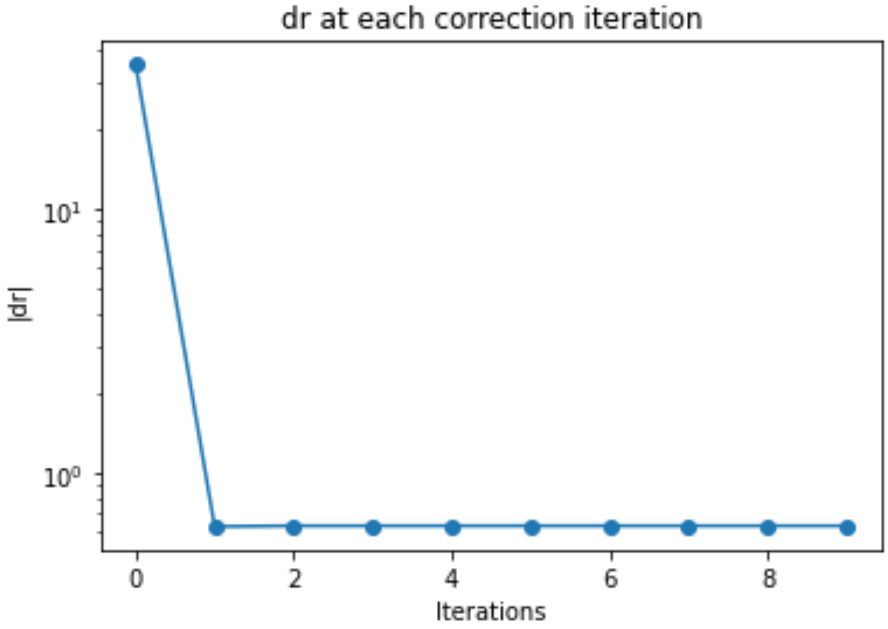

Figure 4.12: Measure of the error during 10 iterations. The error is here quantified as $|d\mathbf{r}|$

The convergence after each iteration of the correction is shown in figure 4.12. Most of the correction is achieved in the first iteration, and after 6 iterations the final $d\mathbf{r}$ is achieved. The initial $d\mathbf{r}$, measured in image pixels, was $[10.66,\ -59.09,\ 12.10,\ -62.28]$ or $|d\mathbf{r}| = 61.25$, and after the correction is $[-0.584,\ 0.17,\ 0.17,\ -0.36]$, with a norm $|d\mathbf{r}| = 0.63$. There is a small remaining error because successive affine transformations due to modifications of `CROTA`, `CRPIX1` and `CRPIX2` in the SO/PHI header restrict the possible movement in $(p_x, p_y)_{i,map}$. However, the final error is orders of magnitude smaller than the initial one, and the corrections found for `CROTA`, `CRPIX1` and `CRPIX2` are substantial.

The results of the correction are shown in figure 4.13. After the correction, the agreement between $(p_x, p_y)_{map}$ and $(p_x, p_y)_{obs}$ is much better and the symbols are in the same position in both images. A close up is given in figure 4.14. Again, $(p_x, p_y)_{map}$ is plotted with the symbols, and the dashed line points to $(p_x, p_y)_{obs}$.

With this example it is demonstrated that the procedure here proposed can improve the camera attitude and improve the corresponding FITS entries. It is assumed that the images from SDO/HMI are perfectly calibrated so that the observed features can be used to calculate the 3D coordinates of the points. Even if the calibration of the SDO/HMI image is not perfect, this procedure brings both images to a consistent agreement. An error in the SDO/HMI attitude parameters would result in an error in the SO/PHI parameters, so that both cameras would have a constant angle and/or misplacement of the solar center. However, this would still allow to perform the stereoscopic analysis using the calibrated data from both cameras.

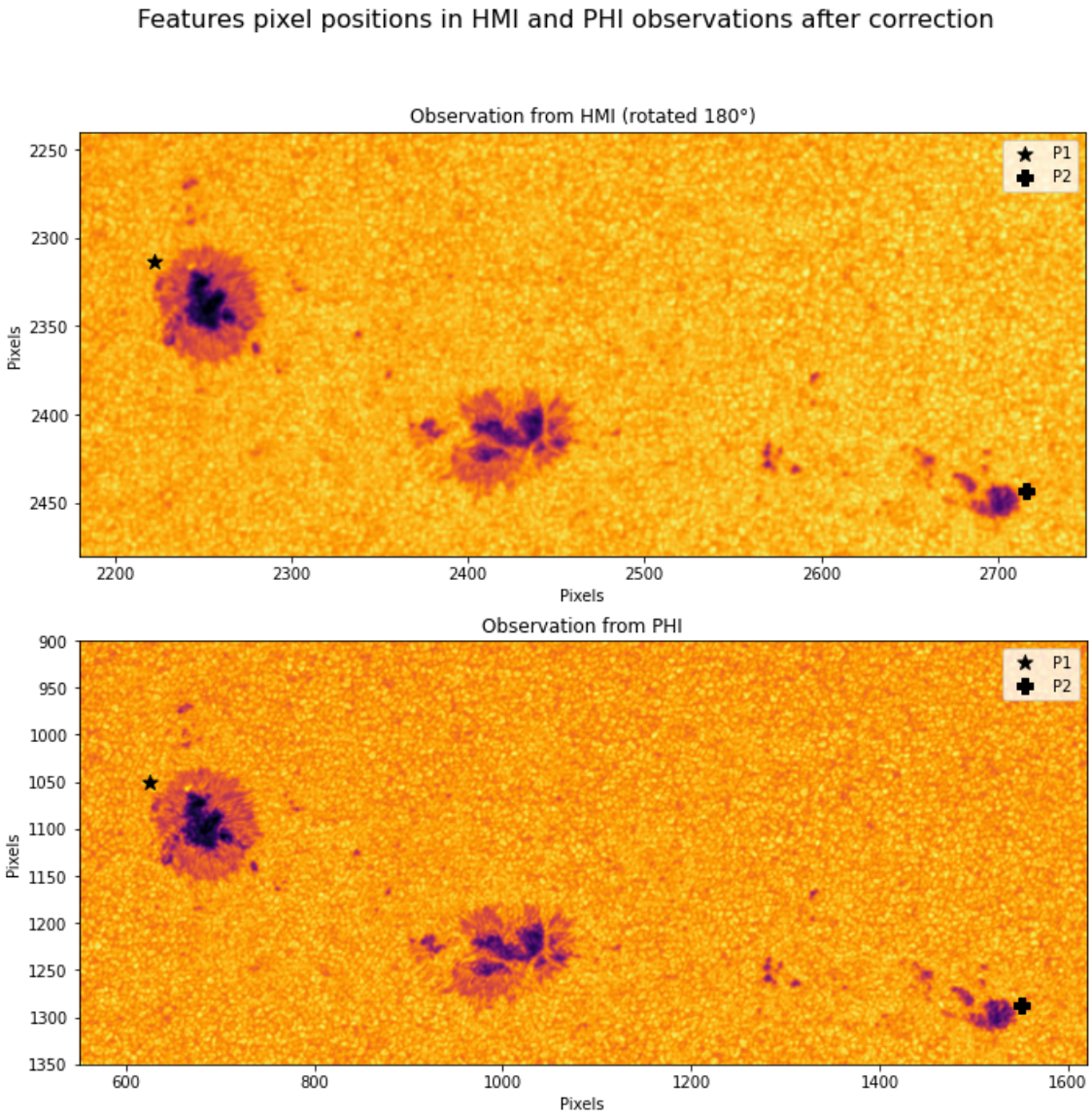

Figure 4.13: Close up to the field of view and the identified features after the correction. The top panel is the SDO/HMI image and the two symbols are the positions of the two features. The bottom panel is the image from SO/PHI where the symbols are the positions of the features according to the SDO/HMI projection. As opposed to Figure 4.10, the symbols here appear in the same position as in the SDO/HMI image.

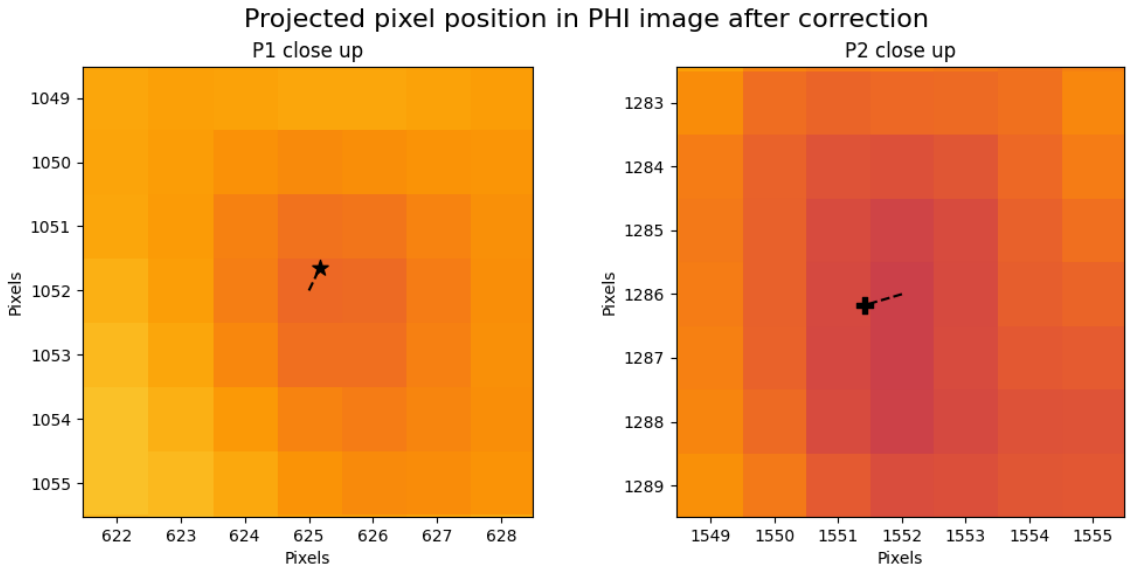

Figure 4.14: Close up to the trigonometric points on the solar surface used for the correction. The symbols are the positions of the mapped points $(p_{x,i}, p_{y,i})_{map}$ obtained from their projection in the SDO/HMI image, and the dashed line points to the observed position $(p_{x,i}, p_{y,i})_{obs}$ in the SO/PHI image. After the correction the distance between the projected and the observed position of each feature is smaller than one image pixel.

4.2 Results of the Method Applied to Real Data

To test the performance of the correlation method with real data, observations from October 29th of 2002 at 06:43 UT were used. The observations on this day were selected for the test because the sunspot appeared within $25°$ to the disk center in the full disk observation of SDO/HMI , the separation of both spacecraft was not too large, and because each spacecraft observed the sunspot from a different side, allowing to gain information about the slopes on both sides of the sunspot. The results in this section were produced following the steps described in Chapter 2. Here we show some intermediate steps as well as the final results obtained. The original, unrectified observations from both SO/PHI and SDO/HMI are presented in figure 4.15.

On the day of the observation SDO/HMI was the spacecraft ahead, while SO/PHI was behind. Their positions in HEEQ coordinates of SDO/HMI and SO/PHI are $[1.48 \times 10^8,\ 1.11 \times 10^5,\ 1.21 \times 10^7]$ km, and $[5.21 \times 10^7,\ -4.25 \times 10^7,\ 8.86 \times 10^6]$ km respectively, corresponding to a distance from the Sun of 0.99 and 0.45 AU. The separation between both spacecraft was of roughly $39°$. Both images were rectified and a close up to the sunspot in both rectified images is shown in figure 4.16.

When using the test data, the grid spacing was equidistant in image pixels. In the case of real observations the grid is mapped onto the rectified images as said in Section 2.1.1. This grid takes into account the curvature of the Sun, so that the grid spacing is constant in the longitudinal direction φ, but not equidistant in the homogeneous coordinate t_x or in image pixels. Figure 4.17 shows an example of the grid mapped onto a rectified image. The central point in the grid of figure 4.17

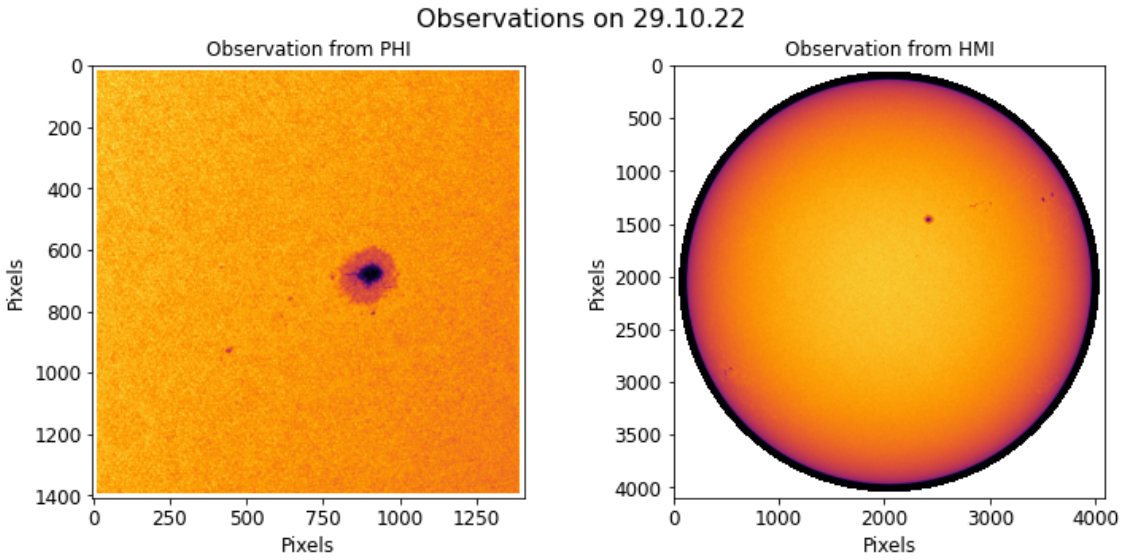

Figure 4.15: Observations from SO/PHI and SDO/HMI on October 29th of 2022.

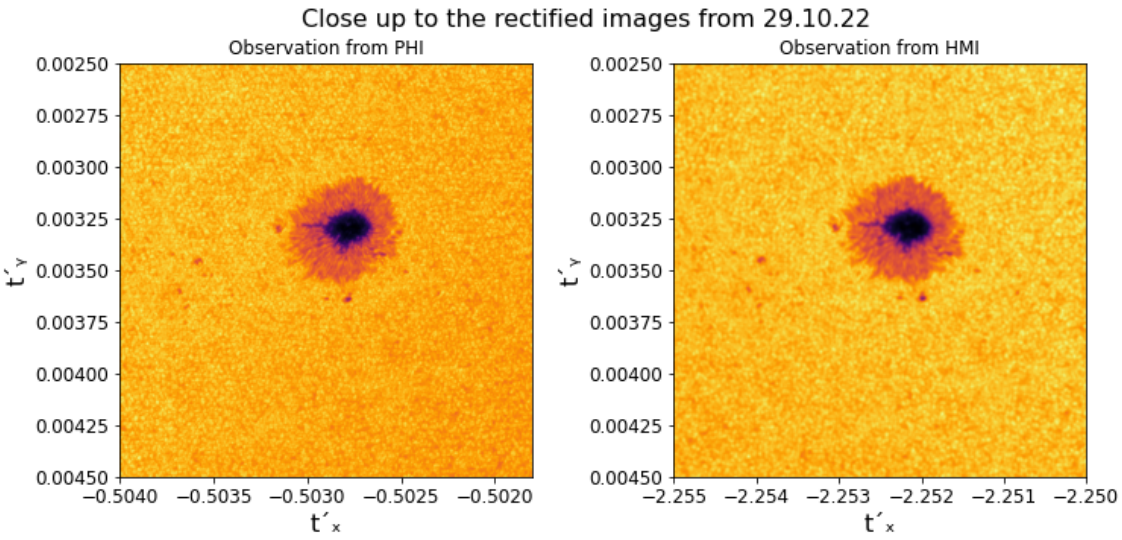

Figure 4.16: Close up to the sunspot in the rectified images of the observations of October 29th of 2022.

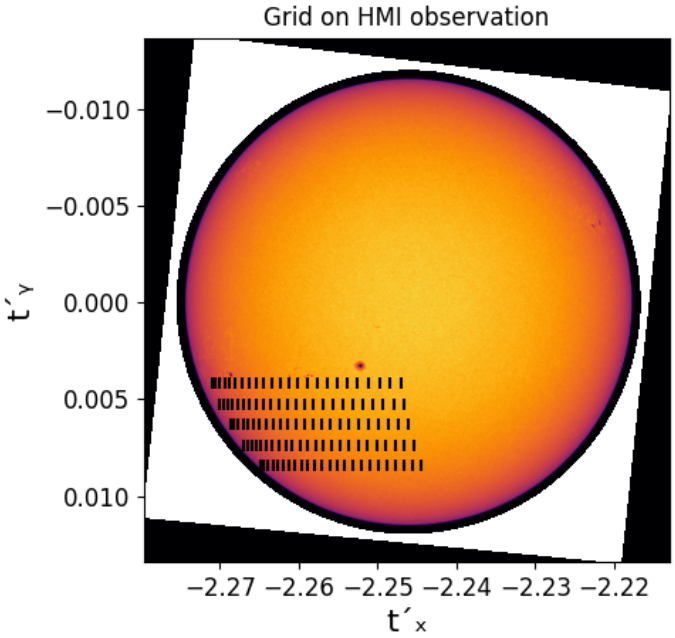

Figure 4.17: Grid mapped onto the rectified image from SDO/HMI . The horizontal sampling size of the grid is of $\Delta\varphi = 3°$ and the vertical spacing of $d\epsilon = 0.061°$.

is in the HEEQ position $[6.29 \times 10^5,\ -1.33 \times 10^5,\ 2.64 \times 10^5]$ km and has epipolar parameters of $\varphi = 30.92°$, $\zeta = 362858.6$ and a radius $\rho = 593927.3$ km. Each epipolar line above and below the reference line at ζ (the epipolar line of the central point, and third one from top to bottom) is at an inclination of $d\varepsilon = 0.061°$, and in each epipolar line the horizontal spacing is of $\Delta\varphi = 3°$.

It is evident in Fig. 4.17 that towards the solar limb the grid boundaries, displayed in small vertical lines, lie closer to each other, regardless of the pixel sampling in the image. This affects the production of the VIPs, so that for this stereoscopic analysis the features to study should preferably lie closer to the disk center, so that the pixel sampling for the VIPs is approximately constant throughout the grid. Since each grid is mapped along an epipolar profile, visualizing each horizontal grid is equivalent to visualizing an epipolar profile. These two terms are used interchangeably throughout this section.

Once the grid boundaries have been mapped onto the rectified images, the pixel intensities within each grid cell are integrated into one data point of the VIP. This integration for a single VIP value may involve one or more image pixels and fractions of them, depending on the grid spacing $\Delta\varphi$ and the pixel resolution of the rectified images. The integration simply consists of an averaging of the image pixels within each surface grid cell. Figures 4.18 and 4.19 show the epipolar grid mapped onto both rectified images and the corresponding VIPs obtained by integrating the image intensities within the grid cells. Figure 4.18 shows the full grid and VIPs, while figure 4.19 shows a close up of the grid, in order to visualize the grid sampling with respect to the image sampling. Given the different resolution between the observations from SO/PHI and SDO/HMI , the grid sampling is between the image resolutions of both, so that the SDO/HMI image is not too much oversampled, and not much detail is lost in the SO/PHI image.

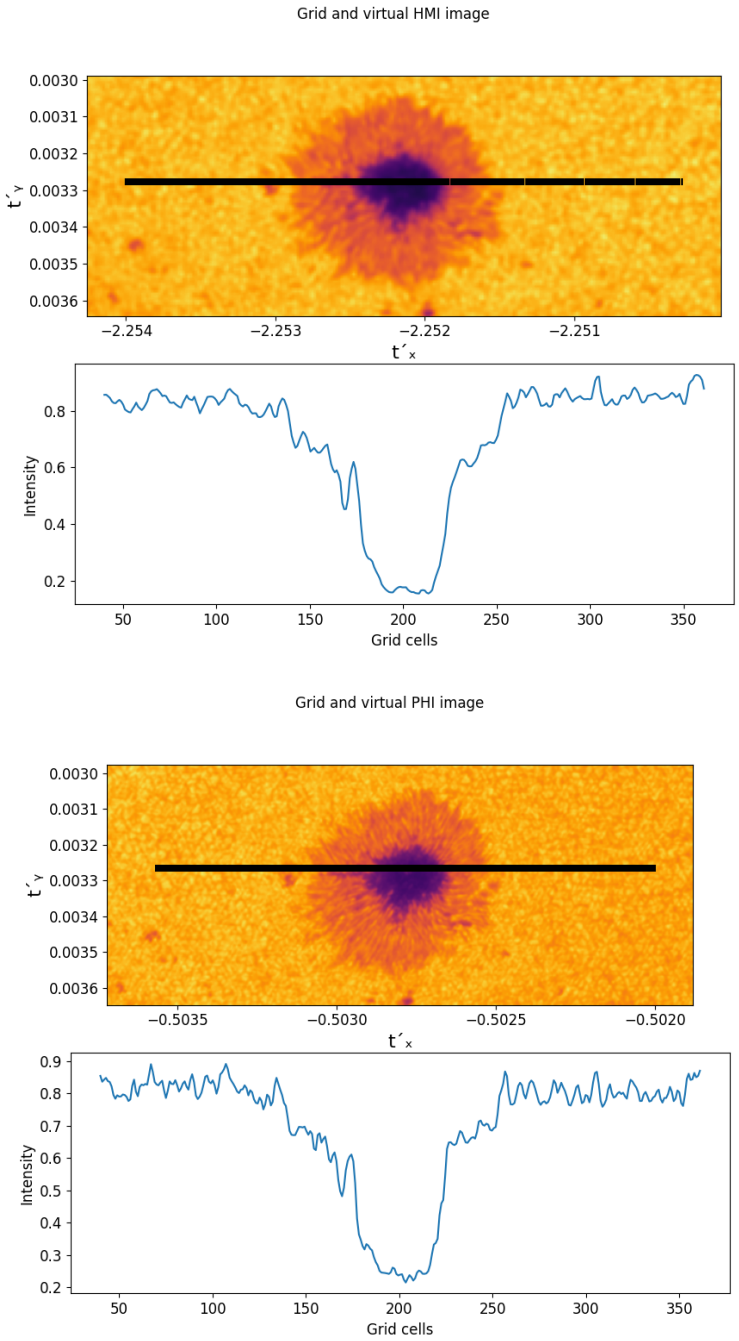

Figure 4.18: Grid and VIPs on the rectified SDO/HMI (top) and SO/PHI (bottom) images

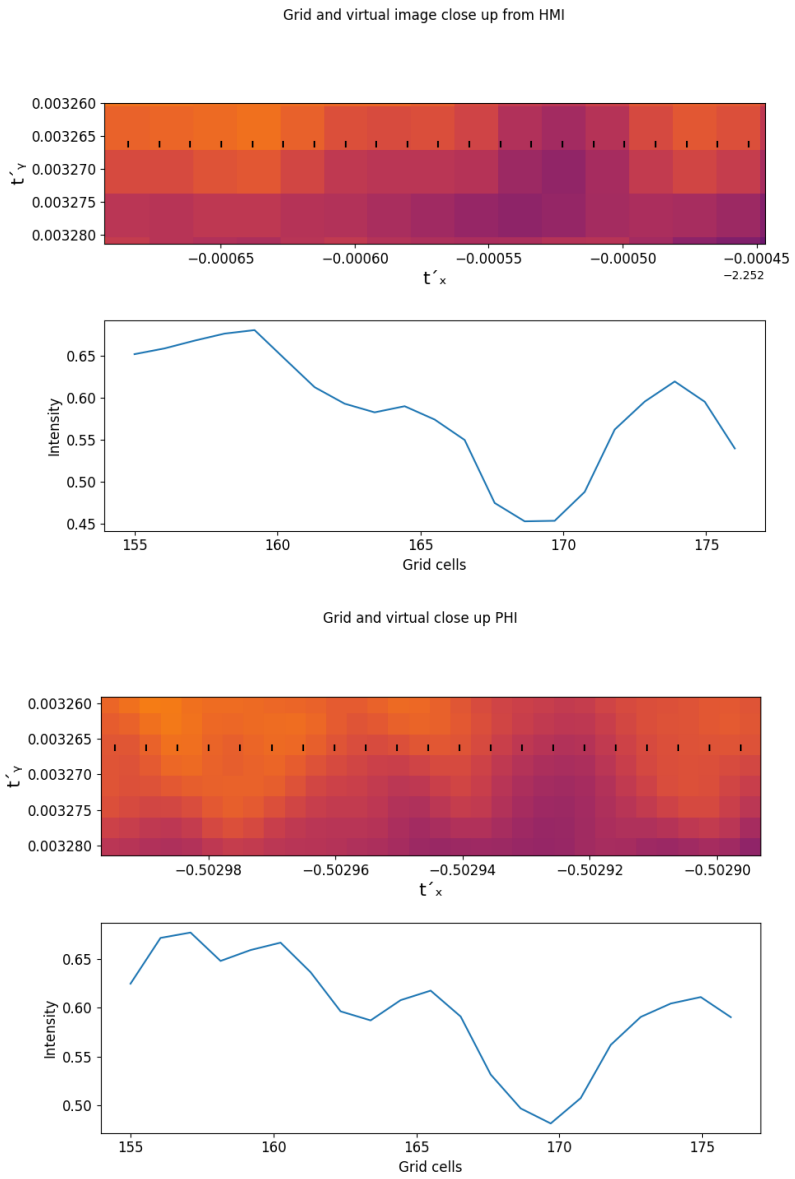

Figure 4.19: Close up to the grid and VIPs on the rectified SDO/HMI (top) and SO/PHI (bottom) images. The grid spacing used to produce the VIPS is of $\Delta\varphi = 0.0025°$. The surface grid boundaries are marked by black sticks, the image pixel size is visible in the color pattern.

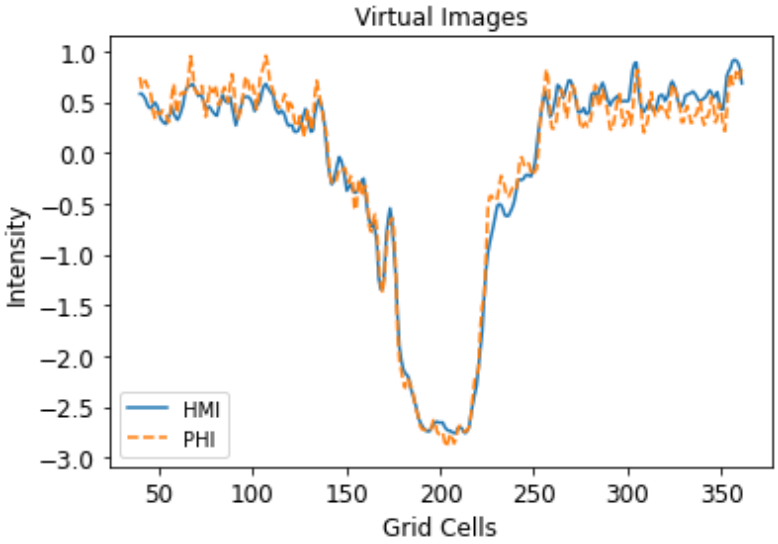

Figure 4.20: VIPs of the rectified images of October 29th obtained by the integration of the grids of figure 4.18.

In this case the comparison is made only for one epipolar profile. The central point in this grid is at a position of $[6.3E05,\ -1.3E05,\ 2.6E05]$km, with epipolar coordinates of $\varphi = 52.5°$, $\rho = 667204.3$ km, $\zeta = 198127.4$, and equivalently $\varepsilon = 0.18°$. The viewing angles at the central point in the grid, are $\gamma_{SDO/HMI} = -13.5°$ = and $\gamma_{SO/PHI} = 25.8°$ (see Eq. 2.13). The grid spacing is of $\Delta\varphi = 0.025°$.

Once the two VIPs have been produced, it is straight forward to perform the correlation method. The two VIPs are shown in figure 4.20. The two VIPs are shifted with respect to one another following the relationship given in equation 2.14 and the correlation is calculated for each shift.

The height variations are calculated at each grid point from the shifts which yield the largest correlation. For the correlation coefficients at a given shift, the window size plays an important role on the performance of the method and the resulting dh. In figure 4.21 the effect of the window size is shown. On the left diagram both VIPs are plotted, and the shadowed boxes show two different window sizes around the same point, marked with a vertical line in the middle of the windows. The right diagram shows the correlation as a function of the total shift $d\varphi_{SDO/HMI} - d\varphi_{SO/PHI}$ for the same grid point, but obtained by correlating the windowed data with the two different sizes. The black curve on the right diagram was obtained by correlating the data with a window of the size of the gray box on the left diagram, while the green curve was obtained by correlating the data with a window size indicated by the green box on the left diagram.

Since the shift that yields the best correlation is converted into dh, it is clear from figure 4.21 that the size of the window plays a very important role on the estimated height variations, even if it is calculated for the same point. Not only is the highest correlation different at different shifts, but the overall correlation value also changes for different window sizes. Figure 4.22 explains this effect better. The correlation is computed as a function of the total shift for all the half window sizes between 5 and 45 grid points. The horizontal axis corresponds to the total shift, and thereby to height; the vertical axis corresponds to the different window sizes. The color map

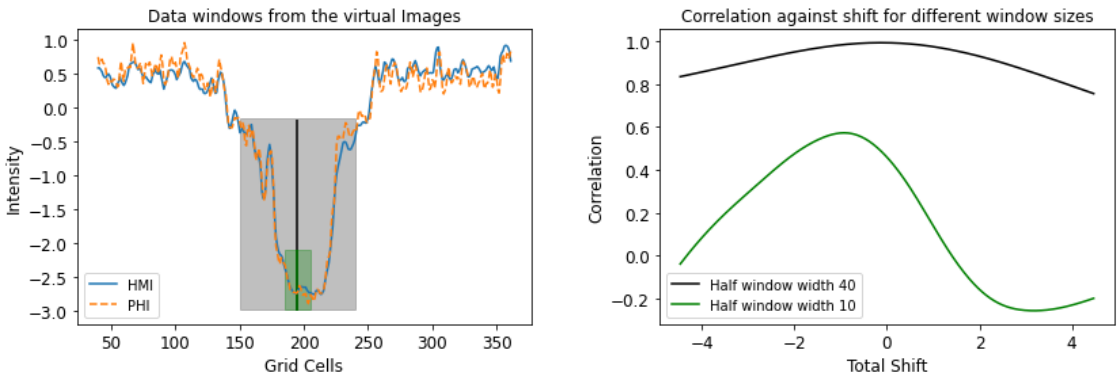

Figure 4.21: Virtual images with the selected window sizes marked in shadowed boxes (left), and the correlation as a function of the total shift, in units of grid cells, for each of the windows of data (right).

shows the value of the correlation. In black is displayed the point for which the correlation is largest for each window size.

The correlation is highest for larger window sizes, and its behavior is more or less constant for larger windows. When the windows are smaller the correlation is more local, so a better resolution can be achieved in φ. However, since less data is involved in the calculations the results may be less stable and prone to have outliers. Given that the aim is to determine the Wilson depression, a large window size will be used for the further calculations, because the correlation is more reliable, even if that results in a loss of detail as described in Chapter 3.

The selected half window size is 40 points. The shift $d\varphi$ that yields the best correlation can be converted into dh by using Eqs. 2.12, 2.14, and 2.16 and the process is repeated for all the grid points in the VIPs while using the same window size for each one of them. The estimated height variations along the epipolar profile of figure 4.20 are shown in figure 4.23.

The reconstructed dh in the lower panel of figure 4.23 shows a larger depression in the center of the sunspot, as well as some smaller scale variations; but a general upward trend in the resulting dh curve is also present. This effect could be due to distortion in the images, or again to a wrong value in the header entries of the SO/PHI image. To test if this upward trend is systematic throughout the image, the height variation was calculated along five different profiles in the quiet Sun. The corresponding epipolar lines are displayed in figure 4.24, and the respective VIPs in figure 4.25. The height variation was calculated for each of the epipolar profiles in figure 4.24.

The results of this test are displayed in figure 4.26. They show the same increasing trend as the results from figure 4.23. It is present in all the reconstructed dh curves. This trend can directly be traced back to the VIPs. It can be seen, comparing the maxima and minima of the VIPs in figure 4.25 that there is a shift between the VIPs that increases steadily from left to right. The VIPs from SO/PHI have an offset towards the end, compared to the VIPs from SDO/HMI. We assume that this is an artifact due to either a distortion in the images or due to an imprecise `CDELT` value, i.e. an inaccuracy in the plate scale.

A wrong `CDELT` in the VIPs of SO/PHI in figure 4.25 would result in a stretching with respect to those of SDO/HMI. For this reason one can assume that the `CDELT`

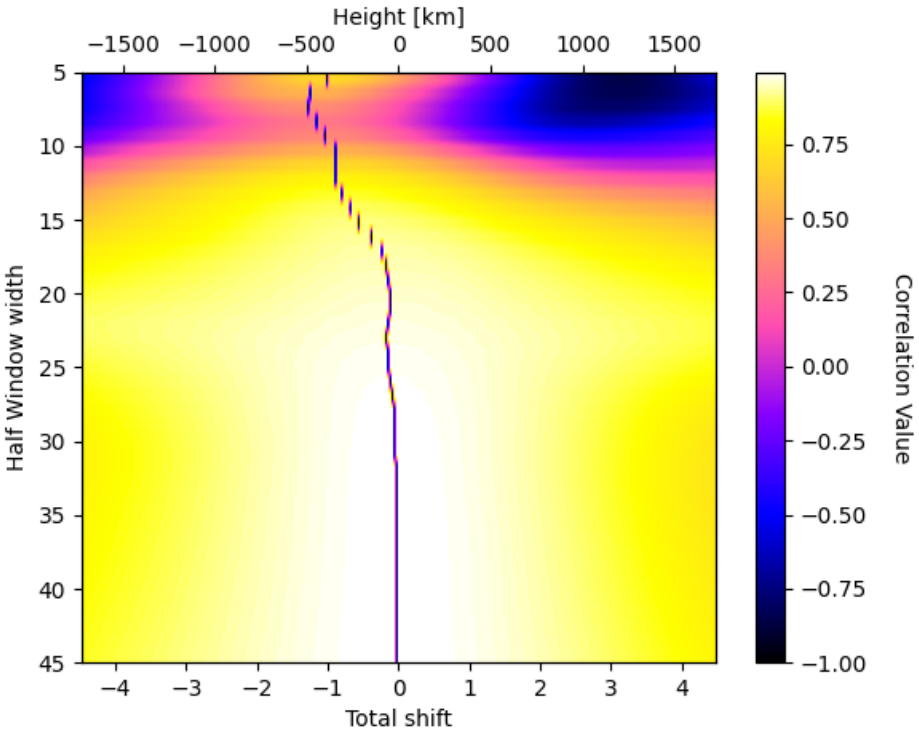

Figure 4.22: 2D map of the correlation as a function of the total shift for a range of window sizes.

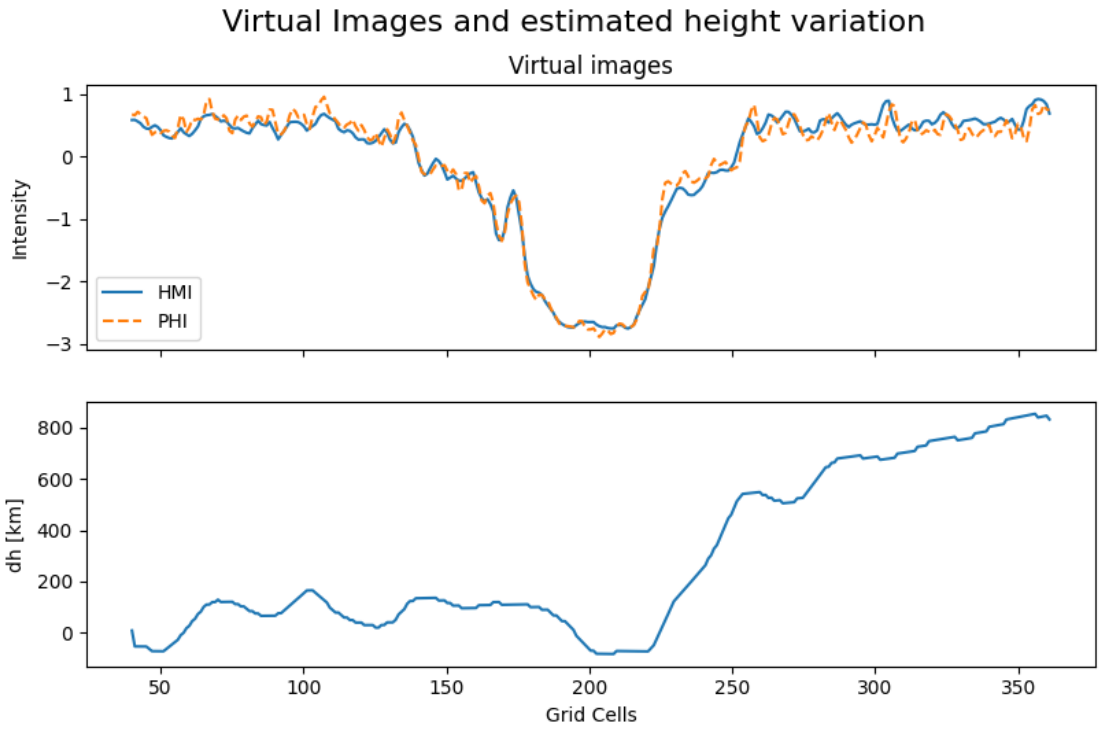

Figure 4.23: VIPs (top) and reconstructed dh (bottom) corresponding to the epipolar profile of Fig. 4.18

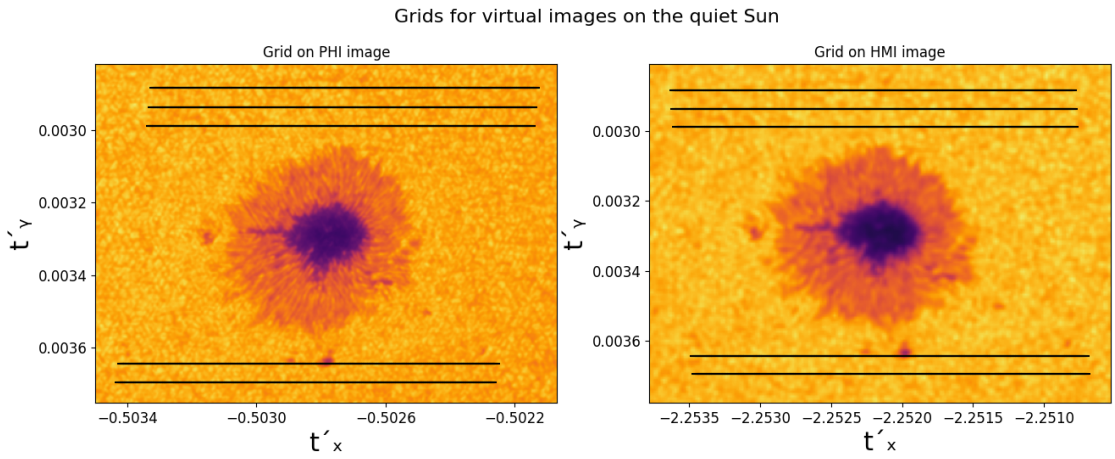

Figure 4.24: Epipolar profile and grids along the quiet Sun.

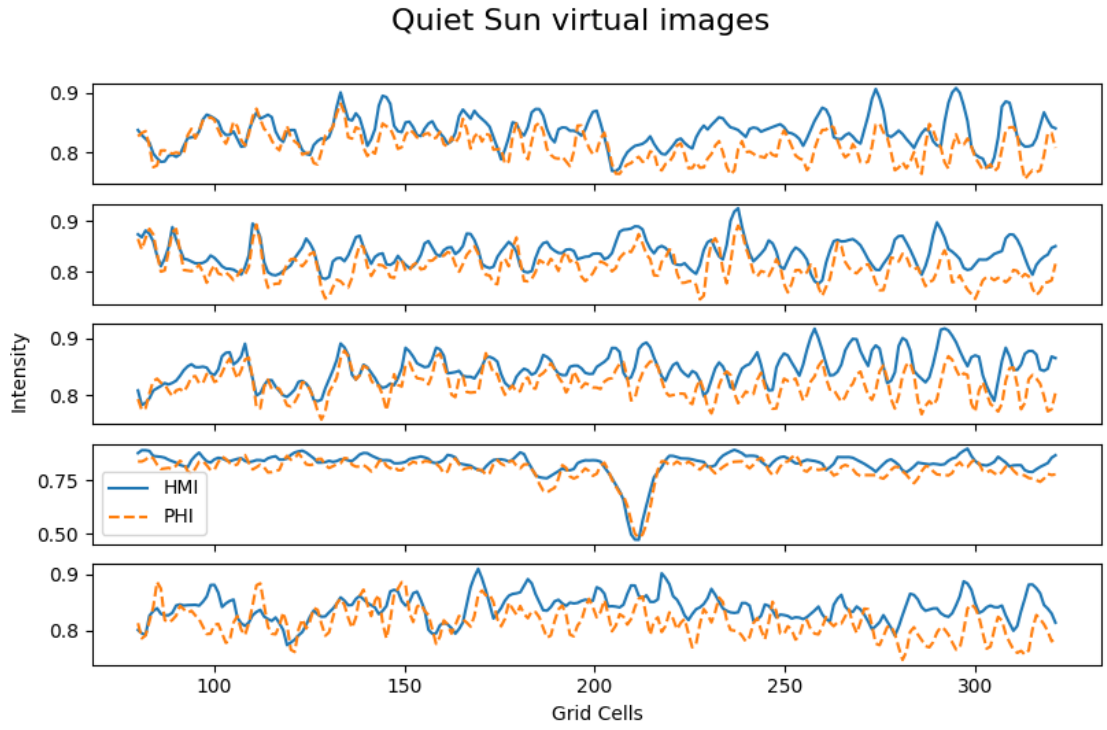

Figure 4.25: Virtual images corresponding to the grids on figure 4.24. The order is the same from top to bottom.

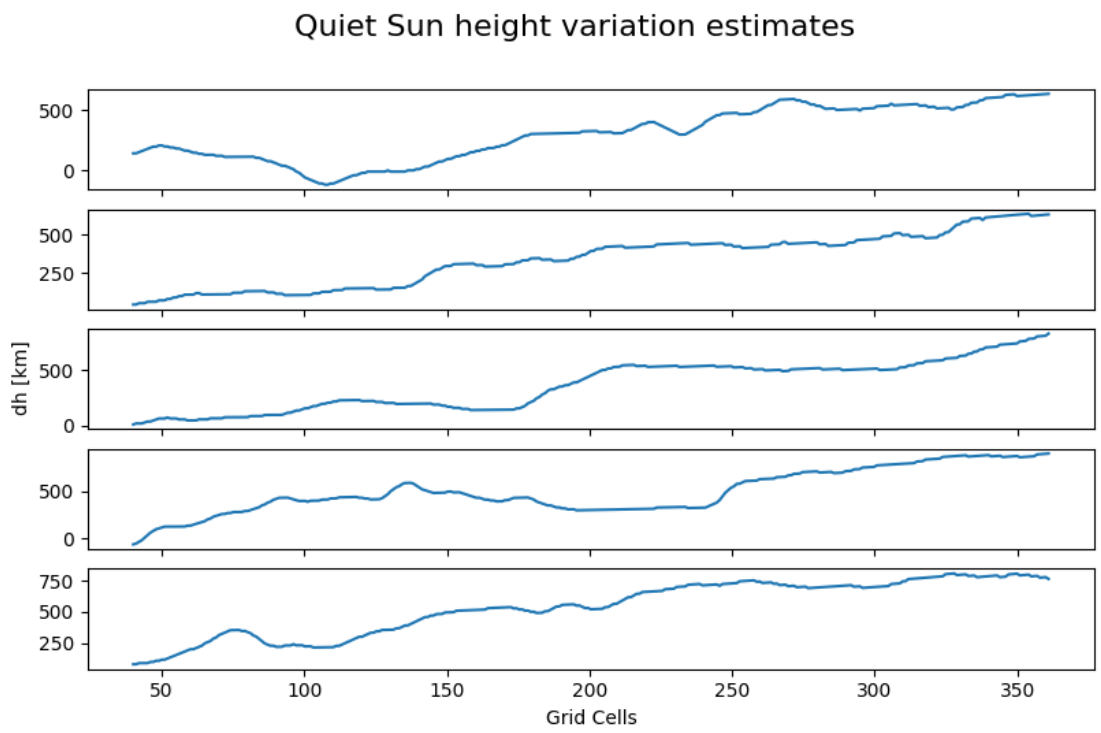

Figure 4.26: Estimated height variation curves for the quiet Sun by the correlation of the pairs of VIPs of figure 4.25. The order is the same from top to bottom.

value in the SO/PHI images is slightly too large. A correction in the CDELT values from 0.5 arc seconds as given in the header of the SO/PHI image, to 0.49745 arc seconds was made, and then the rectification and recalculation of all the parameters, as well as the VIPs from SO/PHI were done. The corrected VIPs are displayed in figure 4.27, where the stretching is no longer visible, as opposed to the VIPs of figure 4.25.

The resulting dh curves are displayed in figure 4.28. The upward trend is removed. Some of the dh results present gaps with no data in the reconstructed height variation curves. This occurs when the correlation method yields large outliers in the results, so those values were deleted from the final curves.

Equivalent to calculating the height variations along the epipolar profiles of figure 4.24, the height variations along the epipolar profile of figure 4.18 are recalculated with the correction in the CDELT and presented in figure 4.29. After the plate scale value correction the dh curve of figure 4.29 looks similar to that of figure 4.23 but without the upward trend.

The height variations of figure 4.29 show a base level that corresponds to the quiet Sun, and a depression within the sunspot of approximately $700 - 800$ km, even though the absolute height values were not determined, since the quiet Sun to the right of the spot appears to be offset by 200 km from the standard solar radius $R_\odot = 6.96 \times 10^8$ km, used in the calculations. The dh curve also reconstructs the height variations in the penumbra region of the sunspot wider than it appears in the VIPs, and there is a visible offset between the minimum intensity and the minimum dh estimate. In this example profile, the topography of the sunspot shows a much smaller bottom plateau than its brightness variation suggests.

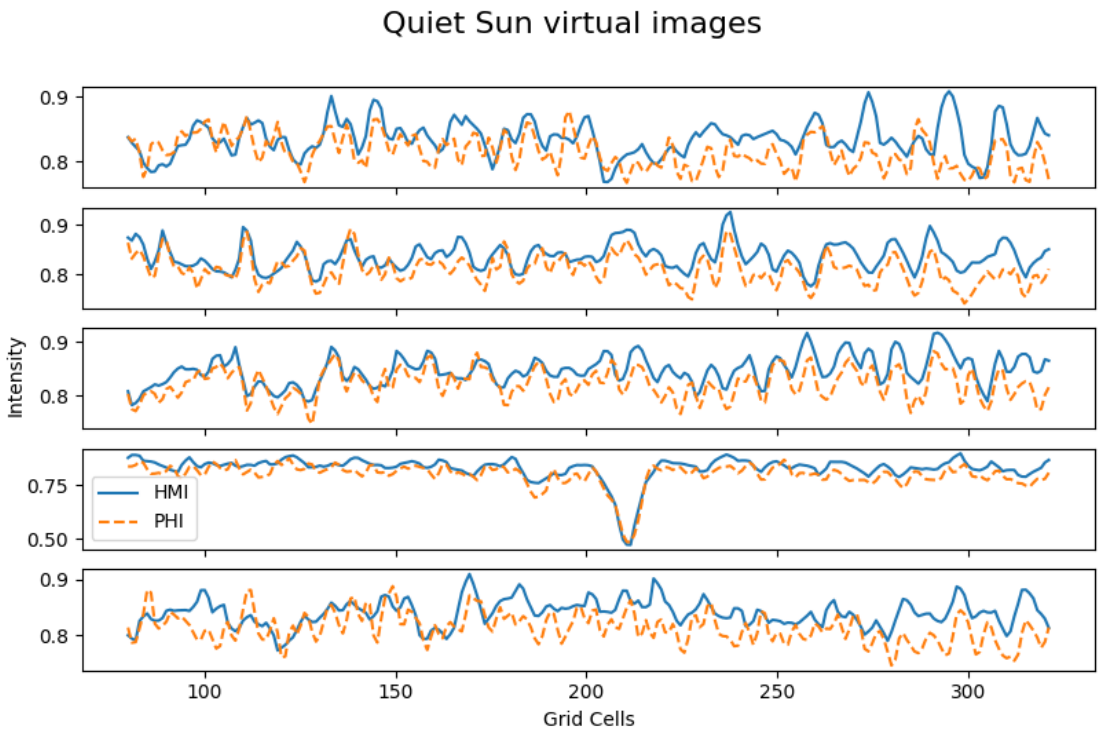

Figure 4.27: Virtual images corresponding to the grids on figure 4.24 after the correction of the CDELT values in the SO/PHI image. The order is the same from top to bottom.

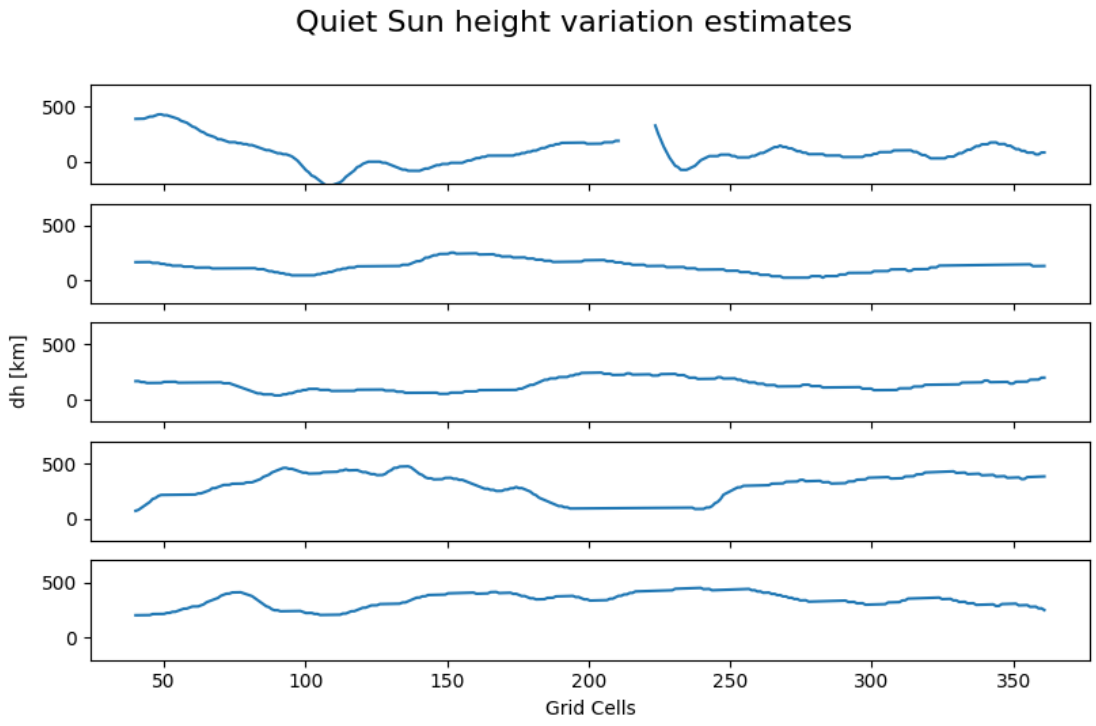

Figure 4.28: Estimated height variation curves for the quiet Sun by the correlation of the pairs of VIPs of figure 4.27. The order is the same from top to bottom.

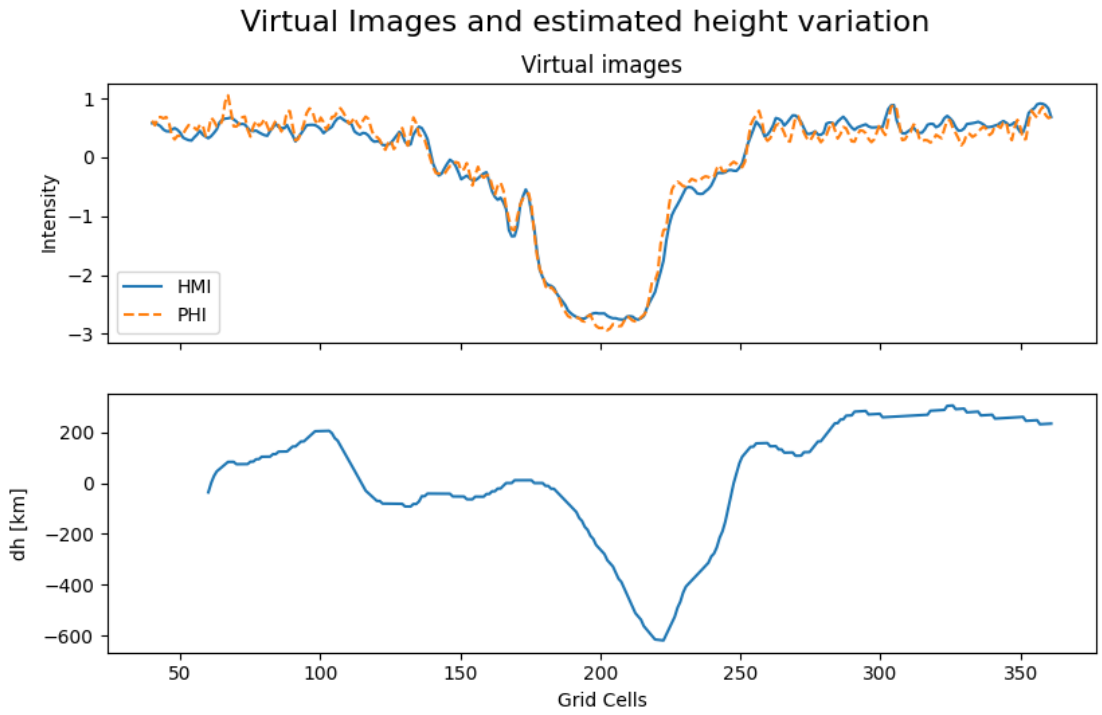

Figure 4.29: VIPs (top) and reconstructed dh (bottom) corresponding to the epipolar profile of Fig. 4.18 after the correction of the CDELT values in the SO/PHI image.

In the following sections we investigate, whether this result holds if the parameters of our calculation are modified.

Testing the Effect of Different Grid and Window Sizes

In this section different grid spacing is tested, estimating the height for the same epipolar profile as in the previous section, but with a grid ten times finer, and a grid four times more coarse than the grid displayed in figure 4.18. The window size used was the same as for the height variations in figure 4.29.

The results of varying the grid spacing are shown in figures 4.30 and 4.31. The grid spacing used to produce the height estimates from figure 4.30 was ten times finer than that of the figure 4.29, or $\Delta\varphi = 0.0025°$, corresponding to $\rho\Delta\varphi = 30$ km. The grid spacing used for figure 4.31 was of $\Delta\varphi = 0.1°$, or $\rho\Delta\varphi = 1165$ km.

The reconstructed height using a finer grid behaves similarly to that of figure 4.29. There is a slight improvement in the resolution so that finer structures can be reproduced but the overall behavior of the results does not change significantly in comparison with the first results. On the other hand, if the grid is very coarse, the quality of the results decreases. The overall depth of the depression of 800 km was reproduced for all grid sizes. To find the optimum grid size the effect of varying the grid only slightly was also tested: the grid size was 1.5 and 2 times finer, and then coarser than that of Fig. 4.29. Varying the grid size slightly did not affect the results in any remarkable way, and therefore they are not presented here.

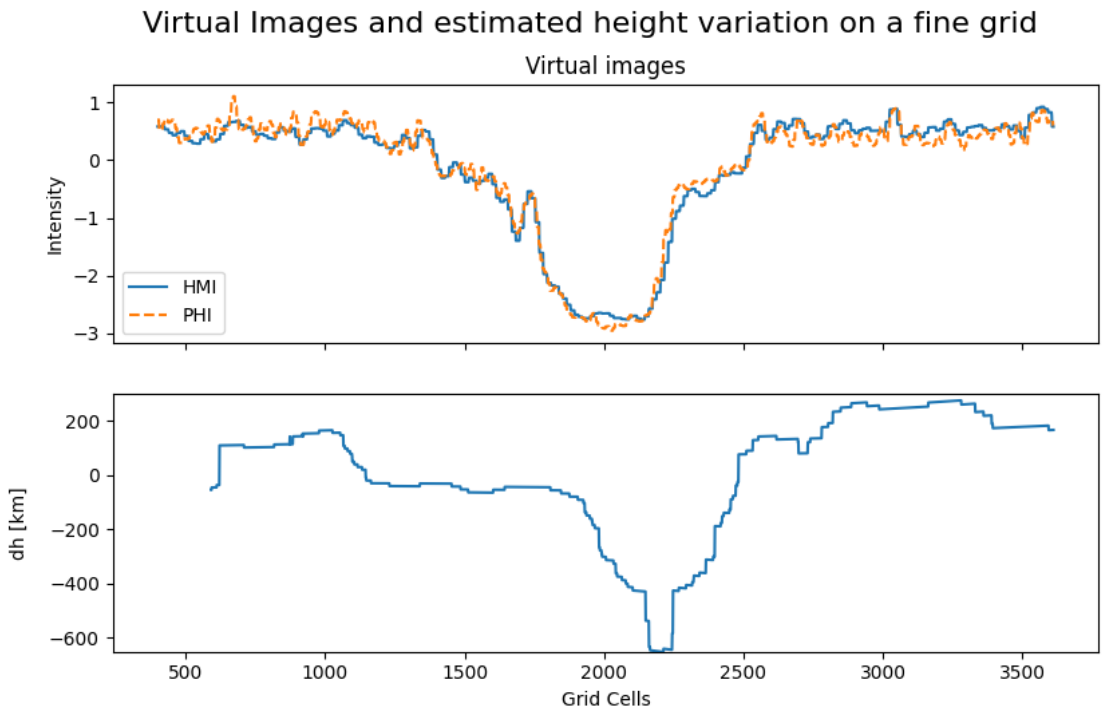

Figure 4.30: VIPs (top) and reconstructed dh (bottom) corresponding to the epipolar profile of Fig. 4.18 using a grid size of $\Delta\varphi = 0.0025° \simeq 30$ km.

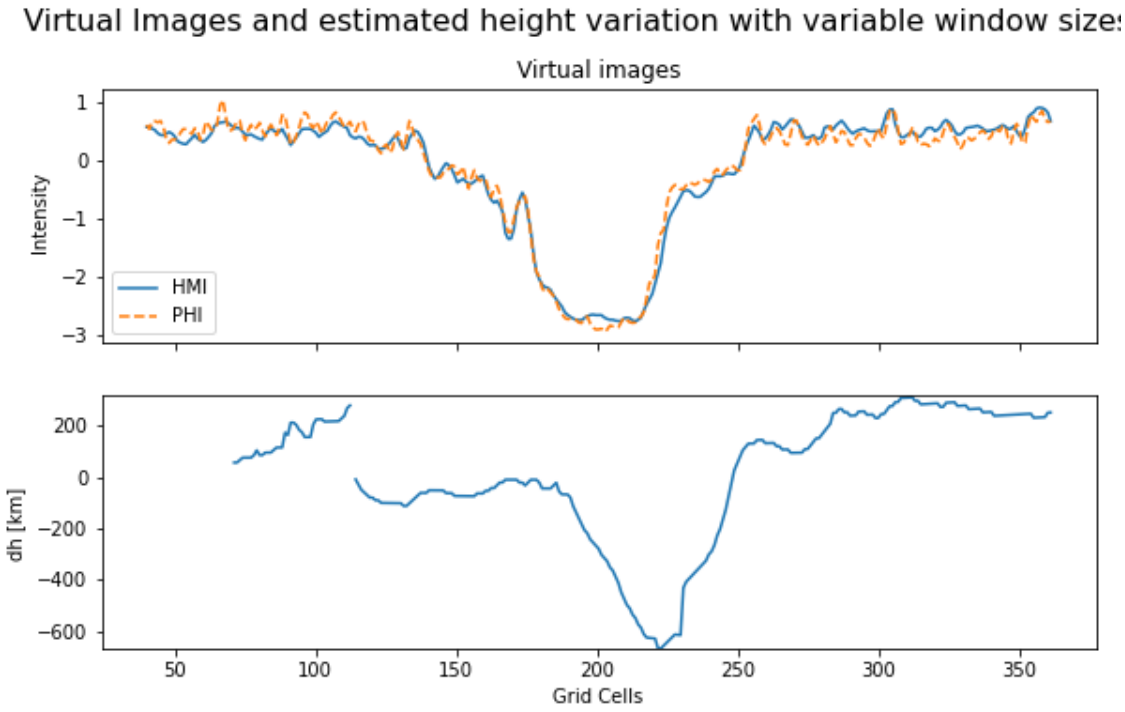

Figure 4.32: VIPs (top) and reconstructed dh (bottom) corresponding to the epipolar profile of Fig. 4.18 using a variable window size.

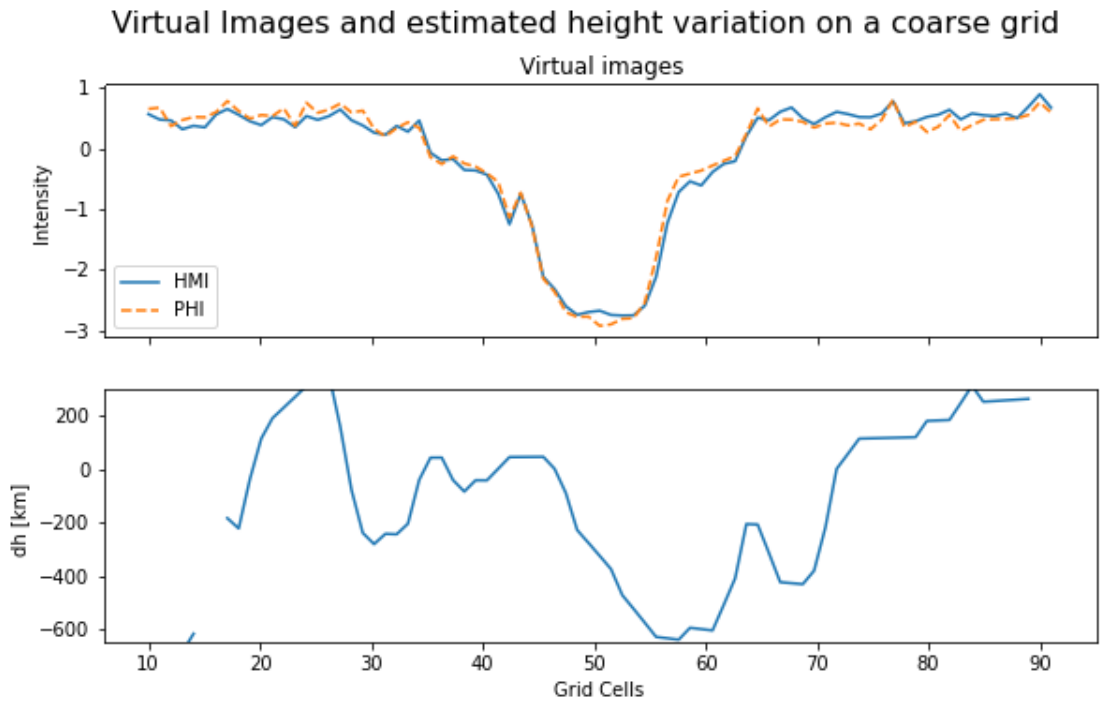

Figure 4.31: VIPs (top) and reconstructed dh (bottom) corresponding to the epipolar profile of Fig. 4.18 using a grid size of $\Delta\varphi = 0.1° \simeq 1165$ km.

Figure 4.32 presents the reconstructed height variations for the standard grid size of figure 4.18, but instead of keeping the window size constant, as for figure 4.29, here the window size is varied, and the selected height is that for which the correlation is highest, within all the half window width range between 15 and 40 grid points (see Figure 4.22).

Using a coarser grid results in a reconstructed height with many irregular fluctuations. On the other hand, using a finer grid or a variable window take much longer computation times, and does not yield a reconstructed height that can be considered better than that of figure 4.29. For this reason, the grid spacing of $\Delta\varphi = 0.0025°$ and a half window width of 40 grid points is a good choice and will be used for the stereoscopic analysis of different epipolar profiles for this particular observations. For other observations, these parameters will have to be adjusted.

Testing the Same Profile Observed 8 Minutes Earlier

To test the consistency in the performance of the method we applied it to observations of the same sunspot but obtained 8 minutes before. The parameters were the same as those used for Fig. 4.29: the grid was centered at the same position within the sunspot, the grid half window width sizes are the same, and the correction to the CDELT value was as well the same. The estimated height is presented in Fig. 4.33.

The height estimates of the sunspot from the observations at 06:35 UT earlier are plotted on top of the results of Fig. 4.29, from observations made at 06:43 UT. The geometrical mean error (see Eq. 2.15) is of ± 190 km at the center of the spot and is plotted as a shaded belt around the results from the original observations. The results from the earlier observations are plotted on top in black, and fall within

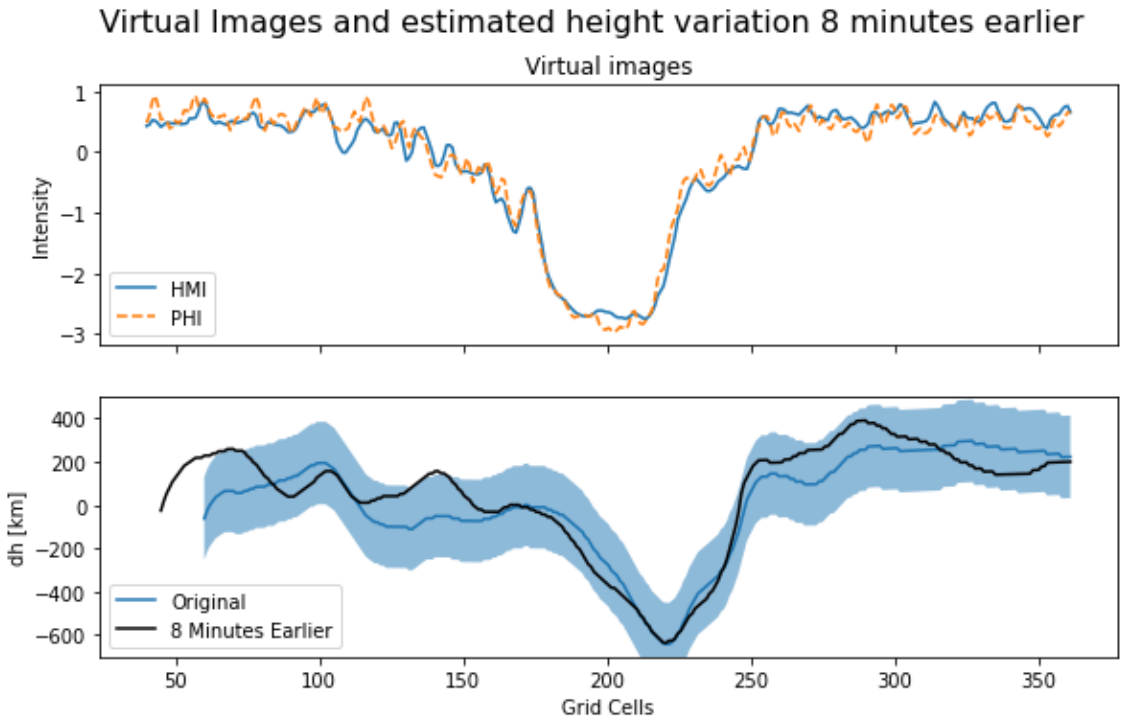

Figure 4.33: VIPs (top) and reconstructed dh (bottom) corresponding to the epipolar profile of Fig. 4.18 in blue and from observations made 8 minutes earlier in black. The blue shaded area marks the range of $\pm\frac{1}{4}h_{th} \approx 190$ km.

the error range in most of the curve. Due to the evolution of the sunspot, a perfect agreement between the two height estimates cannot be expected. This is particularly valid in the left-side penumbra (see Fig. 4.16 at $t'_y \approx 0.00325$) and the quiet Sun areas around the sunspot. Since the results are similar enough, particularly in the umbra of the sunspot, we can consider that the performance of the method is consistent throughout different observations.

Extending the Test to Other Epipolar Profiles

The correlation method was applied to four more epipolar profiles in order to test if the method performs consistently throughout the sunspot. All the four tests were performed with a grid spacing of $\Delta\varphi = 0.025°$ and a half window width of 40 grid points. The selected epipolar profiles are displayed in figure 4.34. The images are zoomed onto the sunspot, so that it is clear where each grid intersects the sunspot. The corresponding VIPs and height variation estimates are presented in figures 4.35, 4.36, 4.37, 4.38

All the reconstructed height variation curves present a 'higher' plateau region in the quiet Sun, and the deepest visible layers close to the center of the umbra. The quiet Sun is consistently at a height between 200 and 400 km, while the center of the umbra at around -600 to 750 km, for which the Wilson depression of this sunspot can be estimated to be of about 800 km, even though the range goes up to around 1000 km.

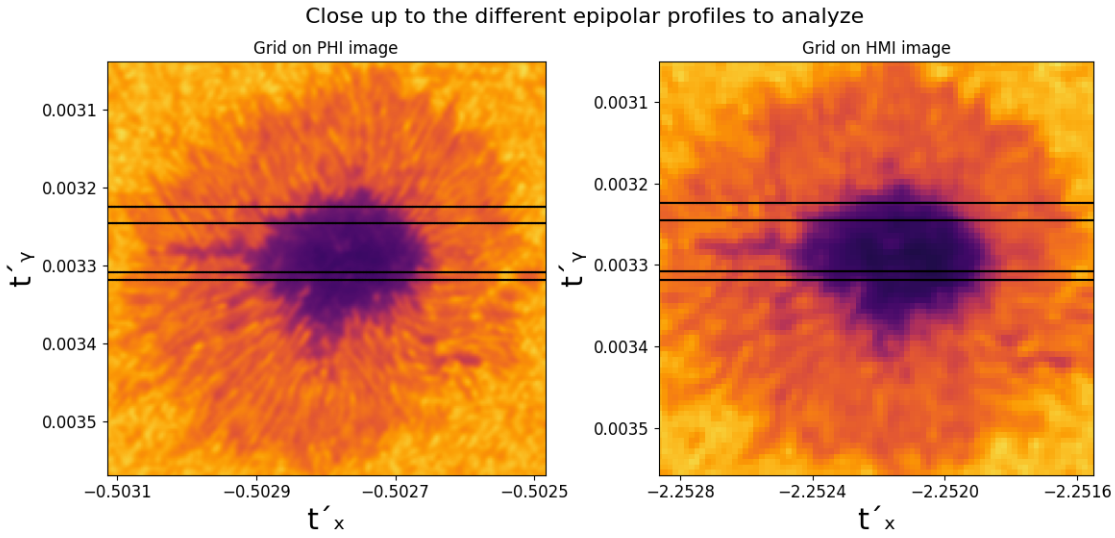

Figure 4.34: Close up to the sunspot in the SO/PHI and SDO/HMI observations. The horizontal lines are the grids to produce the VIPs at each corresponding epipolar profile.

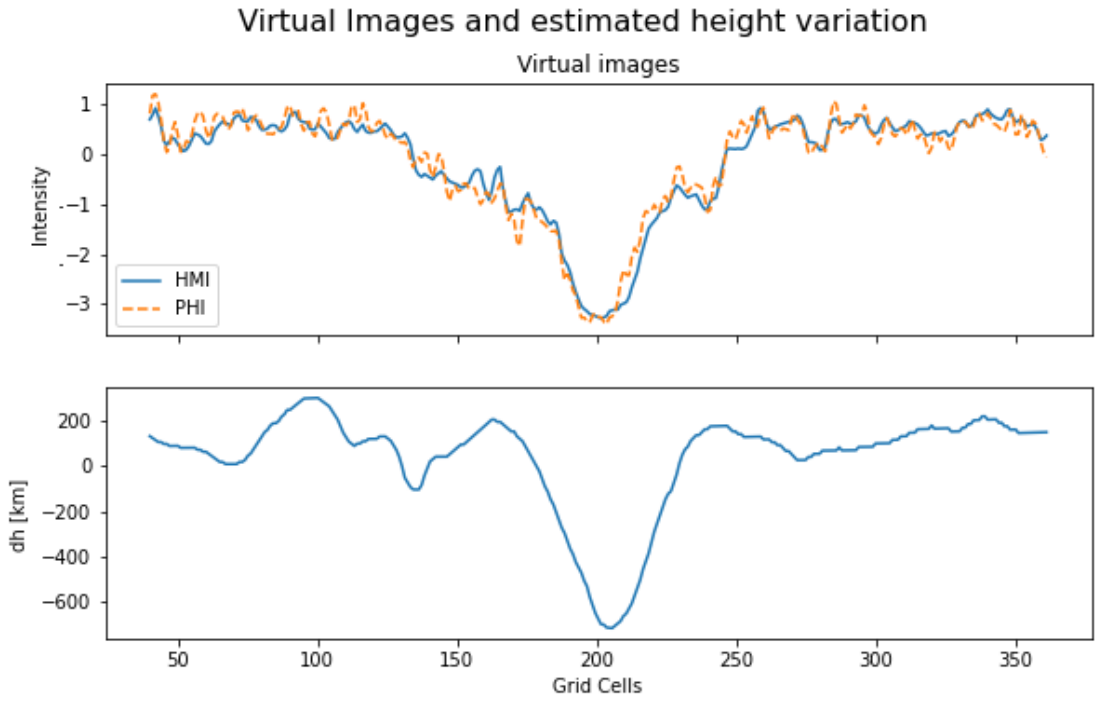

Figure 4.35: VIPs (top) and reconstructed dh (bottom) corresponding to the first epipolar profile from top to bottom displayed in Fig. 4.34

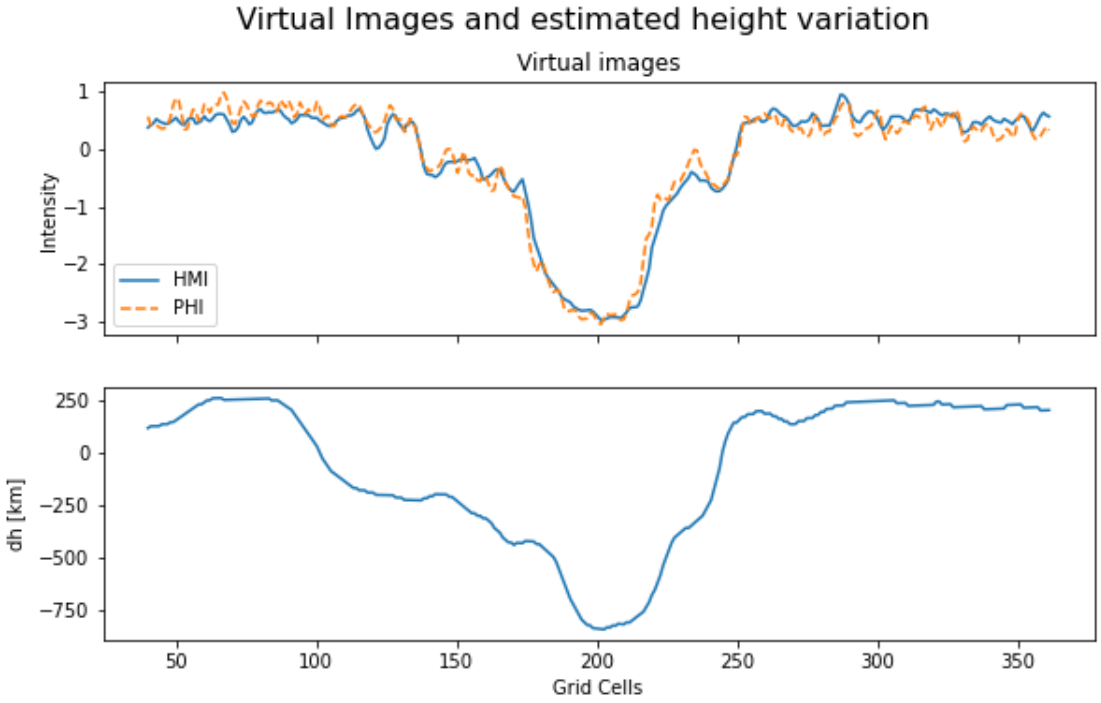

Figure 4.36: VIPs (top) and reconstructed dh (bottom) corresponding to the second epipolar profile from top to bottom displayed in Fig. 4.34

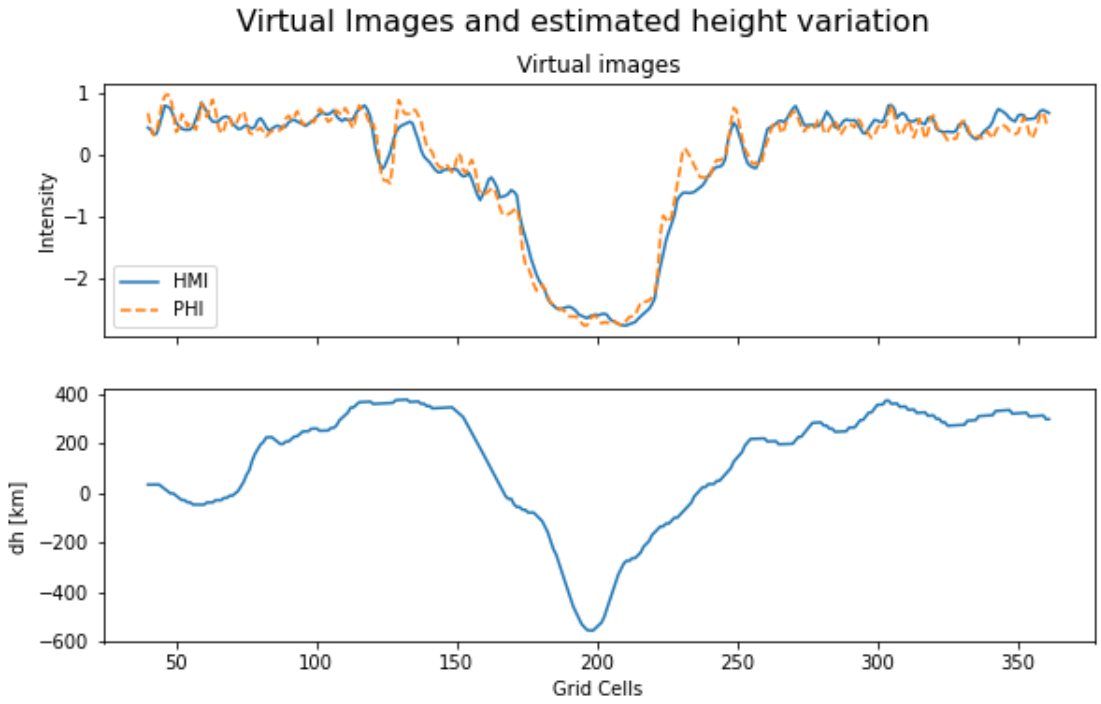

Figure 4.37: VIPs (top) and reconstructed dh (bottom) corresponding to the third epipolar profile from top to bottom displayed in Fig. 4.34.

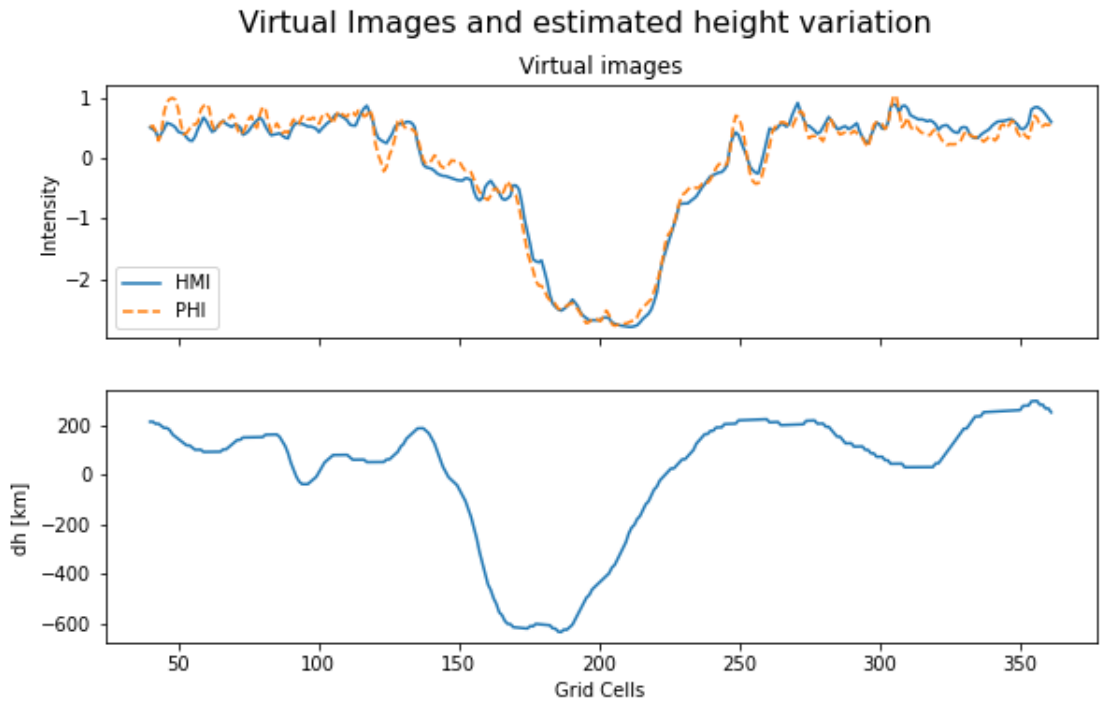

Figure 4.38: VIPs (top) and reconstructed dh (bottom) corresponding to the fourth epipolar profile from top to bottom displayed in Fig. 4.34

An offset is present in all the resulting curves, including those for the quiet Sun, where the base level is always estimated above the zero level by a couple of hundred kilometers, but this offset is consistent throughout all of the results, and therefore not relevant if the depth of the Wilson depression is estimated by the difference between the quiet Sun and the center of the umbra. Another effect that appears throughout the results is that there are height variations on a scale that is smaller than the scale of the Wilson depression, but are still of the order of a couple hundred kilometers. This effect will be further discussed in the next section, as well as possible ways to reduce it. The last consistent effect in the results, and related to the one mentioned before, is that the quiet Sun level is always much better reproduced on the right side of the profiles, while on the left side there are always more irregular height variations. There is also a general horizontal offset between the minimum in the intensity profiles and the minimum dh in the umbra of the sunspot. The results obtained with this method estimate the Wilson depression to be roughly 800 km.

4.2.1 Full 2D Height Map

Similarly to Section 3.3.6, a 2D map was produced to visualize the height variation on a surface. This 2D map was produced by analyzing epipolar profiles with a separation of $\Delta\varepsilon \approx \Delta t'_y \approx 5 \times 10^{-6}$, corresponding to roughly 300 km. Each profile was analyzed using the same parameters as for figure 4.29.

The top panel of Fig. 4.39 displays the FOV that was analyzed, and the results are shown on the bottom panel. The contours of the umbra, the penumbra and a

few pores taken from the intensity image are plotted onto the results to visualize the position on the surface on which the height variations are estimated. To reduce the number of outliers, a condition was set for the results, so that only the dh values for which the correlation was higher than a threshold of $\mathcal{C} \geq 0.995$ were considered. Regions where the correlation value was lower were left empty and are displayed in white in the figure. The projection on the top and bottom panels of Fig. 4.39 are different because the horizontal coordinates on the top panel are rectified homogeneous coordinates (t'_x), while those in the 2D map are azimutal (φ).

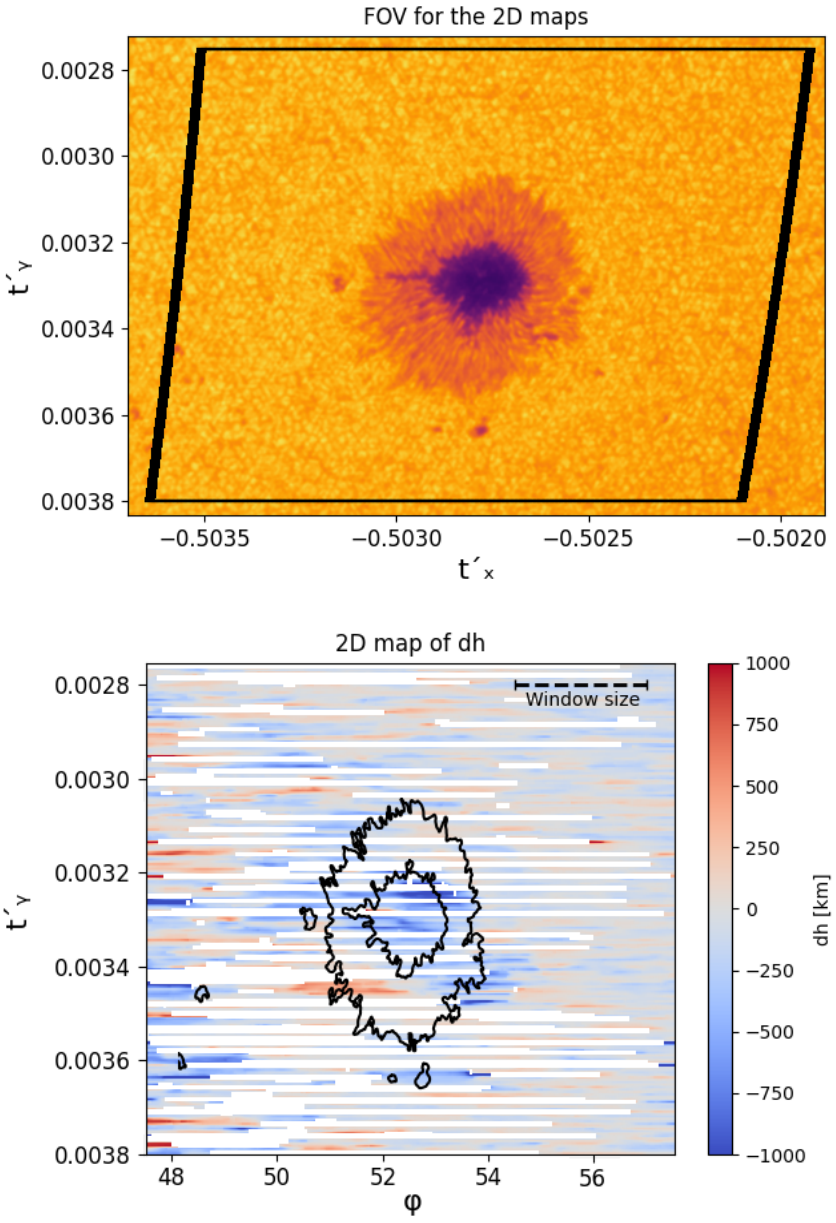

Figure 4.39: 2D colormap (bottom) of the height variations within the FOV of the top diagram. On top of the results are plotted the intensity contours to the umbra, penumbra and a few pores. The dashed line (upper right corner of the bottom panel) indicates the width of the window.

The results from figure 4.39 show that in the umbra of the sunspot, as well as in some of the pores, the dh estimates are deepest. However, even though the position

of these large negative dh estimates agrees with the position of the visual sunspot contours, the size of the reconstructed structures appears much larger in the results.

To test if the reproduced width of the structures in the results is due to the window size, we convolved the original image with the same window, and obtained the contours for the umbra, the penumbra and one of the pores. This is displayed in Fig. 4.40 The other pores were too small and they are no longer visible after the convolution. Plotting these contours in a 2D map shows that the width of the umbra of the sunspot and of the pore are similar to the width of the structures after convolving the image with the window. Some of the other pores are not visible after the convolution, so their contours are not plotted on top of the reproduced results.

With the previous results it can be considered that the umbra of sunspots and pores can be reproduced with the method developed in this work. The dh value of these structures is of the order of -500 to -1000 km. The width of the reproduced structures is comparable to the width of the window size used.

4.3 Summary and Discussion

In the previous sections we demonstrated that the correlation method could be applied to real observations from SO/PHI and SDO/HMI. Performing a stereoscopic analysis was possible even though the data set was obtained from completely different instruments with different resolution and views from points with different distances to the Sun.

The results obtained with this method seem promising to estimate the Wilson depression. The obtained results fall within the range of previous observational studies by Prokakis (1974), which estimate the Wilson depression within a range of 690 to 2100 km. More precise Wilson depression estimates from indirect methods are those of Martínez Pillet and Vázquez (1993), Solanki et al. (1993), and Löptien et al. (2020), who estimate a Wilson depression of ≈600 km, ≈400 km, and 500-700 km, respectively. The Wilson depression estimates from Figs. 4.29, and Figs. 4.35 to 4.38 are of roughly 800 km, which is slightly larger than the estimates previously obtained for different sunspots. However, the results of the 2D map of figures 4.39 and 4.40 give a range for the Wilson depression of -500 to -1000 km, so that previous estimates also fall within this range. The difference in the results obtained here and previous results could be also due to differences in the methods or to real depth differences between different sunspots, to differences in size, magnetic field strength, etc.

Applying the method to real data turned out to be more complicated than with the test data. In order to be able to use the SO/PHI observations, some additional work previous to the rectification and analysis had to be conducted. The WCS header entries of the SO/PHI images need to be adjusted. A short iterative algorithm was created for this purpose, after which the WCS header entries of the SO/PHI images were fixed and the results of the rectification were precise to an order of one image pixel, which is a level of precision required for this particular analysis.

Once the header entries for SO/PHI were fixed, the results showed a linear upward trend in the reconstructed height, probably given by an inaccurate `CDELT` value in the SO/PHI image header, and possibly also to an optical distortion. This value was as well adjusted and the trend in the results was removed. The procedure for this correction was not included in this work because it consisted only in trying with

different values until each reconstructed height profile of the quiet Sun appeared flat on large scales. For this reason the corrected CDELT value is only an estimate. Adjustments of this value, as well as other header entries corrections, for any given pair of combined observations of SO/PHI and other instrument might be necessary.

On the large scale, the correlation method yields a height level for the quiet Sun, and one for the umbra of the sunspot. Smaller scale height variations of the order of a few hundreds of km appear throughout all of the results. It can be seen in the VIPs, that in many of the regions where these irregular fluctuations appear, the structures present in the VIPs are unsimilar, so that the correlation method gives a wrong estimate by correlating unrelated structures. However, these irregularities in the results are of the order of the size of one SO/PHI pixel, and smaller than that of one SDO/HMI pixel, so that the precision of the results is limited to the image pixel size and fluctuations with periods smaller than that size are to be expected. It is also worth mentioning that the magnitude of the Wilson depression is of the order of just a couple of pixels, so that the accuracy of the results is comparable and limited by the spatial resolution of the currently available data. The theoretically resolvable range (see Eq. 2.15) at the center of the sunspot is is ± 383 km, giving a mean uncertainty for our height estimates of ± 190 km. Further random errors introduced during the resampling for rectification and correlation can be expected to scale also with the pixel resolution and are probably of similar magnitude.

There are three main possibilities for these differences in the VIPs. The first one is a consequence of the fact that the line of sight is different for each one of the spacecraft, especially in inclined areas where the line of sight is very different. These differences in line of sight give small scale differences between the images, e.g. due to radiative transfer effects, in addition to the disparity of features, that is the key difference between images used in stereoscopy.

Another possible explanation is the limited resolution of the images. Since in Section 3.3.7 it was seen that for resolutions of the order of hundreds of km, the only quantity that could be retrieved from this analysis is the Wilson depression, whereas other smaller scale height fluctuations cannot be retrieved by this method. Not only that, but the difference in resolution from SO/PHI and SDO/HMI is large, so that the smaller scale structures, such as fine structure in the penumbra or the granules in the quiet Sun, are observed in more detail by SO/PHI than by SDO/HMI, resulting in VIPs with different levels of detail, which induce numerical errors in the correlation procedure. Another possible explanation for the differences in the VIPs is noise in the data. There is an intrinsic level of noise for the observations, but errors induced in the image pixel discretization, the interpolation induced by the rectification and the integration of the observations into the VIPs can also result in noise in the data.

A consequence of the resolution of the data is that the structures tend to be reproduced wider than they are. This effect was seen in Chapter 2, Section 3.3.7, where the test images were degraded to a resolution similar to the resolution that real observations have. For the given resolution of the images, this effect is also present in the results, so that the shape of the features cannot be well reproduced but the Wilson depression can be estimated if the difference between the quiet Sun level and the umbra is calculated. The width of the reproduced structures is directly related to the size of the window used for the correlation. Using higher resolution data will allow to use smaller windows, or at least the size of the window will be smaller

with respect to the size of structures in the images, and therefore the reproduced structure will have a more realistic size.

The last possible explanation for the unreliable fluctuations in the results could be distortion in the images. The observations of both images have been corrected for distortion, but there is the possibility that a residual distortion is still present in the images. This could yield differences in the rectification of the images and therefore in not scanning the exact same epipolar line in both images, resulting in small scale differences between both VIPs. Another possible effect due to a distortion in the images is the horizontal offset between the minimum intensity in the VIPs and the position of the minimum dh in the umbra of the spot, since the direction of this offset changes uniformly throughout the different epipolar profiles in the FOV.

Most likely, the irregularities in the results arise from a combination of the effects mentioned above. However, the relevant feature to be determined, the Wilson depression, was reproduced. As well as with the test data, there is a general offset of the base level, so that only relative heights can be estimated with this method. Adding an error number, or a parameter that indicates if the reconstructed height is reliable at each point would be of advantage, and will be included in any further work on which this stereoscopic method is applied.

Given that there are still a number of issues in the data that need to be fixed, the results obtained with this method are not final yet, but they show that the method is promising in estimating the Wilson depression in the umbra of sunspots and pores.

The correlation method yields reliable results, but they are limited by the quality of the observations available. Analyzing a larger number of combined observations is necessary in order to really assess the capabilities of this method and how much the results are affected by the method limitations, and how much to external effects, like the resolution and noise (as discussed in Chapter 3), it is to be expected that with higher resolution observations, the reliability as well as the level of detail reproduced with this method will increase.

Lastly, it is worth mentioning that given the way the VIPs are produced is different between the test and the real data, applying the optimization method to the real data would require further modifications, which are out of the scope of this work. Future work could consist in adapting the optimization method to the way the VIPs of the real data are produced, in order to further improve the results obtained by the correlation method.

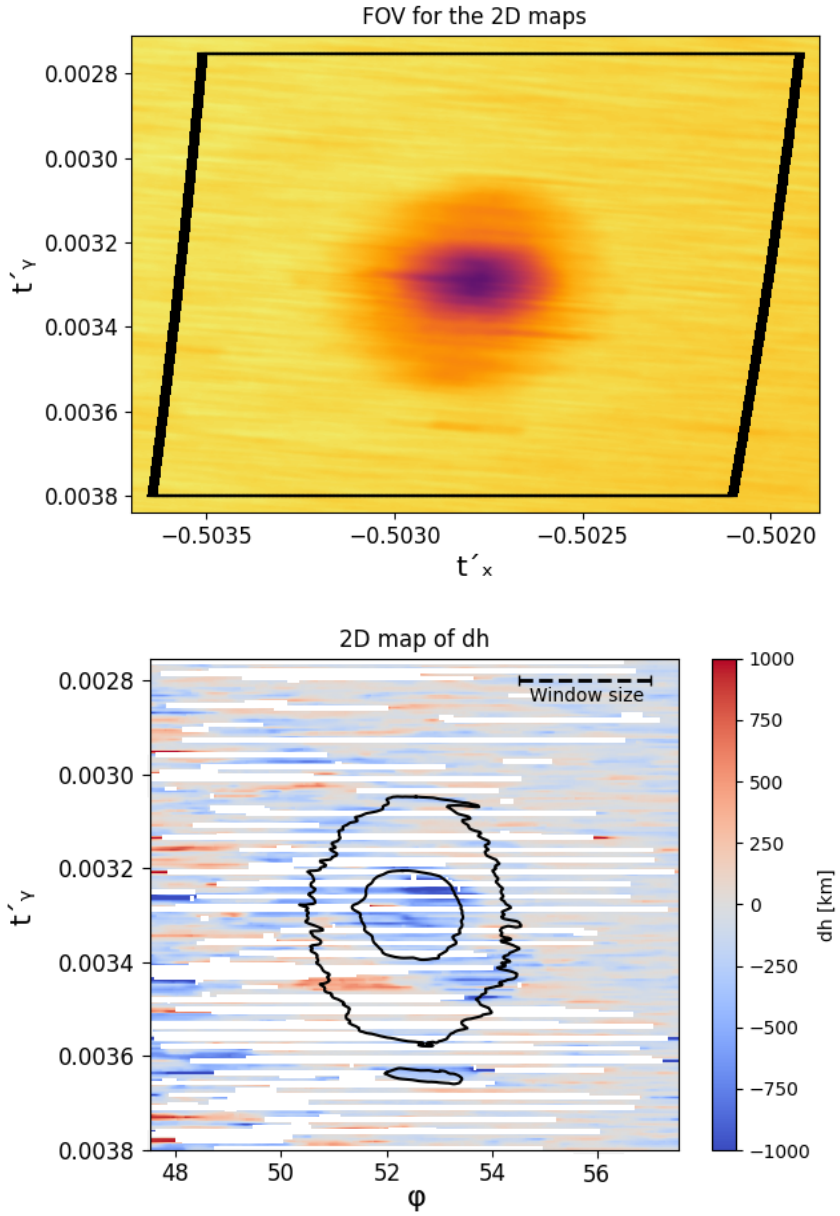

Figure 4.40: 2D colormap (bottom) of the height variations within the FOV of the top diagram. On top of the results are plotted the intensity contours to the umbra, penumbra and a few pores. The dashed line (upper right corner of the bottom panel) represents the width of the window. The horizontal axis in the top diagram is t'_x, while that on the 2D map is the azimuthal coordinate φ. This change of coordinates is to avoid the oblique projection in normalized coordinates as seen in the left diagram.

Chapter 5

Conclusions

A stereoscopic method for the study of height variations in the solar photospohere, more specifically the Wilson depression, was developed. The method is based on the correlation of the brightnesses (VIPs) along epipolar profiles. From the best shift of the VIPs we find the height variations along the epipolar lines.

The method was first tested on synthetic data and then applied to real observations. The method is reliable in estimating large scale height variations, such as the Wilson depression. Even though the results are limited by inaccuracies in the data, as well as the current resolution available in the observation, the method yields reliable results.

The resolution of the images is the biggest limiting factor for the results. At the current resolution of the observations, the disparity in the umbra is of the order of two pixels. As discussed in Chapter 2, if the disparity is 0, then the object is at infinity or at a distance larger than what can be distinguished with the given resolution. Therefore it is to be expected that for higher resolution images the results will improve considerably, and even smaller scale height variations will be reproduced with some accuracy.

At the current resolution of the available observations, the structures are reproduced wider than they are, but the estimate of the Wilson depression in sunspots obtained with this method, for synthetic and for real observations agrees with previous estimates (see discussion of Chapters 3 and 4). It is also to be expected, that with higher resolution observations, the 3D structure within sunspots, as well as heigh variations on the quiet Sun, could be measured.

Given that the size of the reproduced structures is of the same order as the image resolution and the method can still reproduce the Wilson depression of sunspots, our method seems like a very promising tool to study photospheric surface height variations, and it's performance will improve significantly if higher resolution images become available.

When one of the viewing angles approaches the slope of the sunspot on its near side, information on that slope is lost by this camera, and therefore some inaccuracies arise concerning the height estimates of that slope. This must be considered when the results are analyzed. It can be expected that this effect will be present in the results if the viewing angles exceed $\gamma = 30°$, according to the tests performed.

For this work, observations of sunspots on three different days were available. However, for the stereoscopic analysis only the observations of one day, October 29th of 2002, could be used. The observations of March 3rd of 2022 were made

with a spacecraft separation angle of about $6°$. This separation is too small for a stereoscopic analysis as discussed in Chapter 3, Section 3.3.3. In the observations of March 17th of 2022, the sunspot appears too close to the limb in the observation from SDO/HMI, which decreases the resolution and induces some distortion in the observations. Also, both spacecraft observed the sunspot from the same side, which in principle still allows for a stereoscopic analysis, but information on the near slope of the sunspot is lost for both cameras. Therefore having multiple observations does not mean that all of them are suitable for this stereoscopic analysis.

5.1 Outlook

Considering that the method as presented here is reliable for stereoscopic analysis of height variations on the solar surface, some improvement can still be made. First of all implementing a measure of the error or of the reliability of the estimate on each point of the profile would help assess the quality of the work in a systematic way, so that one can know where the estimates are more reliable and where they are not. Naturally, applying the method to more observations will also give a better idea of how reliable the results are.

Possible improvements for the method include reducing the number of outliers in the results by studying in depth the effect on the results that different window sizes with respect to the resolution of the data have. Expanding the method to include the optimization procedure to improve the obtained height vector is also a possible improvement for this method that could yield better results.

If the performance of this method is good and consistent throughout different combined observations, then it can be applied not only to estimate the Wilson depression, but also to use these estimates for other scientific studies. For example, equation (1.21) can be used to estimate the curvature force within sunspots (Martínez Pillet & Vázquez, 1993) from the Wilson depression. With more observations are available, more sunspots can be studied and therefore, both the reliability of this method and the Wilson depression of sunspots can be further studied.

The height variations can be estimated only in the spatial direction of the epipolar profile. Under the assumption of a radial variation of height within sunspots, it can be extended to other parts of the sunspot (Solanki et al., 1993). Another way to have information on more than one direction would be to perform the analysis on the same sunspot but with three observing cameras, which would yield three mutual epipolar planes and therefore height variations along three epipolar directions. However, this possibility is currently not available, as no other instrument observes the Sun at high resolution in the visible spectral range outside the Sun-Earth line besides SO/PHI.

An extension and application of the method here described is to stereoscopically determine and compare the height at different wavelengths. This is particularly interesting when considering the core of a spectral line in addition to the continuum observations presented here. This will allow comparing the line formation height in different solar features and may allow constraining the temperature gradient.

Another extension of this work consists in analysing multiple sunspots in order to perform a statistical analysis of the relation of the Wilson depression with the size, the curvature, or the magnetic field strength; or to use the Wilson depression measurements to improve other sunspot models (e.g. Rempel, 2014).

As said before, the availability of higher resolution observations will improve the results obtained with this method. Current observations of sunspots of SO/PHI combined with observations of e.g. HINODE (Kosugi et al., 2007), could already improve the results; and the availability of more observations of more sunspots will not only help to better assess its performance, but it will also allow to conduct scientific studies where the Wilson depression or other height variations in the photosphere will play an important role.

Bibliography

Aschwanden, M. J. (2011). Solar stereoscopy and tomography. *Living Reviews in Solar Physics*, *8*(1), 1–96.

Aschwanden, M. J., Lim, J., Gary, D. E., & Klimchuk, J. A. (1995). Solar rotation stereoscopy in microwaves. *Astrophysical Journal v. 454, p. 512*, *454*, 512.

Aschwanden, M. J., White, S., & Bastian, T. (1992). 3d reconstruction methods of coronal structures by radio observations. *Coronal Streamers, Coronal Loops, and Coronal and Solar Wind Composition*, *348*, 217–220.

Aschwanden, M. J., & Wülser, J.-P. (2011). 3-d reconstruction of active regions with stereo. *Journal of Atmospheric and Solar-Terrestrial physics*, *73*(10), 1082–1095.

Beckers, J. M., & Milkey, R. W. (1975). The line response function of stellar atmospheres and the effective depth of line formation. *Solar Physics*, *43*, 289–292.

Berton, R., & Sakurai, T. (1985). Stereoscopic determination of the three-dimensional geometry of coronal magnetic loops. *Solar physics*, *96*, 93–111.

Bray, R. J., Loughhead, R. E., & Durrant, C. J. (2009). The solar granulation. *The Solar Granulation*.

Carlsson, M., Stein, R. F., Nordlund, Å., & Scharmer, G. B. (2004). Observational Manifestations of Solar Magnetoconvection: Center-to-Limb Variation. *Astrophysical Journal Letters*, *610*, L137–L140. https://doi.org/10.1086/423305

Caroubalos, C., & Steinberg, J. L. (1974). Evidence of Solar Burst Directivity at 169 MHz from Simultaneous Ground Based and Deep Space Observations (STEREO-1 Preliminary Results). *Astronomy and Astrophysics*, *32*, 245.

Del Toro Iniesta, J. C. (2003). *Introduction to Spectropolarimetry*. Cambridge, UK: Cambridge University Press.

Faugeras, O. (1993). *Three-dimensional Computer Vision: a Geometric Viewpoint*. MIT Press, Cambridge, Massachusets, USA.

Foullon, C. Automated detection and 3D reconstruction of EUV prominences (A. Wilson, Ed.). In: *Solar variability as an input to the earth's environment* (A. Wilson, Ed.). Ed. by Wilson, A. *535*. ESA Special Publication. 2003, September, 477–482.

Frutiger, C., Solanki, S. K., Fligge, M., & Bruls, J. H. M. J. (2000). Properties of the solar granulation obtained from the inversion of low spatial resolution spectra. *Astronomy and Astrophysics*, *358*, 1109–1121.

Fusiello, A., Trucco, E., & Verri, A. (2000). A compact algorithm for rectification of stereo pairs. *Machine Vision Applications*, *12*, 16–20.

Gandorfer, A., Grauf, B., Staub, J., Bischoff, J., Woch, J., Hirzberger, J., Solanki, S., Álvarez-Herrero, A., García Parejo, W., P.and Schmidt, Volkmer, R., Appourchaux, T., & del Toro Iniesta, J. The High Resolution Telescope (HRT) of the Polarimetric and Helioseismic Imager (PHI) onboard Solar Orbiter. In: In *Space telescopes and instrumentation 2018: Optical, infrared, and millimeter wave*.

10698. Proceedings of the SPIE. 2018, 106984N. https://doi.org/10.1117/12.2311816.

Gandorfer, A., Solanki, S. K., Woch, J., Martínez Pillet, V., Álvarez Herrero, A., & Appourchaux, T. (2011). The Solar Orbiter Mission and its Polarimetric and Helioseismic Imager (SO/PHI). *GONG-SoHO 24: A New Era of Seismology of the Sun and Solar-Like Stars*, *271*(1), Article 012086, 012086. https://doi.org/10.1088/1742-6596/271/1/012086

Gokhale, M., & Zwaan, C. (1972). The structure of sunspots: I: Observational constraints; current sheet models. *Solar Physics*, *26*, 52–75.

Gray, D. F. (2021). *The observation and analysis of stellar photospheres*. Cambridge University Press.

Greisen, E., & Calabretta, M. (2002). Representations of world coordinates in FITS. *Astronomy and Astrophysics*, *395*, 1061–1075.

Hartley, R. I., & Zisserman, A. (2004). *Multiple view geometry in computer vision* (Second). Cambridge University Press.

Hirzberger, J., Feller, A., Riethmüller, T. L., Schüssler, M., Borrero, J. M., Afram, N., Unruh, Y. C., Berdyugina, S. V., Gandorfer, A., Solanki, S. K., Barthol, P., Bonet, J. A., Martínez Pillet, V., Berkefeld, T., Knölker, M., Schmidt, W., & Title, A. M. (2010). Quiet-sun Intensity Contrasts in the Near-ultraviolet as Measured from SUNRISE. *Astrophysical Journal Letters*, *723*(2), L154–L158. https://doi.org/10.1088/2041-8205/723/2/L154

Hurlburt, N. E., Martens, P. C., Slater, G. L., & Jaffey, S. M. Volume reconstruction of magnetic fields using solar imagery. (1994). In: *Solar Active Region Evolution: Comparing Models with Observations (Balasubramaniam, K. S. and Simon, G. W. Eds.), Astronomical Society of the Pacific Conference Series, Vol. 68*. 1994, 30.

Inhester, B. (2006). Stereoscopy basics for the STEREO mission. *arXiv preprint astro-ph/0612649*.

Kane, S. R. (1981). Multi-Spacecraft Observations of Solar Hard X-Ray Bursts. *Astrophysics and Space Science*, *75*(1), 163–179. https://doi.org/10.1007/BF00651393

Keller, C. U., Schüssler, M., Vögler, A., & Zakharov, V. (2004). On the Origin of Solar Faculae. *Astrophysical Journal Letters*, *607*, L59–L62. https://doi.org/10.1086/421553

Kopp, G., & Rabin, D. (1992). A Relation Between Magnetic Field Strength and Temperature in Sunspots. *Solar Physics*, *141*(2), 253–265. https://doi.org/10.1007/BF00155178

Kosugi, T., Matsuzaki, K., Sakao, T., Shimizu, T., Sone, Y., Tachikawa, S., Hashimoto, T., Minesugi, K., Ohnishi, A., Yamada, T., Tsuneta, S., Hara, H., Ichimoto, K., Suematsu, Y., Shimojo, M., Watanabe, T., Shimada, S., Davis, J. M., Hill, L. D., … Golub, L. (2007). The Hinode (Solar-B) Mission: An Overview. *Solar Physics*, *243*, 3–17. https://doi.org/10.1007/s11207-007-9014-6

Koutchmy, S., & Molodenskii, M. M. (1992). Three-dimensional image of the solar corona from white-light observations of the 1991 eclipse. *Nature*, *360*(6406), 717–719. https://doi.org/10.1038/360717a0

Landi Degl'Innocenti, E., & Landi Degl'Innocenti, M. (1977). Response function for magnetic lines. *Astronomy and Astrophysics*, *56*, 111–115.

Livingston, W. (2002). Sunspots Observed to Physically Weaken in 2000-2001. *Solar Physics*, *207*(1), 41–45. https://doi.org/10.1023/A:1015555000456

Löptien, B., Lagg, A., van Noort, M., & Solanki, S. K. (2020). Connecting the Wilson depression to the magnetic field of sunspots. *Astronomy and Astrophysics, 635*, Article A202, A202. https://doi.org/10.1051/0004-6361/201936975

Löptien, B., Lagg, A., van Noort, M., & Solanki, S. K. (2018). Measuring the Wilson depression of sunspots using the divergence-free condition of the magnetic field vector. *Astronomy and Astrophysics, 619*, Article A42, A42. https://doi.org/10.1051/0004-6361/201833571

Magain, P. (1986). Contribution functions and the depths of formation of spectral lines. *Astronomy and Astrophysics, 163*.

Maltby, P. (1977). On the difference in darkness between sunspots. *Solar Physics, 55*(2), 335–346. https://doi.org/10.1007/BF00152577

Martínez Pillet, V., & Vázquez, M. (1993). The continuum intensity-magnetic field relation in sunspot umbrae. *Astronomy and Astrophysics, 270*, 494–508.

Mathew, S. K., Solanki, S. K., Lagg, A., Collados, M., Borrero, J. M., & Berdyugina, S. (2004). Thermal-magnetic relation in a sunspot and a map of its Wilson depression. *Astronomy and Astrophysics, 422*, 693–701. https://doi.org/10.1051/0004-6361:20040136

Maunder, E. W. (1903). Spoerer's law of zones. *The Observatory, 26*, 329–330.

Meyer, F., Schmidt, H. U., & Weiss, N. O. (1977). The stability of sunspots. *Monthly Notices of the RAS, 179*, 741–761. https://doi.org/10.1093/mnras/179.4.741

Meyer, F, Schmidt, H., Weiss, N., & Wilson, P. (1974). The growth and decay of sunspots. *Monthly Notices of the Royal Astronomical Society, 169*(1), 35–57.

Müller, D., St. Cyr, O. C., Zouganelis, I., Gilbert, H. R., Marsden, R., Nieves-Chinchilla, T., Antonucci, E., Auchère, F., Berghmans, D., Horbury, T. S., Howard, R. A., Krucker, S., Maksimovic, M., Owen, C. J., Rochus, P., Rodriguez-Pacheco, J., Romoli, M., Solanki, S. K., Bruno, R., … Williams, D. (2020). The Solar Orbiter mission. Science overview. *Astronomy and Astrophysics, 642*, Article A1, A1. https://doi.org/10.1051/0004-6361/202038467

Murray, S. A. (2013). Fields and flares: Understanding the complex magnetic topologies of solar active regions. *arXiv preprint arXiv:1301.5601*.

Nocedal, J., & Wright, S. J. (2006). Conjugate gradient methods. *Numerical optimization*, 101–134.

Parker, E. N. (1979). Sunspots and the physics of magnetic flux tubes. i-the general nature of the sunspot. ii-aerodynamic drag. *Astrophysical Journal, Part 1, vol. 230, June 15, 1979, p. 905-923., 230*, 905–923.

Pearson, K. (1895). Note on Regression and Inheritance in the Case of Two Parents. *Proceedings of the Royal Society of London Series I, 58*, 240–242.

Ponz, J., Thompson, R., & Munoz, J. (1994). The fits image extension. *Astronomy and Astrophysics Suppl., Vol. 105, p. 53-55 (1994), 105*, 53–55.

Priest, E. (2014a). A description of the sun. In *Magnetohydrodynamics of the sun* (pp. 1–73). Cambridge University Press. https://doi.org/10.1017/CBO9781139020732.002

Priest, E. (2014b). Magnetoconvection and sunspots. In *Magnetohydrodynamics of the sun* (pp. 306–333). Cambridge University Press. https://doi.org/10.1017/CBO9781139020732.010

Prokakis, T. (1974). The Depth of Sunspots. *Solar Physics, 35*(1), 105–110. https://doi.org/10.1007/BF00156960

Puschmann, K. G., Ruiz Cobo, B., & Martínez Pillet, V. (2010). A Geometrical Height Scale for Sunspot Penumbrae. *Astrophysical Journal, 720*(2), 1417–1431. https://doi.org/10.1088/0004-637X/720/2/1417

Rempel, M. (2014). Numerical Simulations of Quiet Sun Magnetism: On the Contribution from a Small-scale Dynamo. *Astrophysical Journal, 789*, Article 132, 132. https://doi.org/10.1088/0004-637X/789/2/132

Rezaei, R., Beck, C., Lagg, A., Borrero, J. M., Schmidt, W., & Collados, M. (2015). Variation in sunspot properties between 1999 and 2014. *Astronomy and Astrophysics, 578*, Article A43, A43. https://doi.org/10.1051/0004-6361/201425557

Riethmüller, T. L., Solanki, S. K., Barthol, P., Gandorfer, A., Gizon, L., Hirzberger, J., van Noort, M., Blanco Rodríguez, J., Del Toro Iniesta, J. C., Orozco Suárez, D., Schmidt, W., Martínez Pillet, V., & Knölker, M. (2017). A New MHD-assisted Stokes Inversion Technique. *Astrophysical Journal Supplement, 229*(1), Article 16, 16. https://doi.org/10.3847/1538-4365/aa5830

Riethmüller, T. L., Solanki, S. K., Berdyugina, S. V., Schüssler, M., Martínez Pillet, V., Feller, A., Gandorfer, A., & Hirzberger, J. (2014). Comparison of solar photospheric bright points between Sunrise observations and MHD simulations. *Astronomy and Astrophysics, 568*, Article A13, A13. https://doi.org/10.1051/0004-6361/201423892

Romero Avila, A., Inhester, B., Hirzberger, J., & Solanki, S. K. (2024). Photospheric stereoscopy: Direct estimation of solar surface-height variations. *Solar Physics, 299*(4), 41.

Ruiz Cobo, B., & del Toro Iniesta, J. C. (1994). On the sensitivity of Stokes profiles to physical quantities. *Astronomy and Astrophysics, 283*, 129–143.

Ryutova, M., Ryutova, M, & Evenson. (2015). *Physics of magnetic flux tubes* (Vol. 417). Springer.

Schad, T. A. (2014). On the Collective Magnetic Field Strength and Vector Structure of Dark Umbral Cores Measured by the Hinode Spectropolarimeter. *Solar Physics, 289*(5), 1477–1498. https://doi.org/10.1007/s11207-013-0412-7

Scherrer, P. H., Schou, J., Bush, R. I., Kosovichev, A. G., Bogart, R. S., Hoeksema, J. T., Liu, Y., Duvall, T. L., Zhao, J., Title, A. M., Schrijver, C. J., Tarbell, T. D., & Tomczyk, S. (2012). The Helioseismic and Magnetic Imager (HMI) Investigation for the Solar Dynamics Observatory (SDO). *Solar Physics, 275*, 207–227. https://doi.org/10.1007/s11207-011-9834-2

Schmidt, H. U. (1991). Sunspots. *Geophysical and Astrophysical Fluid Dynamics, 62*(1), 249–270. https://doi.org/10.1080/03091929108229136

Schou, J., Scherrer, P. H., Bush, R. I., Wachter, R., Couvidat, S., Rabello-Soares, M. C., Bogart, R. S., Hoeksema, J. T., Liu, Y., Duvall, T. L., Akin, D. J., Allard, B. A., Miles, J. W., Rairden, R., Shine, R. A., Tarbell, T. D., Title, A. M., Wolfson, C. J., Elmore, D. F., … Tomczyk, S. (2012). Design and Ground Calibration of the Helioseismic and Magnetic Imager (HMI) Instrument on the Solar Dynamics Observatory (SDO). *Solar Physics, 275*, 229–259. https://doi.org/10.1007/s11207-011-9842-2

Schüssler, M., Shelyag, S., Berdyugina, S., Vögler, A., & Solanki, S. K. (2003). Why Solar Magnetic Flux Concentrations Are Bright in Molecular Bands. *Astrophysical Journal Letters, 597*(2), L173–L176. https://doi.org/10.1086/379869

Simon, G., & Weiss, N. (1970). On the magnetic field in pores. *Solar Physics, 13*, 85–103.

Simon, G., Weiss, N., & Nye, A. (1983). Simple models for magnetic flux tubes. *Solar physics*, *87*, 65–75.

Solanki, S. K. (2003). Sunspots: An overview. *Astronomy and Astrophysics Reviews*, *11*, 153–286. https://doi.org/10.1007/s00159-003-0018-4

Solanki, S. K. (1987, June). *The Photospheric Layers of Solar Magnetic Flux Tubes* (Doctoral dissertation). ETH, Zürich, Switzerland. https://doi.org/10.3929/ethz-a-000412992

Solanki, S. K., del Toro Iniesta, J. C., Woch, J., Gandorfer, A., Hirzberger, J., Alvarez-Herrero, A., Appourchaux, T., Martínez Pillet, V., Pérez-Grande, I., Sanchis Kilders, E., Schmidt, W., Gómez Cama, J. M., Michalik, H., Deutsch, W., Fernandez-Rico, G., Grauf, B., Gizon, L., Heerlein, K., Kolleck, M., … Zouganelis, I. (2020). The Polarimetric and Helioseismic Imager on Solar Orbiter. *Astronomy and Astrophysics*, *642*, Article A11, A11. https://doi.org/10.1051/0004-6361/201935325

Solanki, S. K., del Toro Iniesta, J. C., Woch, J., Gandorfer, A., Hirzberger, J., Schmidt, W., Appourchaux, T., & Alvarez-Herrero, A. The Polarimetric and Helioseismic Imager for Solar Orbiter: SO/PHI (K. N. Nagendra, S. Bagnulo, R. Centeno, & M. Jesús Martínez González, Eds.). In: *Polarimetry* (K. N. Nagendra, S. Bagnulo, R. Centeno, & M. Jesús Martínez González, Eds.). Ed. by Nagendra, K. N., Bagnulo, S., Centeno, R., & Jesús Martínez González, M. *305*. IAU Symposium. 2015, October, 108–113. https://doi.org/10.1017/S1743921315004615. arXiv: 1502.03368 [astro-ph.SR].

Solanki, S. K., Walther, U., & Livingston, W. (1993). Infrared lines as probes of solar magnetic features. VI. The thermal-magnetic relation and Wilson depression of a simple sunspot. *Astronomy and Astrophysics*, *277*, 639.

Solanki, S. K. (2003). Sunspots: An overview. *Astronomy & Astrophysics Review*, *11*.

Solanki, S. K., Inhester, B., & Schüssler, M. (2006). The solar magnetic field. *Reports on Progress in Physics*, *69*(3), 563.

Spruit, H. C. (1976). Pressure equilibrium and energy balance of small photospheric fluxtubes. *Solar Physics*, *50*(2), 269–295. https://doi.org/10.1007/BF00155292

Spruit, H. C. (1982). The flow of heat near a starspot. *Astronomy and Astrophysics, vol. 108, no. 2, Apr. 1982, p. 356-360.*, *108*, 356–360.

Stix, M. (2004). *The sun: An introduction*. Springer Science & Business Media.

Thomas, J. H., & Weiss, N. O. (1992). Sunspots-theory & observations: Nato cambridge, 1992. *Sunspots. Theory and Observations*, *375*.

Thompson, W. T. (2006). Coordinate systems for solar image data. *Astronomy and Astrophysics*, *449*(2), 791–803. https://doi.org/10.1051/0004-6361:20054262

Trucco, E., & Verri, A. (1998). *Introductory Techniques for 3D Computer Vision*. Prentice-Hall, Upper Saddle River, New Jersey, USA.

Valori, G., Löschl, P., Stansby, D., Pariat, E., Hirzberger, J., & Chen, F. (2022). Disambiguation of Vector Magnetograms by Stereoscopic Observations from the Solar Orbiter (SO)/Polarimetric and Helioseismic Imager (PHI) and the Solar Dynamic Observatory (SDO)/Helioseismic and Magnetic Imager (HMI)., *297*(1), Article 12, 12. https://doi.org/10.1007/s11207-021-01942-x

Vögler, A., Shelyag, S., Schüssler, M., Cattaneo, F., Emonet, T., & Linde, T. (2005). Simulations of magneto-convection in the solar photosphere. Equations, methods, and results of the MURaM code. *Astronomy and Astrophysics*, *429*, 335–351. https://doi.org/10.1051/0004-6361:20041507

Watson, F. T., Penn, M. J., & Livingston, W. (2014). A Multi-instrument Analysis of Sunspot Umbrae. *Astrophysical Journal, 787*(1), Article 22, 22. https://doi.org/10.1088/0004-637X/787/1/22

Wells, D. C., & Greisen, E. W. Fits-a flexible image transport system. In: In *Image processing in astronomy*. 1979, 445.

Wilson, A. (1774). I. observations on the solar spots. *Philosophical Transactions of the Royal Society of London*, (64), 1–30.

Wilson, P., & Cannon, C. (1968). The structure of a sunspot: Iii: Observations of the wilson effect. *Solar Physics, 4*, 3–17.

Aknowledgments

I would first like to thank my supervisors Bernd Inhester and Johann Hirzberger. Bernd, thank you for the infinite patience and for sharing so much of your knowledge with me, for bringing the discipline and your incredible expertise to this work. Johann, thank you for taking me as your student and for always finding time to help me, and for the constant motivation throughout this PhD. I know I might not have been the easiest student but I am deeply grateful and honored to have worked with you both. I must also thank Sami K. Solanki for giving me the opportunity to work in this project and for always having a very critical and helpful eye for it. Your suggestions were key in the development of this work.

I also want to thank my university supervisor, Karl-Heinz Glaßmeier. Thank you for agreeing to supervise me and for always being so willing to help me throughout the science and the bureaucracy of this PhD. Thank you as well to Yasuhito Narita for taking part in the committee and for the support for this process in the last months. Thank you to Sonja Schuh for being always patient, for making the IMPRS an enjoyable experience and for always encouraging the collaboration and union between students.

I'd also like to thank Tanja, Johanna, Ines, Fee, Claudia and everyone in the IT center for all the support in all the administrative and technical aspects in the institute. You make our lives much easier and I appreciate it a lot.

Special thanks go to all my friends. I really think that if I made it through this PhD, this distance to home, this years of confusion and uncertainty, a pandemic and 5 german winters it has been because of the friends I have made here. We have shared laughs, joy, tears, fears, travels, spaces and memories. I truly treasure all the friendships I've built here.

Argiris, thank you for all the fun, the food, the trust, the advice and for sharing your family with me when I needed one the most. Kok Leng, thank you for always being there, for being always honest and generous, for always having the best music and for sharing the loneliest of times and the loudest of laughs with me. Thank you to Dušan, Tanay and Jesper as well, we met during the interview week and since then I'm thankful for all the moments we've lived together, always full of laughter, mastiha, friendship and support. Thank you to Neel for all the memes and the open talks about life and feelings, thank you to Philipp for all the trust and sweet food to keep going. Thank you to Isabela for the parties, the coffees and the board games, for sharing Brasil with me. To Sonia for bringing back a bit of Mexico and UNAM with you. To Jonathan, Nikolina, Jonas, Ilse, Paula, Ziwen, Vighnesh, Yara, Sanghita, Abhiroop, Pritwi and Abhas for all the moments shared in these last years. Thank you all for being such a nice group of people and accepting my true weird self.

I must also thank my friends outside the institute, especially Ange and Ramin, and Hector and Oscar, who became my family and safe place in this country, I am

forever thankful for having you in my life. Thank you as well to Mariela, Vane, Ale, Hans, Zepi and all my friends far away. Finally thanks to Kerkeh, for always being there to support me.

The biggest thank you goes to my parents, to whom I dedicate this work. I thank you for the education, life, lessons and love that you've given me all my life. I thank my Mom for always cheering me up and for listening to my graces and disgraces, for all your wisdom and calm. I thank my Dad for being the biggest inspiration and example, and for making it possible (literally) for me to have come here to study. Thank you also to Rosario, for the many valuable advice and reminder that effort and hard work are always worth it. Lastly I want to thank my brothers, Andrés and Víctor, and the rest of my family for all the love and support through the distance and time.

This work has been carried out in the framework of the International Max Planck Research School (IMPRS) for Solar System Science at the Technical University of Braunschweig and has been funded by the Sun and Heliosphere Department Junior Scientist Funding of the Max Planck Institute for Solar System Research of the Max Planck Society.

Publications

Refereed Publications

Romero Avila, A., Inhester, B., Hirzberger, J., & Solanki, S. K. (2024). Photospheric stereoscopy: Direct estimation of solar surface-height variations. *Solar Physics*, *299*(4), 41

Posters and Talks

Poster - Romero Avila, A., Inhester B., Hirzberger J., Solanki S.K. (2024), Stereoscopy with SO/PHI and SDO/HMI: Direct Wilson Depression Estimates. *Joint Solar Orbiter, Parker Solar Probe and DKIST Meeting.*

Poster - Romero Avila, A., Inhester B., Hirzberger J., Solanki S.K. (2022), Solar Surface Sunspots and pores height measurements using stereoscopic observations. *Solar Orbiter Workshop.*

Poster - Romero Avila, A., Inhester B., Hirzberger J., Solanki S.K. (2021), Solar Surface Stereoscopy with SO/PHI: two different methods. *Solar Orbiter School.*

Poster - Romero Avila, A., Inhester B., Hirzberger J., Solanki S.K. (2020), Solar Surface Stereoscopy with Solar Orbiter's Polarimetric Helioseismic Imager (SO/PHI). *AGU Meeting.*

Curriculum Vitae

Name: Amanda Romero Avila
Date of Birth: March 10th, 1993
Nationality: Mexican

Education

Doctoral candidate 2019 - 2024
Technical University of Braunschweig Germany
In the International Max Planck Research School (IMPRS) framework at the Max Planck Institute for Solar System Research.
Thesis Title: *Multi-Spacecraft Solar Surface Stereoscopy: a method for direct estimates of the Wilson depression from combined observations of SO/PHI and SDO/HMI.*

Master Degree in Earth Sciences 2016 - 2019
Universidad Nacional Autónoma de México (UNAM) Mexico
Thesis Title: *Interaction of the solar wind with planetary bodies*

Bachelor Degree in Earth Sciences 2011 - 2016
Universidad Nacional Autónoma de México (UNAM) Mexico
Thesis Title: *Transient events in the Earth's foreshock*

Teaching

Tutoring 2024
Technical University of Braunschweig Germany
May 2024: *The Sun and Heliosphere*

Tutoring 2016 - 2018
School of sciences, UNAM Mexico
Jan-June 2019: *Mathematics for the applied sciences III and IV*
Aug-Dec 2018: *Mathematics for the applied sciences IV* and *Collective phenomena*
Jan-June 2018: *Mathematics for the applied sciences IV*
Jan-June 2017: *Mathematics for the applied sciences IV*
Aug-Dec 2016: *Mathematics for the applied sciences III*
Jan-June 2016: *Mathematics for the applied sciences II*